UNIVERSITÀ
DEGLI STUDI
DI PADOVA

EUV Experimental Physics of Extreme Ultraviolet

RWTH AACHEN UNIVERSITY

Development and Metrology of Extreme Ultraviolet and soft X-ray Multilayer Mirrors

Mewael Giday Sertsu

Doctoral Thesis in Science and Technology of Extreme Ultraviolet and X-rays for Interdisciplinary Applications

Padova, Italy 2016

Università
degli Studi
di Padova

EUV Experimental Physics of Extreme Ultraviolet

RWTH AACHEN UNIVERSITY

Sede Amministrativa: Università degli Studi di Padova

Dipartimento di Ingegneria dell'Informazione

Faculty of Mathematics, Computer Science and Natural Sciences

SCUOLA DI DOTTORATO DI RICERCA IN: Ingegneria dell'Informazione

INDIRIZZO: Scienza e tecnologia dell'Informazione

CICLO: XXVIII

TESI IN COTUTELA

Development and Metrology of Extreme Ultraviolet and soft X-ray Multilayer Mirrors

Direttore della Scuola: Ch.mo Prof. Matteo Bertocco

Coordinatore d'indirizzo: Ch.mo Prof. Carlo Ferrari

Supervisore: Ch.mo Prof. Piergiorgio Nicolosi

Supervisore: Chiar.mo Prof. Dr.rer.nat. Larissa Juschkin

Dottorando: Mewael Giday Sertsu

Table of Contents

Summary

This thesis addresses research works on the development and metrology of multilayer thin-film coatings designed for Extreme Ultraviolet (EUV) and soft X-ray spectral regions. While the development part is limited to reflective multilayers at 6.x nm wavelength, significant part of the thesis is devoted to the metrology of multilayers (MLs) in broader spectral range. The development part focuses on the design and fabrication of MLs of high reflectivity around 6.x nm wavelengths to support below 10 nm half-pitch (HP) patterning of the next generation EUV lithography and tabletop reflectometer for below 10 nm EUV sources. Specific activities under this topic include searching of new candidate materials, numerical design, deposition of the MLs, and performance testing at wavelengths below 10 nm.

The second major topic of the thesis focuses on the comprehensive characterization of MLs using innovative approaches. Most challenging questions in ML coatings such as characterization of buried interfaces, determination of layer and interlayer thicknesses, uncertainties of optical constants near EUV and soft X-ray absorption edges are pressing issues. Synchrotron based Grazing-Incidence EUV Reflectivity (GI-EUVR) near absorption edges of one of the component elements in the ML structure is proposed as a major technique to achieve the metrology demands. The strength of GI-EUVR analysis of MLs lies on its simultaneous sensitivity to optical and structural parameters. The proposed EUV metrology method is also capable of evaluating damage analysis of high intensity photons and/or energetic particles on ML performances. In combination with traditional ML characterization techniques, the GI-EUVR enabled characterization of the most challenging buried–interface diffusion processes during multilayer growth. Analysis of chemical composition and corresponding optical properties of inter-diffusion layers are performed near Si L_{III} - edge for Mo/Si and near elemental boron (B) edge for B4C/CeO2 MLs to demonstrate the robustness of the proposed method. Changes of structural and optical parameters of MLs for applications in astronomical telescopes due to the bombardment of helium particles (4 keV He^{++}) that are dominant in the solar corona can be analyzed using the current techniques.

Lastly, the thesis deals with the development of tabletop scatterometer experiment around 13.5 nm EUV wavelength based on Xenon gas discharge produced plasma source. EUV scattering measurements at 13.5 nm central wavelength and 2% bandwidth can be simple and fast surface roughness analysis in the mid-spatial frequency range. Surface patterns in the mid-spatial frequency ranges are resolved in the scattered signals from multilayer surfaces.

Sommario

Questa ricerca spiega tesi lavora allo sviluppo e metrologia di rivestimenti a film sottile multistrato progettate per Estremo Ultravioletto (EUV) e regioni spettrali raggi X molli. Mentre la parte di sviluppo è limitato a multistrati riflettenti a 6.x nm, parte significativa della tesi è dedicata alla metrologia multistrati (ML) in campo spettrale più ampia. La parte di sviluppo si concentra sulla progettazione e fabbricazione di ML di alta riflettività intorno 6.x nm lunghezze d'onda per sostenere sotto 10 nm half-pitch (HP) paterni della litografia EUV prossima generazione e da tavolo per riflessione inferiori a 10 nm fonti EUV. Attività specifiche per questo argomento includono la ricerca di nuovi materiali candidati, progettazione numerica, la deposizione delle ML, e test delle prestazioni a lunghezze d'onda inferiori a 10 nm.

Il secondo grande tema della tesi si concentra sulla caratterizzazione completa di ML utilizzando approcci innovativi. La maggior parte delle domande impegnative nei rivestimenti ML quali la caratterizzazione di interfacce sepolte, la determinazione del livello e interstrato spessori, incertezze costanti ottiche vicino EUV e bordi di assorbimento di raggi X molli premono problemi. Sincrotrone basato Grazing Incidente - EUV riflettività (GI-EUVR) in prossimità di bordi di assorbimento di uno degli elementi componenti della struttura ML viene proposto come una tecnica importante per ottenere le richieste di metrologia. La forza di analisi GI-EUVR di ML si trova sulla sua sensibilità simultanea di parametri ottici e strutturali. Il metodo proposto EUV metrologia è anche in grado di valutare l'analisi dei danni di fotoni ad alta intensità e / o particelle energetiche sulle prestazioni ML. In combinazione con le tradizionali tecniche di caratterizzazione ML, la caratterizzazione GI-EUVR permesso dei processi di diffusione di interfaccia sepolto più impegnative durante la crescita multistrato. Analisi della composizione chimica e corrispondenti proprietà ottiche degli strati tra di diffusione vengono effettuate nei pressi Si L_{III} - bordo per Mo / Si e vicino elementare di boro (B) bordo per B4C / CeO2 ML per dimostrare la robustezza del metodo proposto. Modifiche di parametri strutturali ed ottiche di ML per applicazioni in telescopi astronomici a causa del bombardamento di particelle di elio (4 keV He $^{++}$) che sono dominanti nella corona solare possono essere analizzati usando le tecniche attuali.

Infine, la tesi si occupa dello sviluppo di esperimento da tavolo dispersione intorno 13,5 nm di lunghezza d'onda EUV in base a scarica di gas Xenon sorgente del plasma prodotto. EUV misurazioni di dispersione a 13,5 nm lunghezza d'onda centrale e 2% della larghezza di banda può essere semplice e veloce analisi rugosità superficiale nella gamma di frequenze medio-spaziali.

Acknowledgment

Firstly, I would like to express my sincere gratitude to my advisors Prof. Piergiorgio Nicolosi and Prof. Larissa Juschkin for the continuous support of my PhD study and related research, for their patience, motivation, and immense knowledge. Their guidance helped me in all the time of research and writing of this thesis. I could not have imagined having better advisors and mentors for my PhD study. Besides my advisors, I would like to thank Prof. John Costello, Prof. Gerry O'Sullivan and all the other members of the EXTATIC program for organizing and accepting me as a student.

My sincere thanks to the academic and administrative staff in CNR-IFN Padova for your commitment in supporting me even on non-academic issues, which was not easy at all as a foreign student. Special thanks goes to Dr. Alain Corso, Dr. Paola Zuppella, Dr. Maria Pelizzo, Marco Nardello (PhD researcher) and Antonella Comisso (PhD student) for your humble support in the academic matters. Many thanks to everyone in the "officio dottorandi" for the friendship we all had. Not to mention the coffee break lectures☺. Off course genuine gratitude to the administrative staff of department of information engineering (DEI) especially to Cristina Capuzzo, Stefania schiavon, Sabrina Michel, Enrico Soncin and to the secretary of the PhD school Ms. Alessandra Calore.

I am also grateful for the colleagues and staff at the Fraunhofer ILT for giving me the chance to work in the beautiful labs and made me learn a lot during my mobility to RWTH Aachen University. Special thanks to Aleksey Maryasov for being my lab instructor and my guide in many other issues. I thank my fellow students in the EXTATIC program for having insightful discussions during the welcome weeks and conferences. The work in this thesis is also a collaborative effort of people from many universities. I would like to thank Prof. Zhanshan Wang from Tongji University and Dr. Angelo Giglia from ELETTRA Synchrotron.

I am so much grateful to my wife who has been with me all along the three years. Thanks for your patience and understanding.

Finally, I need to say thank you to the EU for funding both my master and PhD studies through the Erasmus Mundus program. Thanks to the short-term scientific mission (STSM) of the COST action for supporting my scientific activities.

List of publications and conferences

I. **Publications included in this thesis**

I. **M.G. Sertsu**, Paola Zuppella, M. G. Pelizzo, P. Nicolosi “Exploring EUV near absorption edge optical constants for enhanced and sensitive grazing incidence reflectivity*”, Proc. SPIE 8861, Optics for EUV, X-Ray, and Gamma-Ray Astronomy VI, 886111 (26 September 2013)*

II. **M. G. Sertsu,** A. Giglia, S. Brose, A. Comisso, Z. S. Wang, L. Juschkin and P. Nicolosi " Optical and structural characterization of CeO2/B4C multilayers near the Boron absorption edge *", Proc. SPIE 9510, EUV and X-ray Optics: Synergy between Laboratory and Space IV, 95100T (May 12, 2015*

III. **M. G. Sertsu,** A. Giglia, L. Juschkin and P. Nicolosi " Irradiation of low energy ions damage analysis on multilayers ", *Proc. SPIE 9511, Damage to VUV, EUV, and X-ray Optics V, 95110P (May 12, 2015)*

IV. **M. G. Sertsu**, M. Nardello, A. Giglia, A. J. Corso, C. Maurizio, L. Juschkin, and P. Nicolosi "Analysis of buried interfaces in multilayer mirrors using grazing incidence extreme ultraviolet reflectometry near resonance edges," *Appl. Opt.54, 10351-10358 (2015)*

V. **M.G. Sertsu**, A.Giglia, S.Brose, D. Park, Z. S. Wang, J. Mayer, L. Juschkin, P. Nicolosi, “Deposition and characterization of B4C/CeO2 multilayers at 6.x nm extreme ultraviolet wavelengths”, *Accepted with minor corrections in Journal of Applied physics (JAP)*

II. Other publications:

A. M. Nardello, V. Polito, P. Zuppella, Alain J. Corso, S. Zuccon, **M.G. Sertsu**; P. Nicolosi, S. Fineschi, G. Naletto, E.Antonucci, Maria G. Pelizzo “Solar alpha particles damage effects on UV and EUV optical coatings”, *Proc. SPIE 8862, Solar Physics and Space Weather Instrumentation V, 886207 (26 September 2013)*

B. A. Comisso, A. Giglia, M. Nardello, E. Tessarolo, L. Calvillo, **M. G. Sertsu, G.** Granozzi, F. Gerlin, L. Brigo and P. Nicolosi " Characterization of TiO2 thin films in the EUV and soft X-ray region ", Proc. SPIE 9510, EUV and X-ray Optics: Synergy between Laboratory and Space IV, 95100Z (May 12, 2015)

II. Presentations at Conferences and summer schools

i. **M. G. Sertsu**, L. Juschkin, N. Piergiorgio "EXTATIC summer school", Sept 15 -21, 2012, DCU (Ireland)

ii. **M. G. Sertsu**, L. Juschkin, N. Piergiorgio, "Grazing incidence small angle X-ray scattering", Oct 07 -09 /2013, DESY (Hamburg) – ***Poster presentation***

iii. **M.G. Sertsu**, Paola Zuppella, M. G. Pelizzo, P. Nicolosi, "Exploring EUV near absorption edge optical constants for enhanced and sensitive grazing incidence reflectivity", SPIE Optics + Photonics 2013, August 25-29,2013, San Diego, USA – ***Oral presentation***

iv. **M.G. Sertsu**, Paola Zuppella, M. G. Pelizzo, L. Juschkin, P. Nicolosi , "EUV multilayer coatings and modeling of interface diffusion" EXTATIC summer school, Oct 01 -04, 2013, Aachen, Germany - ***POSTER***

v. **M. G. Sertsu**, M. Nardello, A. Giglia, A. J. Corso, C. Maurizio, L. Juschkin, and P. Nicolosi, "Synchrotron based EUV reflectivity measurement near absorption edges for multilayer analysis" Cost Action MP2013 general assembly on advanced X-ray spatial and temporal metrology ", Oct 29 -03 /2014, Dubrovink – ***Oral presentation***

vi. **M. G. Sertsu**, M. Nardello, A. Giglia, A. J. Corso, C. Maurizio, L. Juschkin, and P. Nicolosi, "Analysis of buried interfaces in multilayer mirrors using grazing incidence extreme ultraviolet reflectometry near resonance edges" Extreme ultraviolet lithography (EUVL) international symposium", Oct 27 -29/ 2014, Washington DC – ***Poster presentation***

vii. **M.G. Sertsu**, A.Giglia, S.Brose, D. Park, Z. S. Wang, J. Mayer, L. Juschkin, P. Nicolosi, "Optical and structural characterization of CeO_2/B_4C multilayers near the Boron absorption edge ", SPIE Optics + Photonics 2015, April 13-16, 2015, Prague – ***Oral presentation***

viii. **M. G. Sertsu,** A. Giglia, L. Juschkin and P. Nicolosi, " Irradiation of low energy ions damage analysis on multilayers ",SPIE Optics + Photonics 2015, April 13-16, 2015, Prague – ***Poster presentation***

ix. **M. G. Sertsu,** A. Giglia, L. Juschkin and P. Nicolosi , “ Near edge EUV reflectivity techniques for multilayer damage analysis”, 5th METIS (Multi-element Telescope for Imaging and Spectroscopy) Science Meeting, Sept 5, 2015, Florence (Italy) – ***oral presentation***

x. Aleksey Maryasov, Jenny Tempeler, **Mewael Sertsu**, Larissa Juschkin, “ EUV scattering metrology with high-brightness discharge plasma source”, 5-6 November 2015,VUV and EUV Metrology seminars, PTB, Berlin, Germany – ***Oral presentation***

Acronyms

UV	Ultraviolet
EUV	Extreme Ultraviolet
XRR	X-ray reflection
ML	Multilayer
CL	Capping layer
EUVL	EUV lithography
GI-EUVR	Grazing incidence EUV reflection
BEAR	Bending magnet for Emission, Absorption and Reflectivity
FELs	Free electron lasers
NA	Numerical aperture
DOF	Depth of focus
RF	Radio frequency
DC	Direct current
E-beam	Electron beam
ALD	Atomic layer deposition
PVD	Physical Vapor Deposition
AU	Astronomical unit
BRDF	Bidirectional reflection distribution function
ARS	Angle resolved scattering
PSD	Power spectral density
GI-EUVS	Grazing incidence EUV scattering

WLI	White light interferometer
AFM	Atomic force microscopy
STEM	Scanning transmission electron microscopy
SEM	Scanning electron microscopy
HAADF	High angle annular dark-field
BF	Bright field
DWBA	Distorted wave Born approximation
BA	Born approximation
DW	Debye - Waller
NC	Novet' – Croce
keV	Kilo electron volt
FWHM	Full width half maximum
GA	Genetic algorithm
DE	Differential evolution
METIS	Multi-element telescope for imaging and spectroscopy
TRIM	Transport of ions in medium

1. INTRODUCTION

1.1 Motivation

The last four decades have seen significant progress on the science and technology of multilayer mirrors. DuMond and Youtz made the first attempt in making multilayers (MLs) of Cu-Al in 1940 [1]. Efforts continued to make stable MLs and after three decades in 1972, Spiller et.al fabricated MLs of stable reflection performance [2]. The following two decades after Spiller's success sought several national laboratories such as Bell and Sandia national laboratories in the US and NTT in Japan progressively exploring the science and technology of ML mirrors. Those early attempts of ML coatings were inspired by the need of mirrors in extreme ultraviolet (EUV) and X-ray solar imaging, X-ray microscopy, EUV lithography and various applications in X-ray lasers.

In solar missions, there has been strong desire to study physical processes that occur because of energetic X-ray irradiation and thermal emissions at high temperatures (10^7 k°) of the solar plasmas. This has pushed the X-ray astronomy to include graded multilayer mirrors to the X-ray telescopes and gain focusing capability for incidence photon radiation around 10 keV above the critical angle [3]. At much lower energies in ultraviolet (UV) and EUV, solar missions succeeded in identifying elemental compositions of solar corona and elemental traces of heavy ions. So far, discoveries in the solar missions have inspired to set ambitious future missions. Future solar missions such as the Solar Orbiter (SO) mission of the European space agency (ESA) are determined to study the sun's heliosphere at an unprecedented distance ($<$ 0.28 A.U at perihelion minimum from the sun center) [4]. The SO mission is expected to answer open questions related to the sources of energetic particles in the solar corona, origins of fast and slow solar winds, eruption and early evolution of coronal mass ejections and much more. One important task for the sun-observing satellites that needs to be studied thoroughly before takeoff is stability of optics (particularly of ML mirrors) that make up the coronagraph payload. The stability test of ML mirrors to high thermal loads, energetic particles (such as the H-I Lyman - α line and He –II Lyman), continuous photon irradiation and environmental aging are still under research and are crucial. A considerable part of the thesis is then dedicated to the development of innovative metrology techniques for the damage analysis of ML mirrors exposed to low energetic ions/particles that are dominant in the solar corona [5].

Multilayers are also essential components of the next generation integrated circuit (IC) printing technology based on EUV lithography at 13.5 nm wavelength. Most naturally found materials absorb significant power of the incident materials become in this range of wavelengths, MLs provide sufficient throughput power through reflection.

Thus far, coatings of Mo/Si MLs are qualified as essential components of the collector module and projection optics module in the EUV lithography (EUVL) scanners [6-9]. The MLs reflect significant amount of the incident light and then provide sufficient throughput to resolve smaller features on the wafer.

The smallest diffraction limited feature size resolved on the wafer's photoresist in EUV photolithography projection scanners is given by Rayleigh criterion of image resolution:

$$\text{Smallest feature size} = k_1 \frac{\lambda}{NA} \tag{1-1}$$

$$\text{DOF} = k_1 \frac{\lambda}{NA^2} \tag{1-2}$$

Where k_1 depends on the process and photoresist properties, numerical aperture (NA) is the geometrical opening of the optical system, λ is the illumination wavelength, DOF is the depth of focus.

As the NA and k_1 are reaching physical limits, the way forward is tuning the source radiation towards shorter wavelengths to sustain the Moore's law in the semiconductor industry. This has currently reached at 13.5 nm Laser Produced Plasma (LPP) source for half-pitch (HP) pattern printing below 20 nm on the Si wafer. No surprise, there is strong desire to extend this 13.5 nm EUVL architecture towards 6.x nm EUVL to enable below 10 nm HP IC printing [10]. The toughest challenge in this extendibility road map of the industry is availability of efficient and stable multilayer mirrors that can reflect above 70 % of the incident radiation at that short wavelength. Searching new material combinations (candidates) and characterizing their ultimate potentiality in terms of reflection performance around 6.x nm wavelength is the second motivation of the thesis in an attempt to partly answer the semiconductor industry demand of future lithography technologies based on EUV sources radiating below 10 nm wavelengths.

Large part of this PhD work, however, focuses on the metrology of EUV and soft X-ray multilayers. This is intended to answer some of the apparent challenges in multilayer characterizations. For EUV and soft X-ray multilayers, optical constants, buried interfaces and corresponding chemical and optical parameterization, correlation of thickness and optical properties, deviation of measured optical constants of materials near EUV resonance edges from previously tabulated values by Henke and his colleagues are some of the questions that need to be investigated further. This thesis then focuses on innovative characterization methods for EUV and soft X-ray multilayers to contribute a comprehensive and sensitive analysis of multilayers. Besides, the possibility of using gas-discharge produced based plasma (DPP) EUV sources for a tabletop thin film and nanostructures scatter analysis is assessed in an attempt to leverage limited and expensive Synchrotron and free electron sources.

This chapter introduces EUV and soft X-ray radiations and basic theoretical background of multilayers. Chapter 2 introduces Electron-beam evaporation and magnetron sputtering deposition techniques that are two commonly used fabrication techniques of thin films and multilayers. A list of multilayer and thin film characterization techniques are also provided in this chapter. Chapter 3 introduces grazing incidence EUV reflectivity measurements near absorption edges of elements as innovative metrology technique of EUV and soft X-ray multilayers. Chapter 4 reports on fabrication and reflectivity performances of new multilayer candidates for the 6.x nm EUV lithography. Chapter 5 describes tabletop EUV scattering experiments for surface roughness derivation. Finally, Chapter 6 contains summary and conclusion of the thesis work.

1.2 Extreme ultraviolet and soft X-rays

Even if it is difficult to put clear cut boundaries in the electromagnetic (EM) spectrum, it seems there is a consensus that the Extreme Ultraviolet (EUV) wavelengths lie somewhere from 5 - 40 nm and soft X-rays cover from 0.1 - 5 nm as shown in Fig 1.1. The EUV radiation and soft X-rays are relatively the last spectra to be studied and sought for applications from the EM spectrum. The physics and applications of EUV radiation and soft X-rays are thoroughly described in the book of D. Attwood [11] and only brief introduction is given this section.

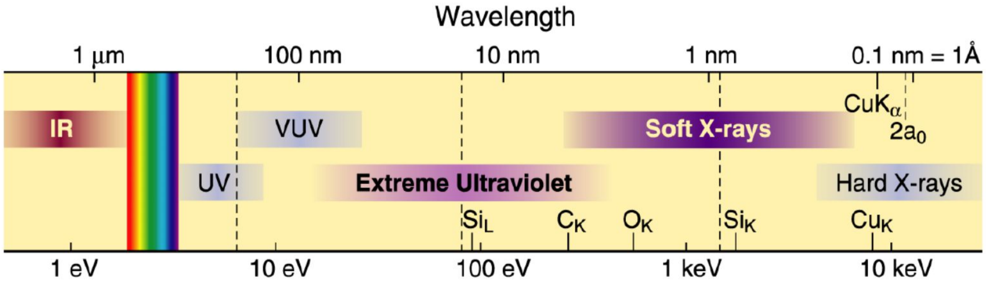

Figure 1. 1: A section of the electromagnetic spectrum indicating the positions of Extreme-ultraviolet (EUV) and soft X-rays [6].

EUV radiation (also soft X-rays) show characteristic interaction with matter that has found applications in life and material sciences. It also requires characteristic technology to develop radiation sources. The distinct feature of EUV and soft X-rays is associated to the high absorption almost by all materials exacerbated due to the natural occurrences of absorption edges of elements in this spectrum. The high absorption of short wavelength spectra in a material medium forced both source generation and performing measurements demand ultra-high vacuum (UHV) environment. Also because of the high absorption coefficients that limit penetration depths to few microns for most relevant materials, the traditional transmission optics is not any more efficient for several EUV and soft X-ray applications. Attenuation lengths of few very important elements are given in Fig 1.2 for EUV and soft X-ray wavelengths from the tabulated values originally measured by Henke and his co-authors [12], and available at the Center for X-ray Optics (CXRO) database <http://henke.lbl.gov/optical_constants/>. For most of the elements, the attenuation lengths are below 100 nm.

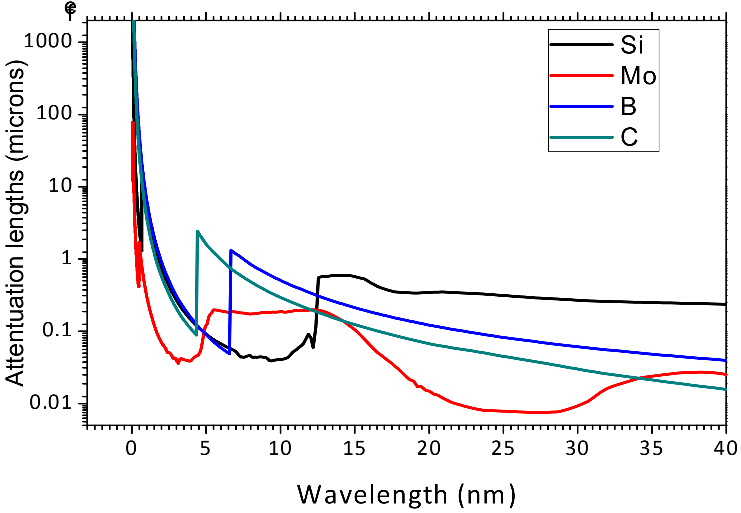

Figure 1. 2: EUV and soft X-ray attenuation lengths of Si, B, C and Mo elements

This situation has motivated the academia and industry to think reflection based optics to enhance the throughput through interference coatings. Stacks of artificial layers (multilayers) of few nanometer thicknesses started to appear as vital devices for normal and grazing incidence reflections. The optical parameters, working principles and performances of the multilayers are explained in this chapter. Optical properties of materials in EUV and soft X-rays are explained first since optical behavior and contrasts play a major role in determining performances of the multilayers.

1.2.1 Optical constants of materials in EUV and soft X-rays

Several authors have determined optical constants of materials in EUV and soft X-rays based on simple thin film transmission, reflection and absorption measurements at Synchrotron or in-house discharge lamp sources. Windt et al. determined the optical constants of electron-beam evaporated films of Ti, Zr, Nb, Mo, Ru, Rh, Pd, Ag, Hf, Ta, W, Re, Os, Ir, Pt, and Au in EUV wavelengths by using angle dependent reflectance measurements [13]. Similarly, Soufli and Gullikson determined optical constants of Si in the energy range of 50 – 180 eV using angle dependent reflectance measurements at synchrotron radiation source [14] . Fernández-Perea et al. calculated the optical constants of B films in the spectral range 6.8 to 900 eV by using transmittance measurements [15]. However, a comprehensive derivation of complex scattering factors f_2 of elements starting from atomic number Z=1 - 92 for the photon energies in EUV and

X-rays (E=50 - 30,000 eV) were tabulated by Henke and his coworkers [12]. Henke et.al compiled the data from previously measured absorption spectra by using interpolations and suitable theoretical models. The corresponding real part of the scatterings, i.e. f_1 was derived numerically by using the dispersion integrals (Kramers-Kroning).

The transmission, reflection and absorption measurement techniques are evolving continuously strengthened by innovations of numerical optimization methods andimproving measurement accuracies. As a result, the derived optical and/or scattering constants are used widely in designing thin films and MLs for many fundamental and technological applications. At the same time, the limitation of the methods have been identified when it comes to EUV and soft X-rays. Several measurements from the synchrotron facilities have reported variations from the calculated optical constants in EUV and soft X-ray wavelengths; these are due to smoothing out of fine structures in the absorption curves[16] and and also due to the high sensitivity of optical constants near absorption edges of EUV and soft X-rays to local atomic interactions [17, 18]. A typical example is given in Fig 1.3, where optical constants (δ and β) of boron carbide (B4C) calculated using Henke et al. show $\sim 38\,\%$ deviation (including numerical fit errors) from measured values at energies near the absorption edge of Boron[17]. Optical constants at photon energies far from the edge show similarity to Henke's calculations. This demonstrates the necessity of measurements of EUV and soft X-ray optical parameters of materials in their actual environments using techniques with appropriate optical sensitivity.

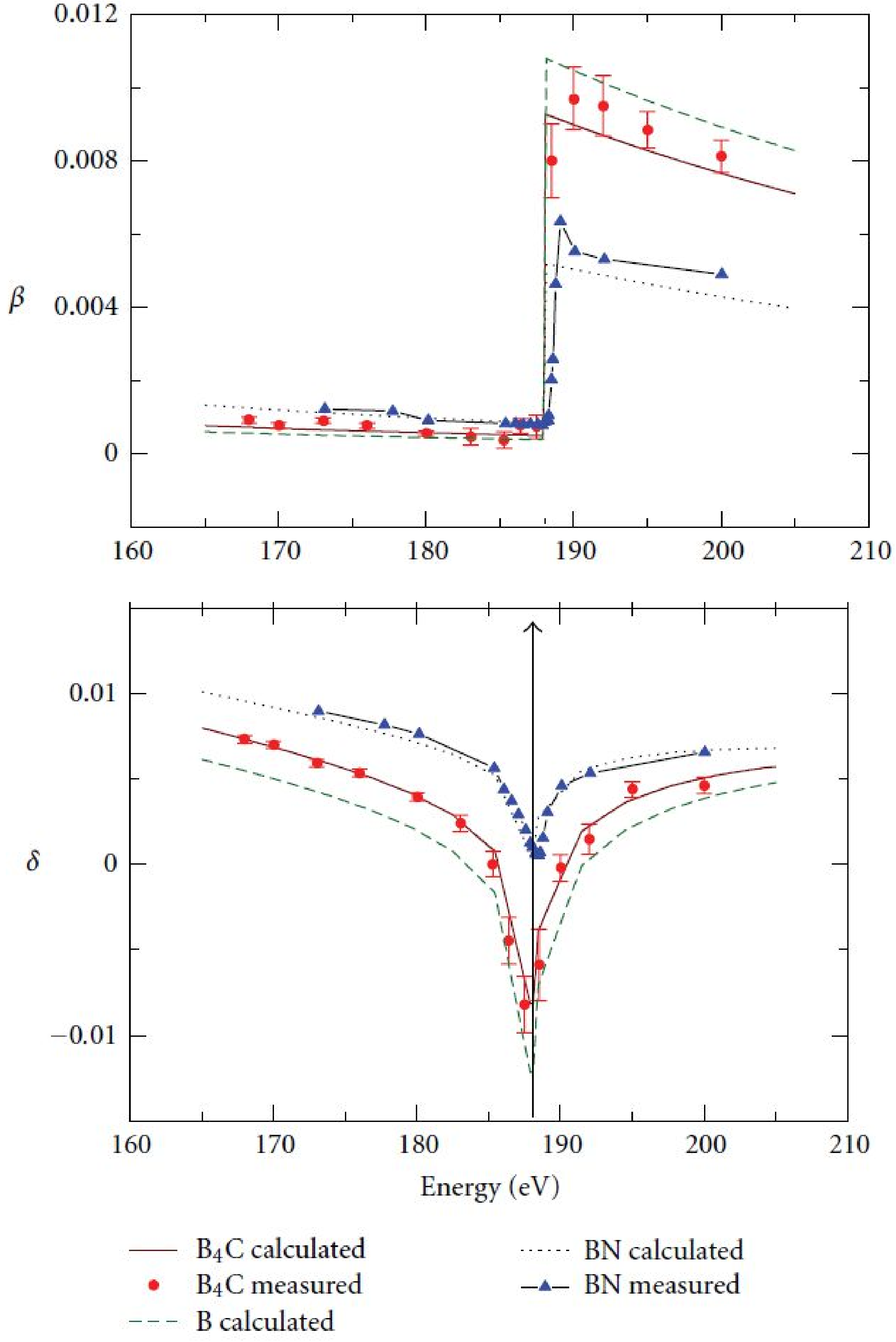

Figure 1. 3: The energy dependent optical constants for B4C, B, and BN as function of photon energies near the boron K-absorption edge (source: page 9 of ref [17]).

A theoretical approach that accounts light-matter interactions at microscopic level is necessary to explain the macroscopic optical phenomena that also accounts for effects of the fine structures. This can be done through the concept of scattering cross sections of particles. Radiation scattering can take place from free electrons, bound electrons, ions and atomic nuclei. In real EM wave-matter interaction, all of those interactions take place. There exist rigorous quantum mechanical calculations that provide accurate way of treating EM scatterings and scattering cross sections. However, much can be learned from the simplified semi-classical atomic scattering model, and basic results are similar in form to those derived by quantum mechanical models [11]. In the semi-classical model, under the forward scattering approximation, the equation of total EUV and soft X-ray photon-scattering cross section (σ) by multi-electron atoms has the following form:

$$\sigma(\omega) = \frac{8\pi}{3}\, r_e^2\, |f^o(\omega)|^2 = \left[\frac{8\pi}{3}\, r_e^2\right] \times \left[\sum_{s=1}^{N} \frac{-g_s\omega^2}{\omega^2-\omega_s^2+i\gamma\omega}\right]^2 \tag{1-3}$$

Where γ is the damping factor due to the absorption, ω_s is the resonance frequency of the atomic transition and ω is the frequency of incident radiation, g_s is the quantum mechanical parameter related to the oscillatory strength of electronic transitions. The physical interpretation of total scattering cross section (σ) in eq. (1-3) refers to the effective number of free electrons contributing to the scattering. The $f^o(\omega)$ is wavelength dependent complex scattering factor, which can be parametrized into real and complex components as given in EUV and soft X-rays by Eq. (1-4).

$$f^o(\omega) = f_1^o(\omega) + i f_2^o(\omega) \tag{1-4}$$

Where f_1^o and f_2^o are scattering factors of an element associated with scattering (reflection) and absorption respectively. The complex refractive indices in EUV and X-rays can be described by the dispersion relation (Eq. 1-5) in terms of scattering factors f_1^o and f_2^o. In this range of energies, interactions with valence electrons are negligible that core level electrons dominate optical responses. This approximation, however, does not hold for longer wavelengths since interactions with valence electrons become significant.

$$n = 1 - \delta - i\beta = 1 - \frac{n_a r_e \lambda^2}{2\pi}\,(f_1^o + i f_2^o) \tag{1-5}$$

Where n_a is the atomic density per unit volume, r_e is the classical electron radius ($\sim 2.82 \times 10^{-15}\ m$), λ is wavelength of radiation. The scattering factors f_1^o and f_2^o are parametrized from the equation of scattering cross-section σ of a semi-classical scattering model for EUV and soft X-Rays in a forward scattering approximation.

The oscillator strength g_s in Eq.(1-3) represents the number of electrons associated with a given resonance frequency ω_s where for high photon energy $\int_{s=1}^{N} g_s = Z$ (atomic number) [11]. When incident radiation frequencies are tuned to approach natural frequencies corresponding to the core electrons binding energies, scattering factors (and thus optical constants) change abruptly because of resonance absorption by the strongly bound electrons. In EUV and soft X-rays, near-edge absorption and reflection measurements can resolve fine structure details that enable to identify chemical compositions. This makes the near absorption edges sensitive to the configuration (i.e. chemical and physical interactions) of an atom in its local environments.

1.3 Basic principles of multilayer mirrors

Multilayers are optical coatings of alternating layers of high and low density materials on polished mirror substrates. The layers are analogous to Bragg lattice planes in natural crystal structures that are common in X-ray crystallography. Typical periodic multilayer structure is shown in Fig 1.4 with D representing bi-layer thickness (i.e. period), Γ denotes ratio of high-density layer (absorber layer) to the period D, and N represents number of bi-layers above the substrate.

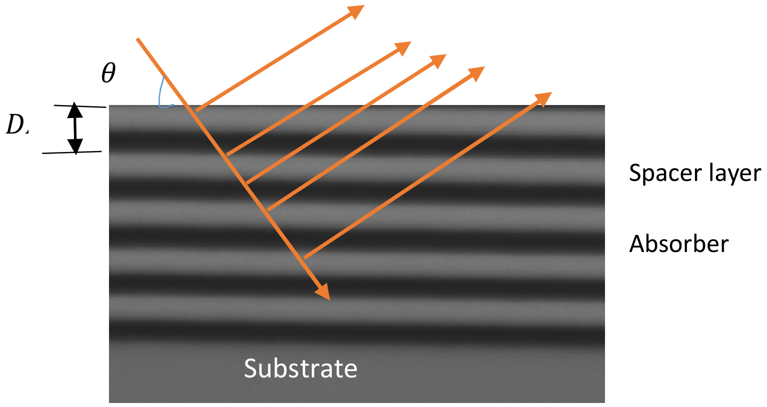

Figure 1. 4:B4C/CeO2 periodic multilayer

Constructive Interference from each interfaces within in the ML stack gives rise to the enhancement of reflectivity becoming intense enough for imaging in EUV and X-ray wavelengths at near-normal incidence angles. Similar to natural crystals, interference behavior in MLs is described by the Bragg equation, slightly modified to account the refraction of EUV and soft X-ray radiation that take place at the interfaces of ML mirrors.

$$m\lambda = 2D\sin\theta\ (1-\frac{2\bar{\delta}}{sin^2\theta})^{1/2} \tag{1-6}$$

Where $\bar{\delta}$ is weighted real part of the refractive index of a bilayer, and θ is grazing-incidence angle. Performance of a multilayer mainly depends on optical contrasts between low Z and high Z materials and sharpness/levelness of interface profiles.. Moreover, optimizing illumination angles and wavelengths, layers thickness ratios and number of bilayers (N) is crucial for ML design and enhancing its reflectivity and tailoring the bandwidth ($\Delta\lambda$) of the reflected beam. Reflectivity enhancement is not only in obtaining high optical contrast but also in reducing the absorption. Ideally, the low Z layers act as “spacers” with low optical constants ($\delta\ and\ \beta$) to maximize optical contrast while high Z layers act as “absorbers” and perform both absorption and scattering. The thickness of absorber layers has to be as low as possible to minimize the absorption while keeping strong scattering (reflection) at the interfaces. The design challenge of MLs is then to find high refractive indices contrast (i.e. high $\Delta\delta$) and the optimum thickness ratio (Γ_{opt}).

For normal incidences, Vinogradov and Zeldovich [11] found that an optimal thickness ratio (Γ_{opt}) for a two-material multilayer mirror need to satisfy Eq.(1-7).

$$tan(\pi\Gamma_{opt}) = \pi(\Gamma_{opt} + \frac{\beta_s}{\beta_a+\beta_s}) \tag{1-7}$$

Where subscript “a” and “s” refers to absorber and spacer layers respectively. However, due to the imperfections of deposition process, the practical Γ_{opt} value is often greater/smaller than the theoretical design.

For ideally smooth interfaces of a multilayer mirror with a substrate of finite thickness, reflection (r) and transmission (t) coefficients of plane incidence waves at each interfaces are calculated according to Fresnel equations for s and p polarized radiation. Based on the ML structure given in Fig 1.5, amplitude reflectivity and transmission at the jth interface calculated by Equations (1-8 -1-11).

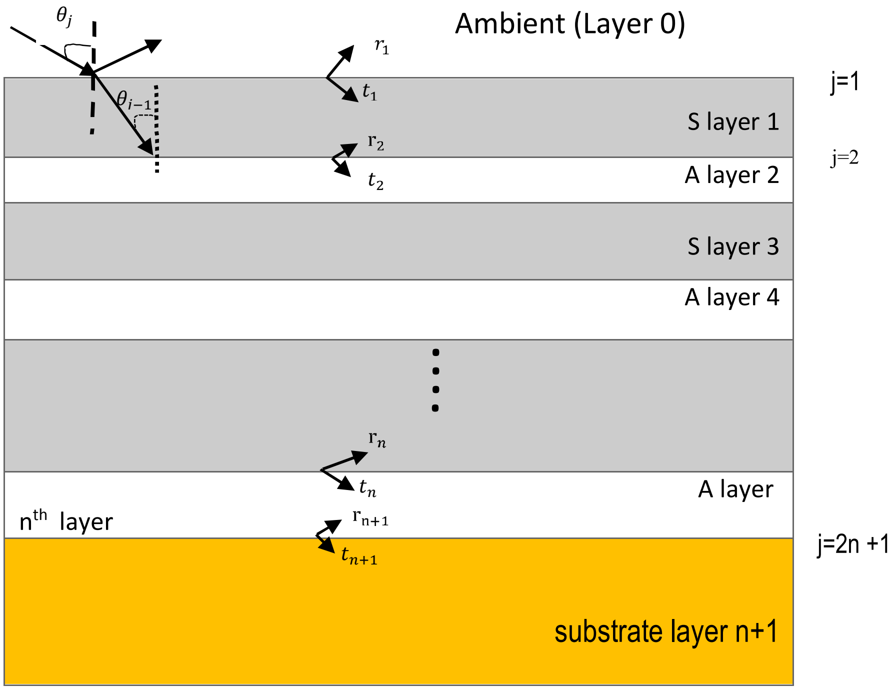

Figure 1. 5: Amplitude reflection and transmission of incident plane wave approximation at the interfaces of a ML structure. S layer refers to “spacer” and A layer is “absorber” layer, reproduced from the thesis of Hui Jiang [14].

$$r_{s,j} = \frac{n_{j-1}\cos\theta_{j-1} - n_j\cos\theta_j}{n_{j-1}\cos\theta_{j-1} + n_j\cos\theta_j} \tag{1-8}$$

$$r_{p,j} = \frac{n_{j-1}\cos\theta_j - n_j\cos\theta_{j-1}}{n_{j-1}\cos\theta_j + n_j\cos\theta_{j-1}} \tag{1-9}$$

$$t_{p,j} = \frac{2n_{j-1}\cos\theta_{j-1}}{n_{j-1}\cos\theta_j + n_j\cos\theta_{j-1}} \tag{1-10}$$

$$t_{s,j} = \frac{2n_{j-1}\cos\theta_{j-1}}{n_{j-1}\cos\theta_{j-1} + n_j\cos\theta_j} \tag{1-11}$$

Apart from the fundamental similarity in working principles, slight changes in design, optimization, fabrication and characterizations of MLs for applications in different areas is understandable. For this reason, short description of MLs for applications in EUV lithography and astronomy are provided here in order to appreciate the related peculiarities in design and metrology.

1.3.1 Multilayers for EUV lithography

One of the driving forces for the advent of short period MLs into the microfabrication technology came from the desire of the semiconductor industry to miniaturize the silicon technology to sustain the “Moore’s” law formulated by Gordon Moore in 1965 [19], which demands doubling of number of transistors on a Si wafer almost in every two years. More transistors means increased functionality, and smaller transistors means increased switching speed and less power consumption for each transistor. The density of transistors in the integrated circuit (IC) is largely determined by the ability of the photolithography process to print an increasingly narrower and sharper feature sizes.

In fact, the history of photolithography (Fig 1.6) is a continuous effort to improve the resolution of lithography systems (commonly known as scanners) by optimizing the processes and photoresist properties, increasing NA of optical systems and shifting to shorter wavelengths. This way, cutting-edge lithography has shifted from the 365 nm 'i-line' of mercury vapour lamps to deep-ultraviolet light from excimer lasers at 248 nm (krypton fluoride lasers) and 193 nm (argon fluoride lasers), and since the year 2010 to the 13.5 nm EUV (tin based LPP sources) [20, 21].

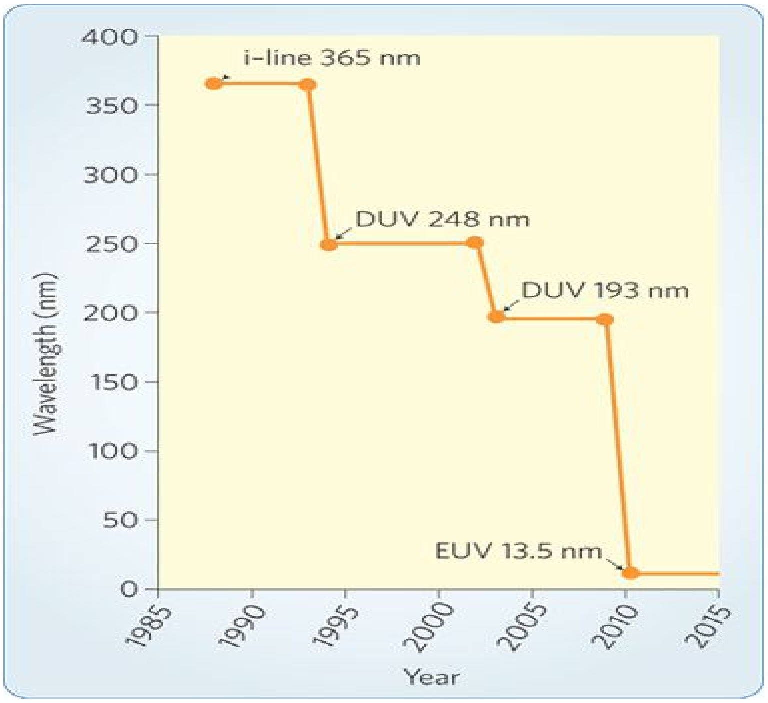

Figure 1. 6: Since the mid-1980s, the wavelength of light used in lithography systems has reduced by almost half from 365 nm to 193 nm.

The EUV lithography at 13.5 nm is the first category from the next generation (NG) scanners with a potential to print below 22 nm features on the IC wafer. Basic design structure and elements of the 13.5 nm EUV lithography system is given in Fig 1.7 from ref [22].

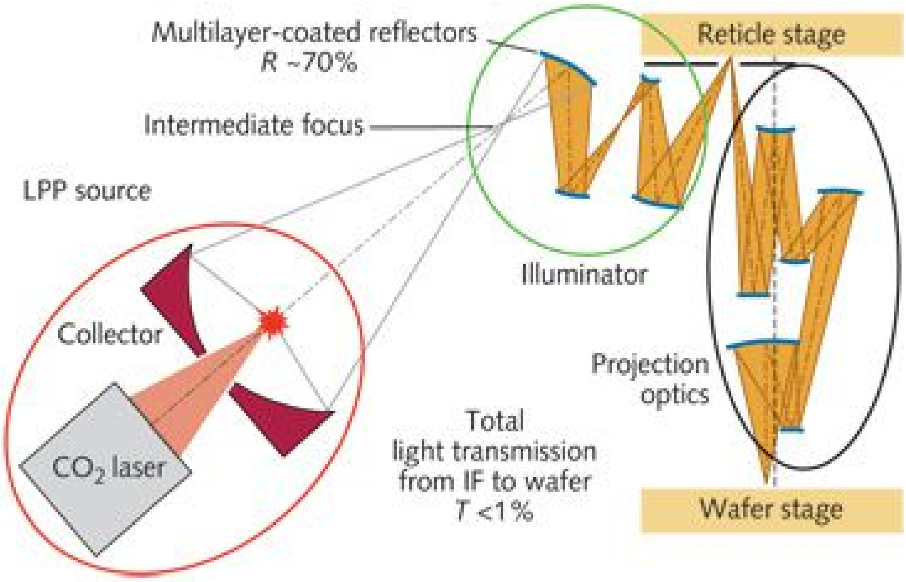

Figure 1. 7: Basic elements of EUV lithography system based on 13.5 nm LPP source

In the version shown in Fig 1.7, pulses from a CO_2 laser illuminate droplets of tin, shown as a red spot, which radiate 13.5 nm light in all directions. A collector mirror focuses the light into a reflective optical system that directs the light onto a reticle, which a second set of mirrors, at right, focus onto the wafer stage. Overall transmission from the intermediate focus at top center to the wafer stage is less than 1%. *(Courtesy of Cymer)* [22]. The basic EUVL system contains ML mirrors (Mo/Si on Si substrate) as the main and critical components of both the illumination and projection optics modules. These MLs need to reflect at least 70 % of the incident radiation to produce sufficient intensity throughput at the wafer stage for resolvable feature printings. The MLs in the projection optics are also responsible for de-magnify images of photoresist mask by 4 × . Moreover, the MLs need to be stable over extended period of photon fluxes. In over all, it is clear that the Mo/Si MLs are the enabling optical devices for the next generation EUV lithography.

Mo/Si based MLs are among the well studied and exploited for UV, deep UV and EUV regime. However, for EUV wavelengths below 10 nm, the performance decays and other ML combinations based on Lanthanum (La) and Boron (B) have gained considerable attention.

There are two compelling reasons for the shifting towards sub 10 nm MLs. One is the desire in the semiconductor industry to extend the 13.5 nm EUVL to 6.x nm to enable photographic printing of feature sizes below 10nm. The second is a growing demand for laboratory based below 10 nm EUV reflectometry for fundamental studies of films, spectroscopic analysis of extreme state of matter and short wavelength filters and splitters. Combinations of La/B [23], LaN/B4C and La/B4C MLs [24, 25] are among the candidates for high reflectivity performances for the below 10 nm sources. However, further investigation of new material combinations and process optimizations are required to fulfil the performance requirements. Reflectivity of $\geq 70\ \%$ at near-normal incidence are required to enable the 6.x nm EUV lithography in order to print below 16 nm features on the IC wafers, while state of the art reflectivity performance stands at 64.1% measured at 6.65 nm wavelength and 1.5 degree off-normal incidence from La/B –based ML structures fabricated by hybrid thin-film deposition procedure [26].

1.3.2 Multilayers for astronomy

Walter based designs of X-ray telescopes [27] containing grazing-incidence mirrors of single layer coatings were sufficient for grazing incidence observation at low energy X-ray astronomy. However, focusing X-rays at energies greater than 10 keV becomes impractical with glancing incidence metallic mirrors because the critical angle for total external reflection is roughly proportional to $1/E$ [28], where E is the photon energy. This implies that the field of view and diameter of the optics decrease as $1/E$ resulting in small field of view and smaller diameter optics or longer focal lengths. This challenge was reversed by introducing multilayer coatings that enabled to extend X-ray focusing to higher energies. Moreover, advanced mathematical models of thin film growth, global optimization algorithms capable of searching the optimum structure inside a very wide domain of possible solutions and depth graded MLs are some of the legacies of X-ray astronomy that are useful in other parts of the EM spectrum.

EUV astronomy, considered as a successor of the X-ray astronomy, involves future solar missions that are designed to observe the sun in UV and EUV regime with easy extension to the visible range. Such solar missions in UV, EUV and visible spectral regime need multilayer coatings of high efficiency in such broad bandwidth of the EM spectrum. Carefully designed MLs give high near-normal reflectivity that enable full imaging of the extended solar corona [29]. As an example, spectroscopic and imaging analysis of the solar corona is possible by using innovative MLs with sufficient reflectivity performance at H I Lyman - α line (121.6 nm), He –II Lyman- α line (30.4 nm) and visible spectra. Such analysis enables to determine chemical composition of the solar corona, global map of solar wind outflow, relative density distributions of ions in the solar corona, insight into the origins of solar winds and origins of energetic particles [30, 31]. Thus far, multilayer-based instruments have been used in a number of major solar satellite instruments since the 1990's, including SoHO/EIT, TRACE, STEREO/EUVI, Hinode/EIS and SDO/AIA, and have flown in numerous sounding rocket experiments since the 1980's [32]. Some of the results to date include discovery of ionized hydrogen (electrons and protons) and helium (alpha particles) as dominant components in the solar corona. Moreover, trace amounts of heavy ions and atomic nuclei such as C, N, O, Ne, Mg, Si, S, and Fe ripped apart by heating of the Sun's outer atmosphere are detected [33].

In summary, future solar missions are planned to have very compact coronagraph, capable of imaging in UV, EUV and visible using just a single coronagraph module, stable over a continuous flux of solar-radiation and minimum loss of performance due to irradiation by ionized ions and particles that are common in the solar corona. This thesis contributes to the future solar missions by developing metrology techniques to study damage of MLs due to the irradiation of energetic particles that are dominant in the solar corona.

1.4 Interface roughness profiles in multilayers

Practically, interfaces of multilayers are neither sharp nor smooth. Under different film preparation conditions (substrate temperature, pressure, growth rate, presence of impurities, shadowing effects etc.) and different growth methods (physical and plasma vapor deposition, sputtering, chemical vapor deposition, nanocluster deposition, etc.), one may obtain a wide variety of different surface/interface morphologies and film microstructure which are inherently related to dynamic growth mechanisms. These, in turn, have a significant and generally different influence on physical properties, transmission and reflectivity performances. Specular X-ray and neutron reflectivity of rough interfaces decrease with $\sigma^{-\xi}$ where ξ can vary from 2 - 5, and σ is the root – mean square roughness as shown in Fig 1.8.

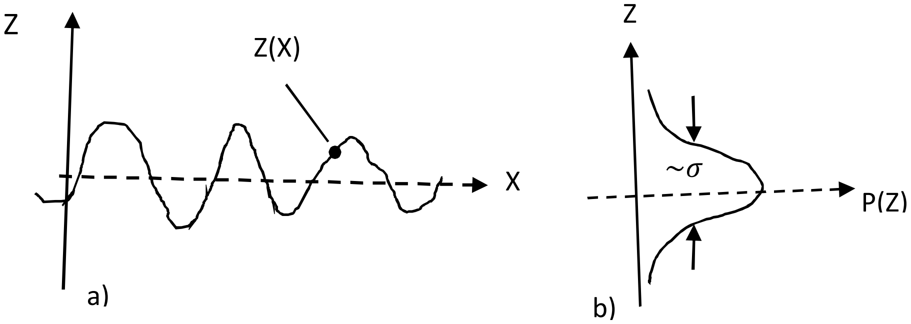

Figure 1.8: Interface roughness described by a profile function Z(X) as shown in (a) which varies with Gaussian statistics about the mean position of the interface, z=0. The standard deviation σ of the Gaussian probability density distribution P (Z) shown in (b).

Most commonly used correction factors during theoretical reflectivity calculations of rough surface are Debye-Waller ($\exp^{-2{q_o}^2\sigma^2}$) and Novet-Croce factors ($\exp^{-2q^2\sigma^2}$) where q_o is perpendicular component of incidence wave vector and q is perpendicular component of the wave vector in the material [34]. Both factors assume a Gaussian distribution of roughness heights at the surfaces and interfaces with the only difference that Novet - Croce (NC) takes average of the wave vectors in the two media above and below a given interface. NC can describe at low and high grazing incidence angles while the Debye – Waller (DW) describes well for low grazing angles. NC and DW are limiting cases of the generalized description of Distorted Wave Born Approximation (DWBA) for non-specular scattering [35]. Both NC and DW have limitations to account practical influences of neighboring atoms that make interface roughness not exactly Gaussian distribution. Such interface irregularity corrections are included at each interfaces between the “spacer” and “absorber” layers during reflectivity calculations or fitting to measured data. This method of accounting interface roughness is also known as two-layer modeling (i.e. the period contains only two layer pairs). However, when significant formation of interlayers are formed during the ML growth a four-layer modeling (i.e. the period contains four different layers) give better description of the structure and its optical properties [36].

1.5 Light scattering for single surface and multilayer interfaces

Light scattering techniques have long - standing history in quantifying surface finish by using longer wavelengths in visible, infrared and UV [37, 38]. Scattering measurements still maintain their demand as potential techniques in measuring roughness and defects of optical surfaces, thin films and multilayers in shorter wavelengths of EUV and soft X-rays in the increasingly miniaturized nanotechnology.

However, scattering experiments at EUV wavelengths are far more challenging as the scattering increases $\sim\frac{1}{\lambda^4}$. This implies that a surface categorized ‘smooth’ in the tradition long wavelength measurement can scatter significant amount of the incident radiation in EUV. In most cases, 3D scan of the scattered signals is required to obtain signature of a surface, which is time consuming for the industry. In line to the developments of short wavelength scatterometers, we describe in this chapter a simpler version of tabletop EUV scatterometer mainly targeted for angle resolved measurements.

1.5.1 Historical background of light scattering techniques

The most commonly used theories of surface scattering among many others are the classical Rayleigh-Rice surface scatter theory (1951) [39], the classical Beckmann-Kirchhoff surface scatter theory (1963) [40], and the generalized Harvey - Shack theory (1976) [41].

The classical Rayleigh-Rice surface scatter theory is a rigorous vector treatment (takes polarization of the incident and scattered light into account) valid for large incident and scattered angles; however it utilizes a perturbation technique with an explicit smooth-surface approximation and is limited in the case of rougher surfaces [42, 43].

The classical Beckmann-Kirchhoff (B-K theory) surface scatter theory is valid for rougher surfaces starting from Kirchhoff’s integral which gives the scattered light-field amplitude, but it has an inherent paraxial or small-angle limitation that restricts its ability to accurately account for both wide-angle scattering and large angles of incidence [44]. Vernold and Harvey [45] have modified the B–K theory to overcome this limitation. Their modification involves replacing the geometrical form factor of the B–K theory by a simpler Lambertian form. This extends the utility of the theory to large angles of both incidence and scatter [46].

Harvey and Shack (1976) developed a linear systems formulation of surface scatter phenomena in which the scattering behavior is characterized by a surface transfer function [47]. This treatment provided insight and understanding not readily collected from the above two theories, however, it suffered from the same paraxial limitations as the Beckmann-Kirchhoff theory. Later Krywonos and Harvey developed a linear systems formulation of nonparaxial scalar diffraction theory (1999) [48]. This led to the unified surface scatter theory that combines the advantages of the classical Rayleigh-Rice and the Beckmann-Kirchhoff theories that appeared to be valid for both smooth and moderately rough surfaces and at arbitrary incident and scattered angles known by the name generalized Harvey- Shack theory (GHS theory) [49]. By Fourier transforming the surface transfer function obtained by the GHS theory, one can calculate the BRDF (bi-directional reflectance distribution function) analytically since measurement of BRDF is challenging. BRDF calculations based on the GHS theory are required as an input to image analysis codes for increasingly short wavelengths (EUV and X-rays) that violet wavelengths smooth surface approximation implicit in the Rayleigh-Rice surface scatter theory. However, for surface roughness analysis, experimental measurement of BRDF is required. More conceptual and experimental definitions of BRDF are provided in section 5.3.

1.5.2 The Bidirectional Reflectance Distribution Function (BRDF)

In 1970, Nicodemus introduced a four-dimensional bi-directional reflectance distribution function (BRDF), a quantity that geometrically describes the scattering properties of a differential surface element. In general, it can be defined in radiometric terms as the reflected (scattered) radiance $L(\theta_s,\phi_s,\theta_i,\phi_i)$ divided by the incident irradiance $E(\theta_s,\phi_s,\theta_i,\phi_i)$, Eq.(1-12) [44].

$$BRDF= f(\theta_s,\phi_s,\theta_i,\phi_i) = \frac{dL(\theta_s,\phi_s,\theta_i,\phi_i)}{dE(\theta_s,\phi_s,\theta_i,\phi_i)} \tag{1-12}$$

Where (θi, ϕ_i) and (θs, ϕ_s) are the incident angle and scattered angle in conventional spherical coordinates.

Practically, BRDF can be measured for a small differential area element of a reflecting surface, ΔA, with a narrow beam of light at a fixed angle of incidence and measuring the radiant power by scanning a small collecting aperture over a hemisphere centered upon the normal to the surface element [48, 50] for the geometry given in Fig 1.9.

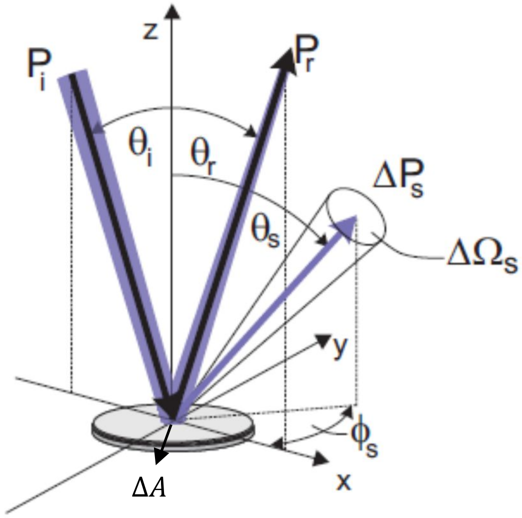

Figure 1.9: Illustration of the geometry used in defining the BRDF.

Under these conditions, the BRDF is approximated by dropping the differentials in Eq. (1-12) leading to the simpler Eq. (1-13).

$$BRDF = \frac{\Delta P_S/\Delta\Omega_S}{\Delta P_i \cos\theta_S} \tag{1-13}$$

Where ΔP_s is the radiant power scattered into the solid angle $\Delta\Omega s$ subtended by the collecting aperture, and ΔPi is the incident radiant power falling on the area element, ΔA. The total BRDF would consist of an infinite family of these two - dimensional scattered light distribution functions; one for every possible incident angle. The BRDF is also a function of the wavelength and the state of polarization of both the incident and scattered radiation. The total integrated scattering (TS) defined by the ratio of the power P scattered into the forward or backward hemisphere over the incident power P_I can be derived by integrating the BRDF function as in Eq.(1- 14).

$$\mathrm{TS} = 2\pi \int_0^{\pi/2} BRDF \cos\theta_s \sin\theta_s \, \theta_s \, d\theta_s \tag{1-14}$$

1.5.3 Angle resolved scattering measurements

Angle-resolved scattering (ARS) experiments are one of the available techniques in analyzing single optical surface roughness, interface imperfections of thin films and multilayer interfaces [51]. One can obtain the BRDF by multiplying the ARS by $\frac{1}{\cos\theta_s}$. In many applications, it is not only the amount of scattered light, but also the angular distribution of the scattered radiation that is important. James E. Harvey, et.al in ref [49] listed four major areas of applications where angular distribution of the scattered light is important: 1) The design and analysis of stray light rejection systems required by optical systems used to view a relatively faint target in the vicinity of a much brighter object, 2) the fabrication of “super-smooth” surfaces for high resolution X-ray and extreme ultraviolet (EUV) imaging systems, 3) inverse scattering applications where scattered light “signatures” are used to remotely infer target characteristics, and 4) the engineering of “enhanced roughness” to increase the efficiency of thin-film photo-voltaic solar cell applications.

For optically smooth metallic or dielectric single surfaces (Fig 1.10a), angle-resolved scattering is directly proportional to the 2D surface power spectral density (PSD) given in Eq. (1-15) based on the vector perturbation theory (VPT) [52, 53].

$$ARS(\theta_s, \varphi_s) = \frac{16\pi^2}{\lambda^4} cos^2\theta_s \cos\theta_i \, Q \, PSD\,(f_x, f_y) \qquad (1\text{-}15)$$

Where λ is the illumination wavelength, Q is an optical factor that is determined by the refractive index, scattering angles (θ_s), incidence angle (θ_i) and polarization states of illumination and detection. The validity of VPT, in many publications, is limited to surfaces with smaller micro-roughness compared to the wavelength [54, 55]. Under the smooth - surface limit approximation (i.e. when the surface/interface roughness σ is much less than the wavelength λ of the incident light), light scattering from a multilayer coating of rough interfaces as shown in Fig 1.10b can be theoretically calculated by Eq. (1-16) [56].

$$ARS(\theta_s) = \frac{1}{\lambda^4} \sum_{i=0}^{N} \sum_{j=0}^{N} C_i C_j^* \, PSD(f) \qquad (1\text{-}16)$$

Where C_i is an optical factor that contains the illumination and detection characteristics (polarization, incidence angle θ_i and scattering angle θ_s) as well as properties of the perfect ML (thickness, optical functions, etc.). The roughness properties of the interfaces ($i = j$) and their cross-correlations ($i \neq j$) are described by the PSD function.

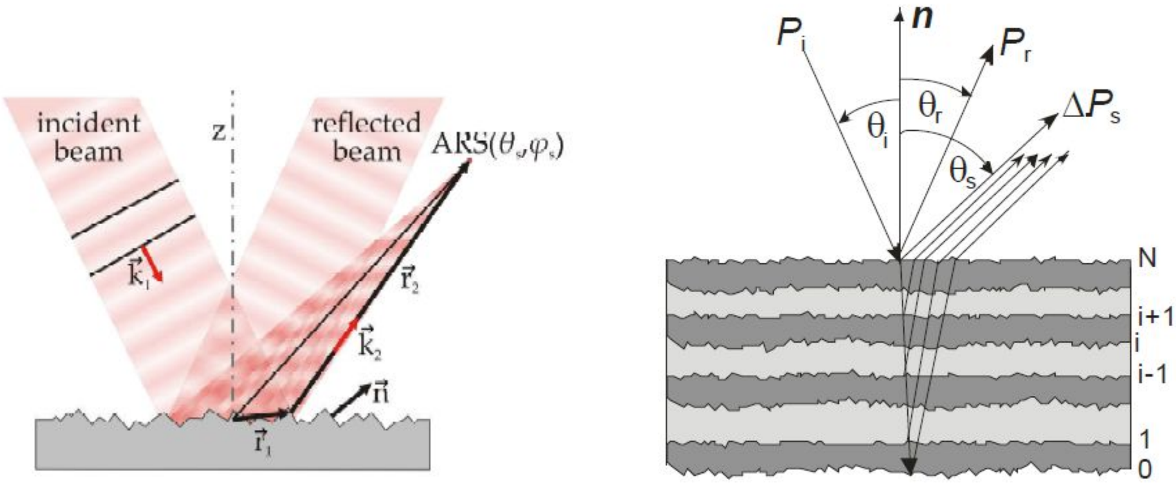

Figure 1.10: a) Single surface scattering geometry used in Beckmann-Kirchhoff theory. b) Basic geometry of scattering from multilayer structures of number of interfaces, .

However, calculation of ARS according to the inverse mathematical Eq. (1-16) is very challenging because the number of input parameters grows $\sim N^2$. Besides, optical and structural parameters of each interfaces need to be known beforehand. Therefore, direct measurements of ARS distributions from experiments are common practices. In such cases, ARS is defined by Eq. (1-17) similar to the BRDF.

$$ARS(\theta_s) = \frac{P_s(\theta_s)}{P_i \Delta\Omega_s} \tag{1-17}$$

Where P_s is the power scattered into the solid angle $\Delta\Omega_s$, normalized to the incident power P_i. The instrument geometry defines $\Delta\Omega_s$ as a function of the detector aperture and its distance to the sample.

There are different approaches of performing angle resolved scattering measurements. Goniometer based experimental systems are conventional set-ups for 3D ARS measurements in Synchrotrons and to some extent stand-alone in house laboratories [57]. Main advantage of such systems is flexibility, sensitivity and speed as well as a direct link to the optical performance at the working wavelength. Goniometer systems contains three main parts: the radiation sources, beam propagation/conditioning part and the experimental/detection chamber as shown in Fig 1.11.

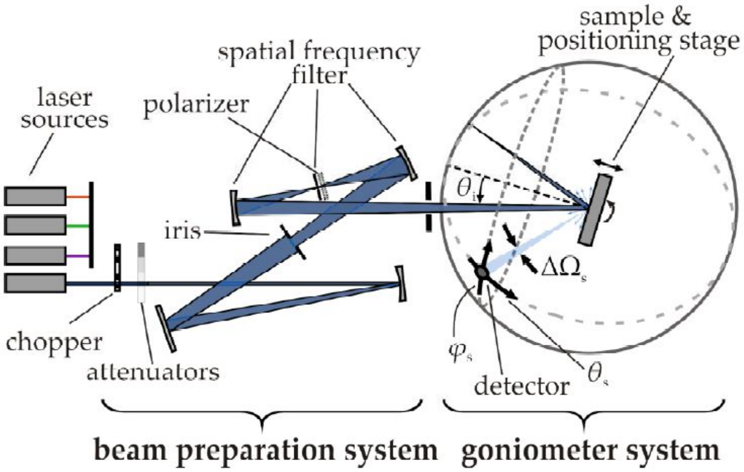

Figure 1.11: Scheme of stand-alone scatterometer developed at the Fraunhofer IOF- a typical goniometer based instrument for 3D-ARS measurements [51].

In Fig 1.11, the detector moves by one of the goniometer arms in a constant radius around the sample to capture angular distribution of the scattering. The disadvantages of goniometer systems are, however, time consuming and are availability is limited to the Synchrotron facilities. The alignment of goniometer systems is also challenging due to the number of degrees of freedom for sample adjustment, incidence and scattering angles, and polarization. The time-consuming measurements and alignment complexities make goniometer systems unsuitable for high volume quality assessment. Laboratory set-ups that perform in-plane 1D/2D scan are emerging. As part of the trends to have laboratory based scattering set-ups, a EUV scatterometer experiment based on high brightness discharge produced plasma (DPP) source is under development at the physics department of RWTH Aachen University. Chapter 5 of the thesis describes the experimental set-up and provides preliminary analysis of this grazing incidence diffuse reflection from surfaces and multilayers at incidence wavelength of 13.5 nm and 2% bandwidth.

2. MULTILAYER FABRICATION AND CHARACTERIZATION

The first part of this chapter describes theoretical basics of the two most common thin films and multilayer deposition techniques that are used to develop multilayers described in the thesis. The second part of the chapter explains a short summary of characterization techniques of thin films and multilayers.

2.1. Introduction on multilayer growth

In principle, any method for the deposition of thin films can be used for the fabrication of multilayer coatings. The deposition of EUV and soft X-ray reflecting periodic stacks of more than a hundred extremely thin and atomically flat layers requires a dedicated deposition technique. For many coatings, the quality of the boundaries is also the most important parameter for the performance of the coatings. Thicknesses are often shorter by a factor of 100 from conventional mirrors and boundaries have to be sharp within 1/10 of the multilayer period [58]. To successfully grow such layers, detailed knowledge and control is required on the surface science processes in general and processes of epitaxial growth and nucleation. So far, multilayer interference coatings for short wavelength applications have been successfully fabricated using evaporation, sputtering, epitaxial growth and laser – plasma deposition techniques [59].

There are three modes of epitaxial thin film growth at crystal surface or interfaces. Frank–van der Merwe (FM: layer-by-layer), Stranski–Krastanov (SK: layer-plus-island) and Volmer–Weber (VW: island formation) [60]. The basic differences among the three growth models are shown schematically in Fig 2.1.

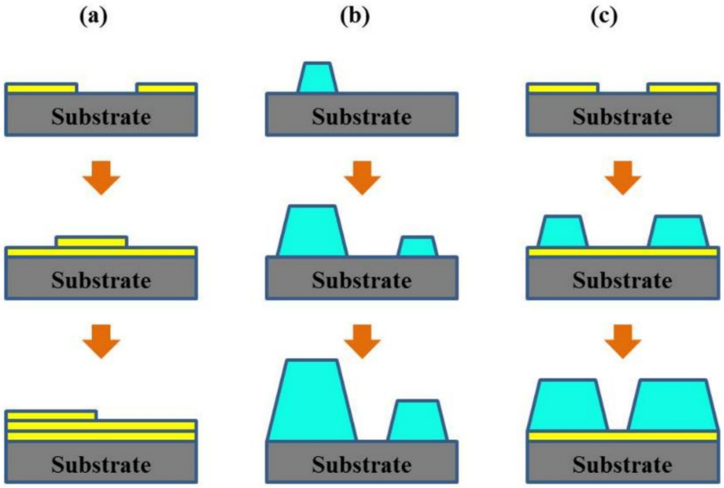

Figure 2. 1: Schematic diagram of three basic epitaxial thin film growth models: (a) layer-by-layer growth mode (FM); (b) island growth mode (VW); and (c) Stranski –Krastanov (SK) mode [34].

In Frank–van der Merwe (FM) growth, the deposited atoms (ad-atoms) attach preferentially to surface sites resulting in atomically smooth, fully formed layers. This layer-by-layer growth is two-dimensional, indicating that complete films form prior to growth of subsequent layers [61]. Nevertheless, this is only possible for a limited number of material combinations under very strict conditions. In Volmer–Weber (VW) growth, adatom–adatom interactions are stronger than those of the adatom with the surface, leading to the formation of three-dimensional adatom clusters or islands [62]. Growth of these clusters, along with coarsening, will cause rough multi-layer films to grow on the substrate surface. For hetero-epitaxial growth of layers from more than one materials with different structures, the SK model describes the process fairly [63]. The SK growth is an intermediary model between the FM and VW. 2D layer and 3D island growth characterize it. Transition from layer-by-layer to island-based growth occurs at a critical layer thickness which is highly dependent on the chemical and physical properties, such as surface energies and lattice parameters, of the substrate and film [64]. The experimental observations on Ge/Si systems seem to show a critical thickness of about 3 monolayers (ML) for pure Ge on Si substrate [65]. “In general, ad-atoms need energy to form smooth, dense and closed layers, but on the other hand, a too high ad-atom energy can activate a chemical reaction of the particle with the previous layer leading to compound formation at the interface, or cause penetration of the particle into the previous layer, resulting in enhanced interface intermixing. Ideally, one should be able to tune the particle energy to the different growth stages that are encountered: low in the initial growth part of the layer while increasing when the layer thickness increases [63]".

2.2. Multilayer deposition techniques

In layer deposition processes, thermal and kinetic energies of the ad-atoms are critical parameters in optimization of stack regularity, layer composition and interface structures. For multilayer growth from at least two different materials, the conflicting requirements of energies of the ad-atoms make the selection of a deposition technique that fulfils the requirements for all constituent materials challenging. High–performance EUV/Soft X-ray mirrors have been successfully deposited with different physical deposition techniques each having advantages and disadvantages. Of the many methods that have been applied, magnetron sputtering and electron beam evaporation are the most widely used. Further discussion on these two methods are provided in the subsequent paragraphs.

Electron beam evaporation (E-beam) is a Physical Vapor Deposition (PVD) technique whereby an intense, electron beam is generated from a charged tungsten filament and steered via electric and magnetic fields to strike source material (e.g. pieces of Co) at the crucible and vaporize it within a vacuum environment. At some point as the source material is heated via this energy transfer its surface atoms will have sufficient energy to leave the surface. At this point they will traverse the vacuum chamber, at thermal energy (less than 1 eV), and can be used to coat a substrate positioned above the evaporating material. Average working distances are 300 mm to 1000mm. Typical structure of an E-beam evaporator is shown in Fig 2.2.

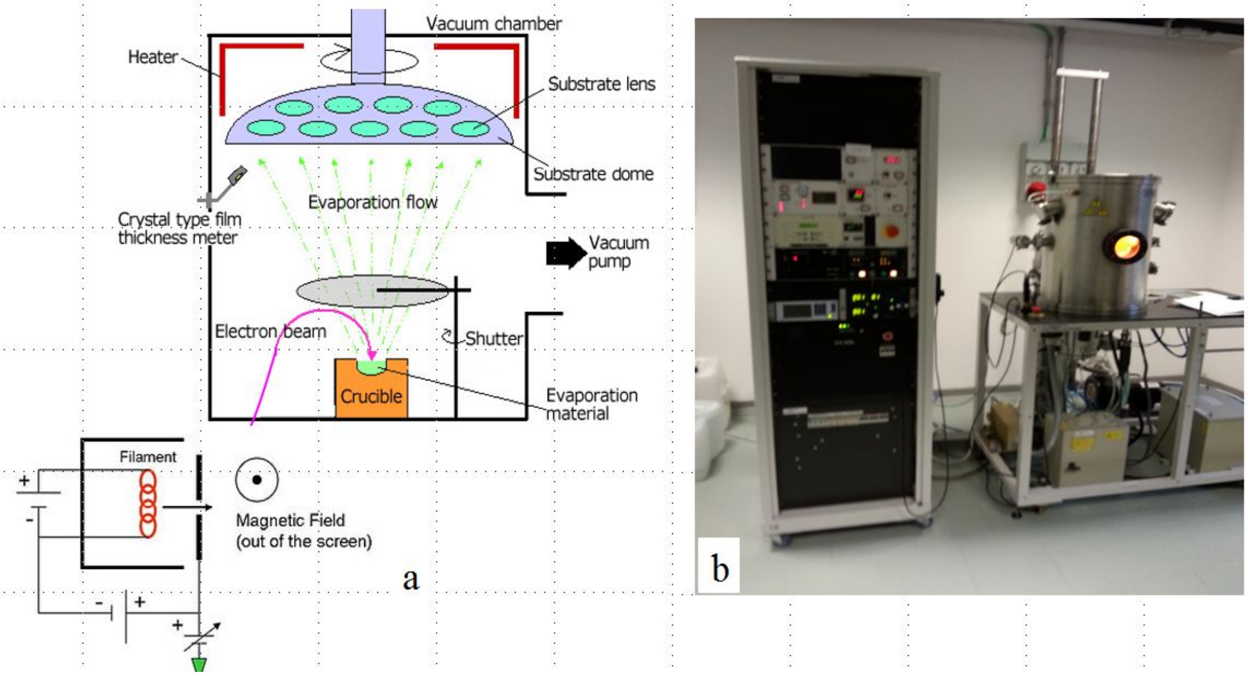

Figure 2. 2: a) Image of structure of an electron beam evaporation device; b) IONVAC e-beam and Joule evaporation system at CNR- IFN, Padova. Example: the recipe for e-beam evaporation of SiO2 in the industry is: Base Pressure: < 10-5 Torr, Emission Current: 150 to 200 mA, Sweep Size: Entire crucible Accelerating Voltage: 10 kV [66].

The E-beam machine consists of two main sections; an electron source (electron gun) and the deposition chamber. The electron source generates electrons through thermionic emission, field electron emission or the anodic arc method, accelerates them as electron beam, and deflect them via electric and magnetic fields into the crucible section that holds the evaporant material. The deposition chamber section is a low-pressure chamber where evaporation, transport towards substrate and deposition of target materials take place. Continuous source of heat energy from accelerating electron beams is required until the vapor pressure $P_{vapor} > 10^{-4}$ torr for most elements.

Early attempts to quantify evaporation phenomena, from the kinetic theory of gases, has led to the basic equation (Eq. 2-1) for the rate of evaporation Φ_{evap} from both liquid and solid surfaces [59].

$$\Phi_{evap} = 3.513 \times 10^{22} \frac{P_{vap}}{\sqrt{MT}} \quad \text{molecules/cm}^2 \text{ sec} \qquad (2\text{-}1)$$

Where P_{vap} is vapor pressure (torr), M is molecular weight and T is the temperature (°c). This equation can be converted to mass evaporation rate, Γ_{evap} as given in Eq. (2-2).

$$\Gamma_{evap} = 5.834 \times 10^{-2} \sqrt{\frac{M}{T}}\ P_{vap}\ \mathrm{g/cm^2\,sec} \tag{2-2}$$

Example: at $P_{vap} = 10^{-2}$ torr, mass flux = 10^{-4} grams/cm^2 sec.

While metals essentially evaporate as atoms and occasionally as clusters of atoms, the same is not true of compounds. Therefore, the vapor composition is usually different from that of the original solid or liquid sources. This causes a stoichiometric variation of deposited film from that of the source.

A related and highly vital parameter in E-beam deposition is the film thickness uniformity and purity. The deposition geometry mainly influences the ultimate film uniformity. Film thickness uniformity for point and surface source are given in Fig 2.3 [59]. The characteristics of evaporation sources (point vs surface sources), source-substrate distance (h), vacuum pressure and sample size can limit film uniformity. As can be seen from the evaporation geometry in Fig 2.3 (Inserted), maximum thickness d_0 grows at $\phi = 0$. For $\phi \neq 0$, film thickness d is less than the maximum.

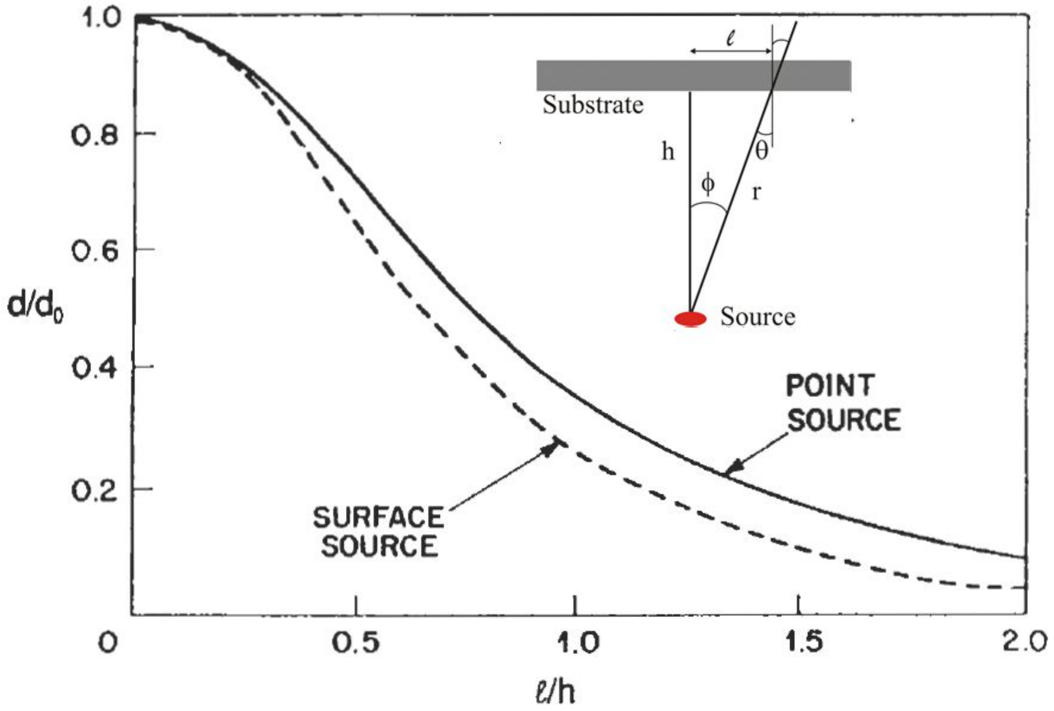

Figure 2. 3: Film thickness uniformity for point and surface sources. (Insert) is geometry of evaporation onto a parallel plane substrate [33].

Decreasing sample size (ℓ), increasing source–substrate distance (h), better vacuum, using multiple sources, moving substrate during deposition (e.g uniform rotation), put source and substrate on same sphere surface can enhance film uniformity in E-beam deposition.

The other Plasma Vapor Deposition (PVD) process most used today is magnetron sputtering. In magnetron sputtering, a plasma is created and positively charged ions from the plasma are accelerated by an electrical field superimposed on the negatively charged electrode or "target". The positive ions are accelerated by potentials ranging from a few hundred to a few thousand volts and strike the negative electrode with sufficient force to dislodge and eject atoms from the target. These atoms will be ejected in a typical line-of-sight cosine distribution from the face of the target and will condense on surfaces that are placed in proximity to the magnetron sputtering cathode, Fig 2.4

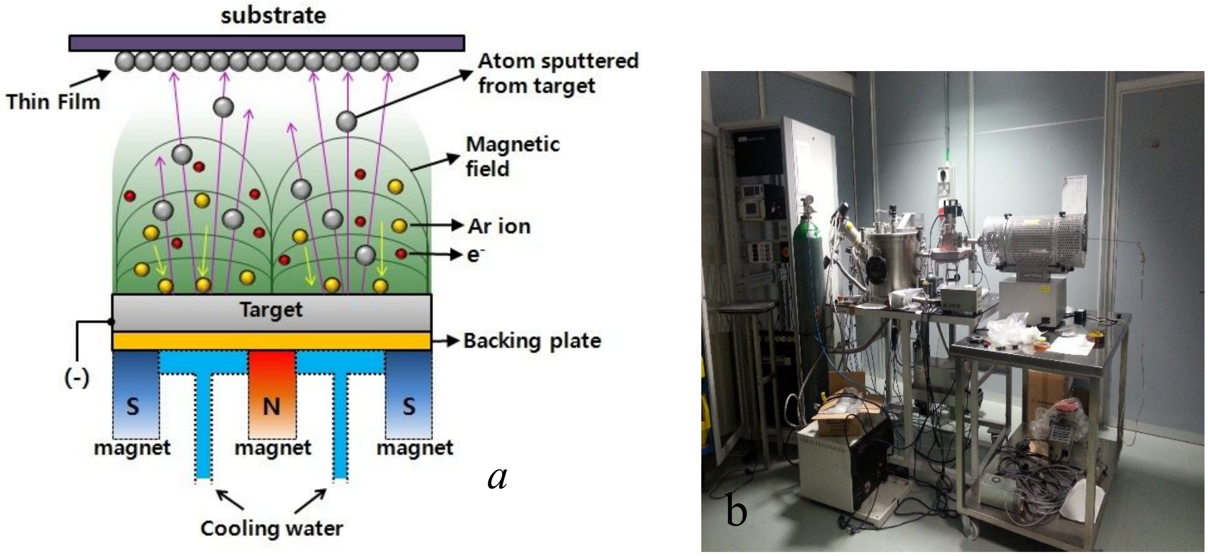

Figure 2. 4: a) principle of magnetron sputtering < http://marriott.tistory.com/120 > b) RF magnetron facility at CNR –IFN, Padova. A ‘standard’ process recipe for sputtering a thin film in NanoFab is: Base Pressure: less than 1x10^{-5} torr, Argon flow rate: 30 sccm (standard cubic cm/minute) (1sccm = 2.7x10^{19} atoms/cm^3), Argon Pressure: 7 mTorr, Power: 300 watts.

A very fundamental parameter in sputtering systems is the sputter yield, S. The sputter yield is defined as the number of atoms or molecules ejected from a target surface per incident ion and is a measure of the efficiency of sputtering. Theoretically, sputtering processes are described through a complex interaction of ions with surfaces, and there have been several theories to formulate the sputter yield. The currently accepted theory for the sputtering yield from collision cascades is due to Sigmund [66, 67] and predicts that

$$S = \frac{3\alpha}{4\pi^2} \frac{4M_1M_2}{(M_1+M_2)^2} \frac{E_l}{E_b} \qquad (E_l < 1\ \text{keV}) \tag{2-3}$$

$$S = 3.56\alpha \frac{Z_1Z_2}{Z_1^{\frac{2}{3}} + Z_2^{\frac{2}{3}}} \left(\frac{M_1}{M_1+M_2}\right) \frac{S_n(E)}{E_b} \qquad (E_l > 1\ \text{keV}) \tag{2-4}$$

Where M_1 and M_2 are molecular weights of struck atoms and target atoms respectively, E_l is the threshold energy required to displace an atom of the target, E_b is surface binding energy. These equations depend on two complex quantities, α and $S_n(E)$. α is a measure of efficiency of momentum transfer in collisions. $S_n(E)$ is related to reduced stopping power and is a measure of energy loss per unit length due to nuclear collisions. It is a function of the energy as well as masses and atomic numbers of the atoms involved. At high energy sputter yield is relatively constant because $S_n(E)$ tends to be independent of energy. Typical values of sputter yields for metals when sputtered with inert gases (He, Ar, Kr, Ne and Xe) of energies 0.5 - 1keV range from 0.01 to 4 and increase with mass and energy of the sputtering gas [59].

However, there is another crucial parameter that need great attention in sputtering processes; the film thickness uniformity. The film thickness uniformity is a crucial factor for optical and electrical applications of the various kinds of films such as metal, semiconductor and insulators that are prepared using sputtering systems. Generally, for different sputtering systems and different sputtering conditions, the characteristics of the thickness distribution are different. Thickness uniformity is influenced by a number of the process parameters such as working pressure, spatial distribution of the flow of sputtered atoms, sputtering power and temperature of the sputtering gas, type of target material, target – substrate geometry, substrate heating, ratio of rotation speed to revolution speed [68], etc. The good thing of sputtering systems is, however, that several studies have been conducted on identifying effects of each parameters on the film thickness uniformity both theoretically and practically, and thickness uniformities within $\pm 1-5\%$ are possible to obtain [69].

For researchers and engineers working on film and multilayer growth, it is often useful to know the differences of the E-beam and magnetron sputtering facilities in order to notice which one does better which. A summary of the difference is given in table 2.1.

Table 2. 1: Main differences between a sputter deposition system and E-beam evaporation system for the fabrication of multilayer mirrors [58].

Sputtering	**E-beam**
Stable rates	Deposition rates can vary
suitable sputtering for high melting point materials	Requires very high temperature for melting and this causes instability of rates
Thickness control by timing	Needs error compensation for the in-situ thickness monitor
Substrate holder rotates past sputter source	Needs shutter in front of the source
Good thickness uniformity requires large (>3.mirror size) chamber diameter	Good uniformity over large areas
Kinetic energy of deposition often > 100 eV can be adjusted	Kinetic energy smaller than 0.5 eV not adjustable
Surface smoothing can be performed by ion gas bombardment	Ion polishing added for smoother boundaries

It appears that sputtering is the method of choice when a large number of similar coatings have to be fabricated routinely. Once the optimum parameters for a material combination are determined, the deposition process can be easily automated. In contrast, the thermal deposition with in-situ monitoring requires more skills from the operator or more sophisticated he computer system to control the deposition.

2.4 Characterization methods of multilayers

Multilayer characterization is a measurement process to understand the intrinsic nature of multilayers. Understanding optical, electrical and structural properties of multilayers is crucial for the feedback chain of coating processes and for the development of multilayers of designed performances and stability. The characterization techniques in EUV and soft X-rays can have varied complexities based on various applications of the multilayers ranging from instrumentation for solar astronomy to plasma experiments and EUV Lithography. Besides, quantifications of physical parameters such as optical constants, uncertainty calculations of layer thicknesses and various structural parameters, quality check of interface profiles, influences of neighboring physical and chemical interactions require robust techniques. Thanks to the development of thin film growth and surface sciences, the numerous in-situ and ex-situ characterization techniques of thin films can be modified to measure multilayer parameters. Analysis techniques most commonly used for multilayer surface and in-depth investigation are summarized in table 2.2. The choice of a specific technique/s depends on several factors such as in-situ/ex-situ requirement, single film vs several layers, range of layer thickness and composition, temporal and spatial resolution required, and type of source available at hand, etc.

Table 2.2: Analysis techniques most commonly used for multilayer surface and in-depth investigation [70-74].

Techniques	Examples	Advantages	Disadvantages
Scanning probe microscopies	AFM	High lateral resolution	No in-depth information, material-independent
	STM	Very high lateral resolution, can distinguish materials	No in-depth information, needs conducting surface
	Profilometers	Fast capture of surface profiles	Low spatial resolution
Electronic microscopies	TEM	High in-depth resolution (best resolution)	Intensity scale has no calibration Expensive Difficulty in sample preparation Lacks large area statistical average
	STEM		
	FIB		
	HAADF		
	SEM		
Scattering methods	Elastic-X-ray scattering	-give structural information on the atomic length scale - Measure ensemble average in time - Enable in-situ film growth monitoring - high depth penetration - non-destructive and surface sensitive	Scatterings from multilayers need theoretical models For the electron /atomic scatterings, area ensemble is limited by the de-Broglie wavelength For multilayers, dynamical scattering models are required and then complexity increases
	Electron scattering		
	Atomic scattering		
	SAXS/WAXS		
Optical spectroscopies	Time-dependent dynamic reflectance (DRS)	Time average reflectivity Simple and non-destructive	Needs model for thick/several layer analysis
	Angle resolved reflectometer	Multi-angle analysis	
	Spectral-resolved normal reflectance	Exploits optical sensitivity Used for performance testing of multilayers	Overestimates at-wavelength sensitivity
	X-ray standing wave (XSW) analysis	-Supports XRR in thickness derivation	Not efficient for low Z elements and aperiodic multilayers because of low fluorescence yield

	XPS	Elemental specific, non-destructive	Limited depth penetration
Electron spectroscopies	EELS	Elemental specific, non destructive	Resolution less than TEM
	AES	Sensitive for chemical compositions	Only surface, no lateral resolution
	EDX	High material selectivity	Averages over large depth scales, limited lateral resolution

Table 2.2 is a brief summary of various techniques that can be deployed to retrieve certain parameters of multilayers. Further explanations of X-ray scattering are provided below since the interest of the thesis is on non-destructive and non-imaging metrology techniques of EUV and soft X-ray multilayers.

2.4.1 X-ray scattering methods

Elastic X-ray scattering, atom/ion scattering and electron scattering are particularly useful for real-time observation of thin film growth (i.e. in-situ monitoring), because they give structural information on the atomic length scale with a time resolution suited to growth dynamics. X-ray scatterings are performed at X-ray energies in the 10 keV range where the elastic scattering cross section is large and the wavelength of around 1.0 Å produce high depth resolution. It is worth noting that chemically selective scattering can be achieved by tuning the X-ray energy to specific atomic transitions (e.g Cu-K_{α} at 8 keV) where the scattering cross section is enhanced by anomalous scattering. X-ray methods are generally non-destructive, in that sample preparation is not required, and they can provide a very appropriate route to obtain structural information on thin films and multilayers. Typical set up of an X-ray diffractometer machine, where diffraction, scattering and specular reflection data are measured, is shown in Fig 2.5.

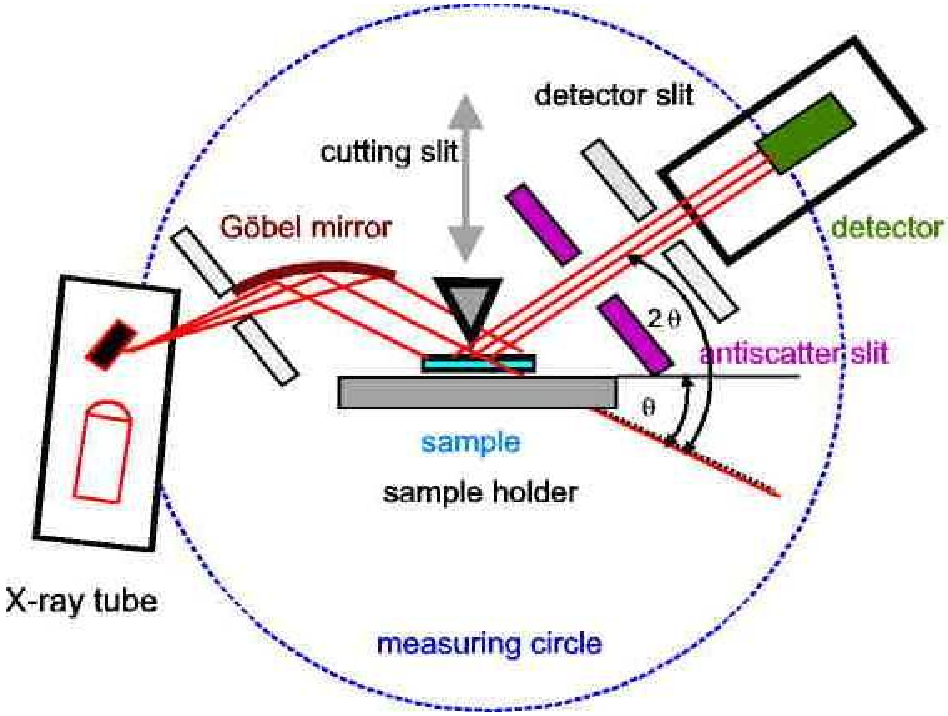

Figure 2. 5: Scheme of experimental setup <http://www.hzdr.de/db>

High - energy electrons in the ranges of 30 to 150 kilovolts impinge Cu, Mo or W targets and produce broadband bremsstrahlung and Cu Kα characteristic radiation (8 keV, 0.154 nm). Most of the unwanted bremsstrahlung radiation is removed with a parabolic multilayer mirror (Gobel mirror). Two channelled Si/Ge crystal monochromators (not shown in Fig 2.5) are used to improve the energy resolution and divergence angle. A 50–200 μm slit (cutting slit) positioned behind the channelled crystal monochromators restricts the size of the X-ray beam. A sample is placed on a sample stage that translates in three directions and rotates around three axes to enable different measurement requirements. Anti-scatter slit and detector slit are installed to minimize stray light and to limit the spot size received by the detector respectively. A fluorescing scintillator is used to detect the X-rays. The stimulated scintillator produces fluorescence that is collected and amplified by a photomultiplier tube to produce electronic signals. As a result, specular reflection, X-ray diffraction and diffuse reflection/scattering can be measured in the same diffractometer machine.

X-ray diffraction (XRD) is a powerful and convenient tool that measures diffracted intensity from crystal lattice planes. However, the new methods of material fabrication and emerging of artificial structures such as the multilayers have challenged the analysis of XRD data. Lots of works have been done on XRD from multilayered systems by many groups such as Fullerton and Schuller et al [75]. Nevertheless, because in XRD only the scattered X-ray intensity is measured and the phase information is totally missing, modeling is usually required to fit the measured intensity, and thus indirectly, the structures of samples may be obtained. The problem with modeling is that fits are not unique. Analysis even gets tougher for multilayer analysis of XRD peaks due to the unavoidable diffusions and formations of alloys, thickness fluctuations and other artifacts.

The specular X-ray scattering, which in effect is X-Ray Reflectivity (XRR), is another relevant technique for multilayer analysis. The basic idea behind the XRR is that beam of X-rays from a flat surface are reflected and intensity of the reflected X-rays in the specular direction are measured . If the interface is not perfectly sharp and smooth then the reflected intensity will deviate from that predicted by the law of Fresnel reflectivity. The deviations can then be analyzed to obtain the density profile of the interface normal to the surface. Fig 2.6 shows X-ray measurements of atomic layer deposited 16 –bilayer W/Al_2O_3 multilayer at Cu-K_{alpha} (8 keV) as reported in ref. [76].

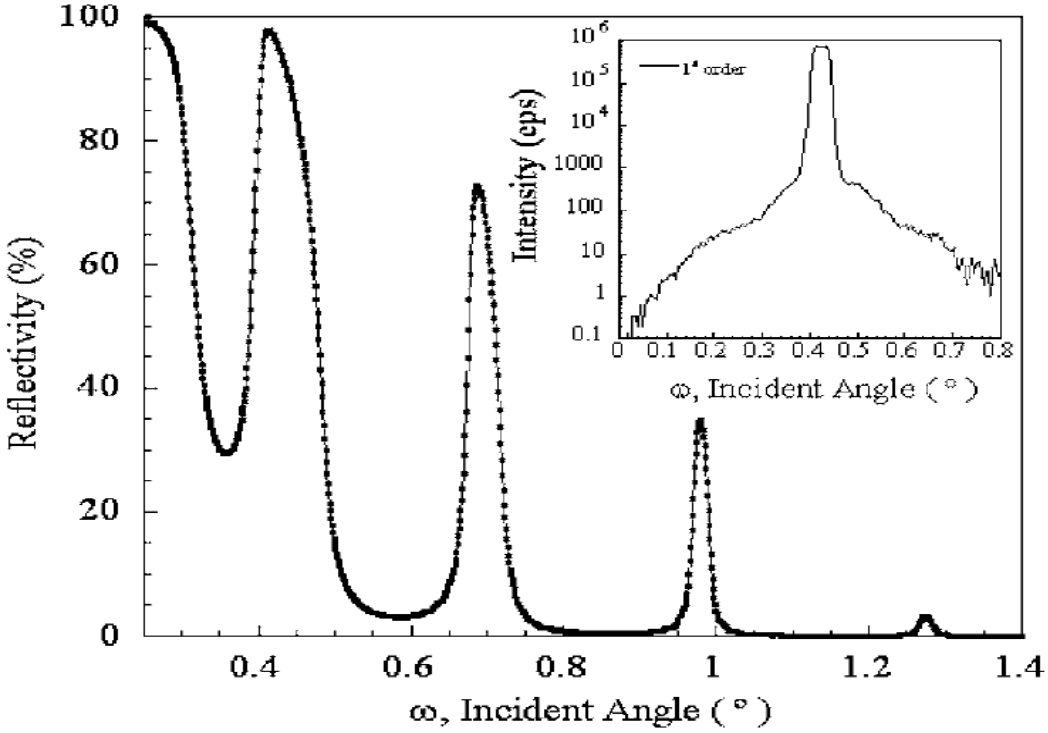

Figure 2. 6: Normalized X-ray reflectivity scan of a 16-bilayer W/Al_2O_3 multilayer at at Cu-K_{alpha} (8 keV). The inset shows an off-specular transverse scan (rocking curve) performed at the first-order Bragg peak for the 16-bilayer W/Al_2O_3 multilayer at at Cu-K_{alpha} [76].

From the XRR data of multilayers, thickness, density and interface roughness information can be retrieved by fitting to a mathematical model of multilayer reflectivity. Even with such model dependent analysis, the period of multilayers is determined with high resolution. However, buried interface diffusion and corresponding stoichiometric compositions of alloys need a technique with higher optical sensitivity than XRR. For optical and buried interface analysis of multilayers, Synchrotron based EUV reflectivity at photon energies near the absorption edges of elements give high optical sensitivity. The EUV reflectivity analysis in combination with XRR analysis are used in chapter 3 and 4 for the characterizations of Mo/Si and B4C/CeO2 multilayers coated in E-beam and RF magnetron sputtering facilities.

3. EUV AND SOFT X-RAY METROLOGY DEVELOPMENT FOR MULTILAYER ANALYSIS

3.1 Introduction to the GI-EUVR technique

Multilayer mirrors for reflection at EUV and soft X-rays have short periods, i.e. few nanometers. Individual layer thicknesses in the ML stacks are even shorter. Mo/Si MLs for the 13.5 nm EUV Lithography (EUVL) technology have a period of ~6.7 nm. Space applications for near normal reflectivity at 30.4 nm (He-Lyman – α line) demand MLs with period of less than 20 nm [77]. Next generation EUVL below 10 nm and tabletop EUV and soft X-ray reflectometry experiments will require MLs of period shorter than 10 nm. For such ML mirrors, actual optical properties at the working wavelength/s, thickness and interface control during deposition processes limit the reflectivity performances. Advanced facilities such as ALD (Atomic Layer Deposition), E-beam sputtering, RF - Magnetron sputtering and other atomic deposition facilities are required to deposit such short period MLs. On the other hand, in-situ and ex-situ measurement and characterization techniques are equally important as feedback loops to the facilities and as performance tests against theoretical simulations.

This chapter deals with simple, innovative and non-imaging experimental techniques for the characterization of EUV and soft X-ray multilayer mirrors. A Grazing Incidence EUV Reflectivity (GI-EUVR) near resonance edges of elements is described as a major technique for the analysis of optical properties, structural properties and interface profiles of ML mirrors. Further enhancement of the proposed method is performed by systematic combination of the GI-EUVR with X-Ray Reflectivity (XRR) measurements and electron imaging techniques.

This chapter commences with theoretical study of EUV optical responses near absorption edges for sensitive grazing incidence reflectivity measurements followed by experimental demonstrations. The potentiality of the GI-EUVR is further demonstrated through damage analysis of multilayer mirrors irradiated by energetic ions foreseen to be a useful technique in space applications.

3.2 EUV near absorption edge optical properties for multilayer characterization

The fact that most candidate elements have absorption edge energies in EUV and soft x-rays has demanded extensive studies on the optical properties and possible impact on multilayer design and reflectivity. Impacts of interface roughness, interface diffusion, fluctuations of optical constants and phases of inter-diffusion layers on the reflectivity of multilayers help to understand better the interaction of EUV and soft X-rays with materials of interest in this spectrum. In the theoretical analysis, two ML reflectivity models are explained depending on how the surface roughness and interface imperfections are accounted in the model. One is the statistical (two – layer) model and the second is interlayer (four – layer) ML model. In both cases, the theoretical analysis are performed near the absorption resonance edges of elements, which have high sensitivity to fluctuations of various design parameters. Tabulated values of optical constants of elements originally compiled by Henke and his co-authors [78] that are available at the at the Center for X-ray Optics (CXRO) database http://henke.lbl.gov/optical_constants/ are used for the theoretical calculations.

3.2.1 Statistical (two – layer) modeling of ML reflectivity

In this model, the reflectivity of multilayers is calculated based on recursive dynamical theory of Parrett with interface imperfections accounted by multiplying the Fresnel coefficients by an error function such as Debye-Waller factor ($\sim e^{-\frac{q_j^{2}\sigma_j^{2}}{2}}$) in the case of small roughness or Nevot – Croce factor ($\sim e^{-\frac{q_j^{2}\, q_{j+1}^{2}\, \sigma_j^{2}}{2}}$), where σ_j and σ_{j+1} are root mean square roughness and q refers to momentum transfer vector. The refraction corrected Bragg law is used to determine the relationship between grazing incidence angle (θ), wavelength (λ) and period (d) as follow in the two – layer model.

$$d = \frac{m\lambda}{2\sin\theta\left[1 - \frac{2\tilde{\delta}}{\sin^2\theta}\right]^{\frac{1}{2}}} \tag{3-1}$$

Where $\tilde{\delta}$ is the bilayer weighted real part of the refraction index and m refers to the diffraction order. Reflectivity of Mo/Si multilayers on SiO_2 substrate with d= 7nm, number of bilayers N =10 and optimized Γ −ratio to the wavelength of 99.4 eV (near Si - L_{III} edge) incident radiation are theoretically calculated using the two - layer model. Off- absorption edge reflectivity calculation is also performed for the sake of comparison with the near edge calculations as shown in Fig 3.1.

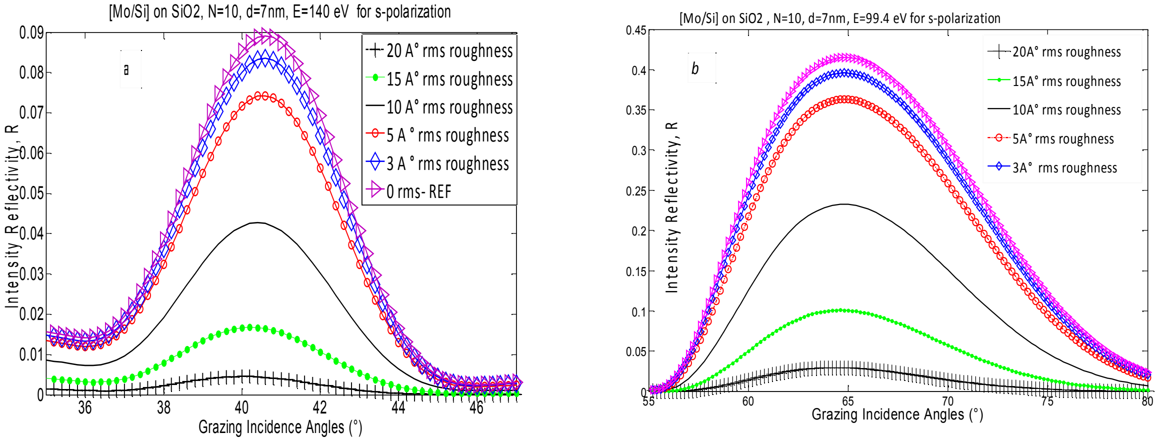

Figure 3. 1: Effects of interface roughness ($\sigma\ rms$) on the grazing incidence reflectivity of; a) Mo/Si multilayer on SiO2 substrate, $d = 7nm, N = 10$ at incident photon energy 140 eV ($\sim 8.86\ nm$); b) Mo/Si multilayer on SiO2 , $d = 7nm,\ N = 10\ at\ 99.4\ eV$ ($\sim 12.5\ nm$)

The impact of interface roughness on grazing incidence reflectivity of Mo/Si MLs is theoretically shown at two different incident photon energies (99.4 eV and 140 eV). Debye – Waller like interface error functions exponentially decreases reflectivity of MLs as the wavelength gets shorter. However, a shift in angle of the Bragg peak does not occur.

Similarly, impacts of fluctuations in optical constants on the grazing incidence reflectivity of Mo/Si MLs are provided in Fig 3.2. Optical constants of materials can be modified due to several factors. Deposition process imperfection, harsh working environment such as energetic ions bombardment, thermal loads, aging, chemical interaction such as oxidation are some of the factors which can bring about changes in optical constants which in turn affect reflectivity performance.

Capping [79] and Ion beam bombardment [80] are some of the technological solutions thus far implemented to sustain stability of MLs and increase reflectivity. To gain an idea of how much the reflectivity is affected by changes in optical constants (possibly caused by one or more of the above listed phenomenon) for a given theoretical modeling, 5,10 and 15% changes in δ and β of Si and Mo layers are introduced in the statistical model. First, Si layers are made to change (keeping δ and β of Mo layers constant) and vice versa. It is true that change in optical constants will cause changes in reflectivity for any wavelength in the EUV and X-Ray region. Nevertheless, at the near absorption edge it could be significant when the change is, for example, due to chemical interactions since the resonance scattering response is quite sensitive to local environment interactions.

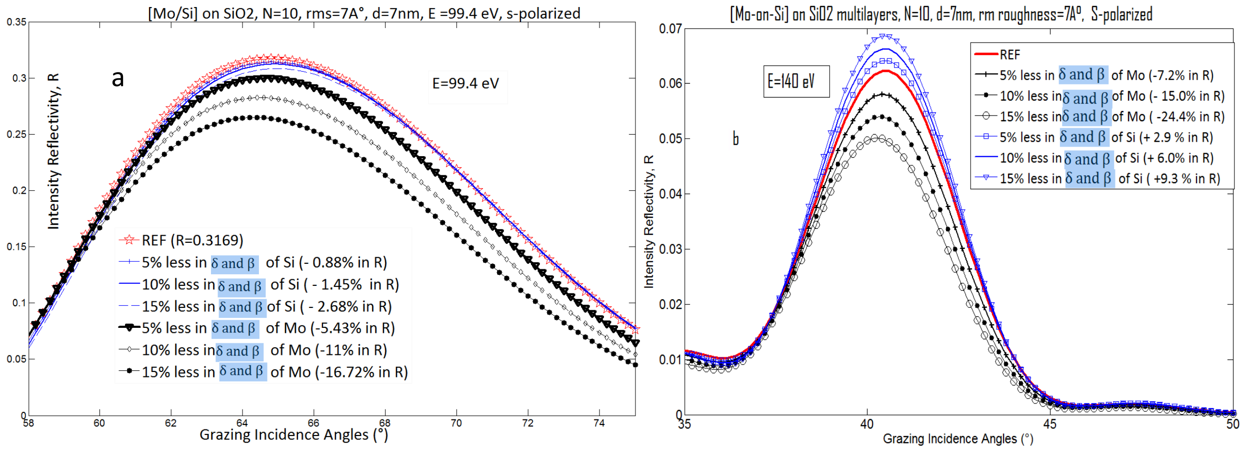

Figure 3. 2: 5, 10 and 15% change introduced to optical constants of Mo and Si layers independently; a) at incident photon energy of 99.4 eV; b) at 140 eV. δ *and* β of Si layers are changed first while that of Mo layers are kept constant, and vice versa. This way the impact of fluctuations of optical constants of Si layers and Mo layers can be determined independently.

At 99.4 eV, 10% decrease in δ and β of Mo layers resulted in 11% change in reflectivity while 10% change in Si layers caused 1.45% loss in reflectivity. At 140 eV, 10% decrease in δ and β of Mo layers resulted in 15% change in reflectivity while 10% change in Si layers resulted in 6% loss. In general, reflectivity of the model for wavelengths near the Si L_{III} edge have shown higher tolerance to changes of optical constants of Mo and Si layers. It is also vivid that near the Si edge (i.e. at 99.4 eV), tolerance to changes in δ and β of Si layers, compared to the same changes in Mo layers, is high. This is indeed useful finding in optimizing numerical fitting procedures of reflectivity curves for Si based MLs near its EUV edge.

In summary, statistical model gives useful insight for the theoretical analysis of ML reflectivity. However, it is limited when inter-diffusion layers are formed. Thus, a different model not just based on two-layer system but four-layer system is theoretically studied below for MLs with inter-diffusions.

3.2.2 Four - layer modeling of ML reflectivity

In practice, ML interfaces are neither smooth nor sharp. The two – layer system (aka interlayer modeling) is just a simplified version. Several scenarios result in intermixing of layers during and after deposition of MLs even although inter-diffusion during deposition process is a major cause. In either cases, to be able to characterize MLs with inter-diffusion regions is paramount important as a feedback to the manufacturing process and study impacts of parameters on the shape and value of the reflectivity curves. The four - layer model is explained in Fig 3.3. In this theoretical modeling, a period (d) consists of layer 01 + interlayer -01 + layer 02 + interlayer -02 as indicated in Fig 3.3a. The interface region can be characterized by an interface profile function, p(z), and an interface width, σ, as illustrated schematically in Fig 3.3b.

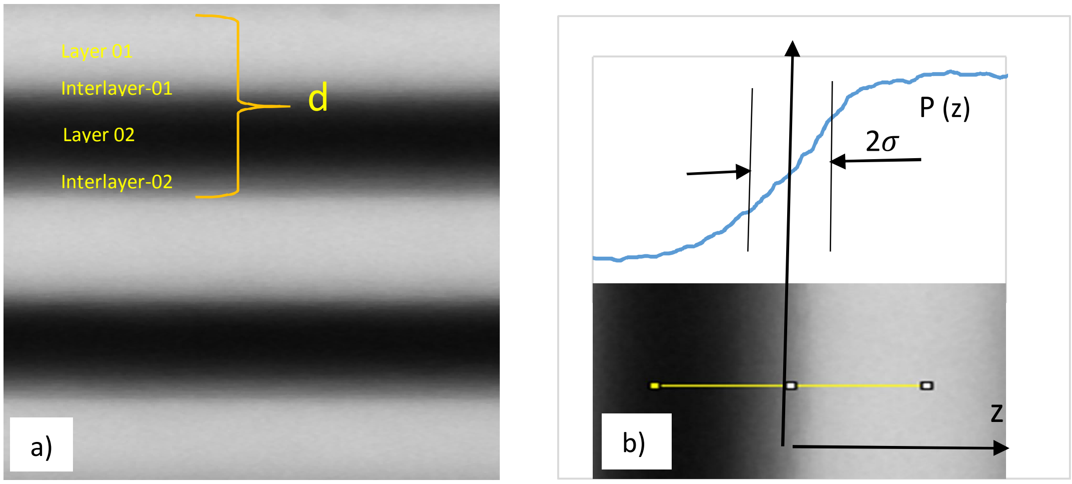

Figure 3. 3: Four – layer modeling of MLs with enhanced inter-diffusion at interfaces.

Again, Mo/Si MLs on SiO_2 substrate with $N = 4$, d = 7nm, Mo and Si layer thicknesses 2.3 nm and 2.9 nm respectively. The introduced inter-diffusion (interlayer) regions in the modeling have $1nm$ for the Mo – on - Si and 0.8 nm for Si – on – Mo interfaces. Analysis include effects of interlayer thicknesses, period thickness fluctuations and effect of stoichiometric phases of interlayers on the reflectivity curves. First result, which deals with impact of interlayer thicknesses at two photon energies, is given in Fig 3.4

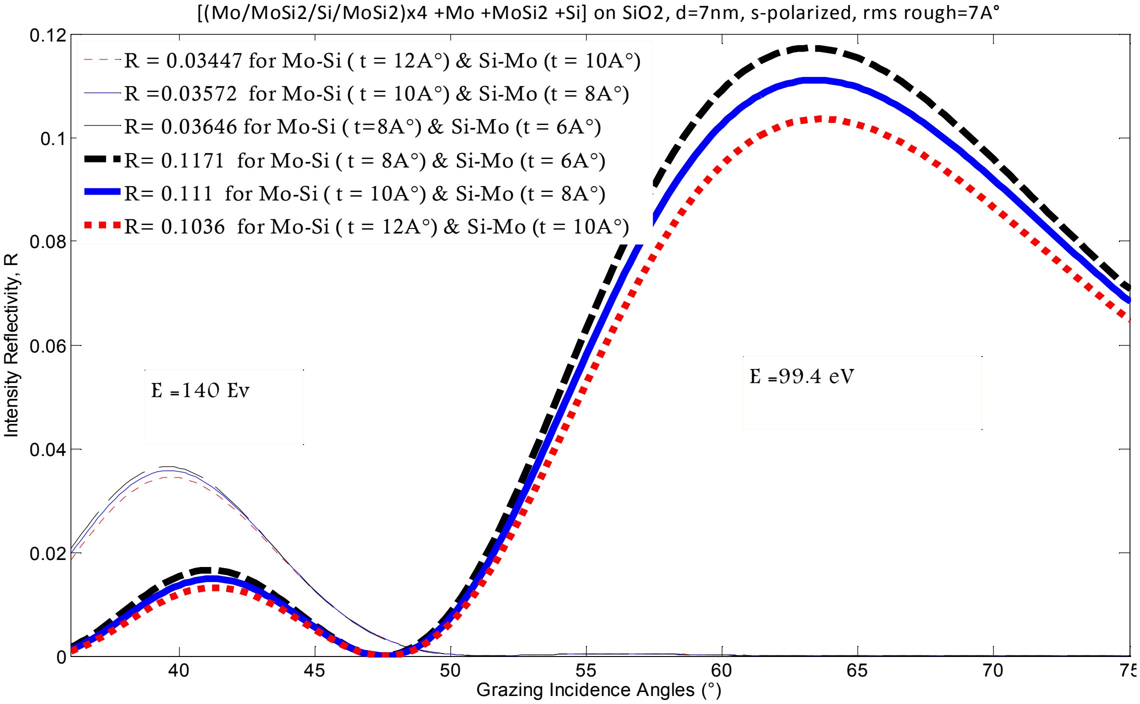

Figure 3. 4: Reflectivity from $[Mo/MoSi2/Si/MoSi2]_{\times 4}$ + Mo +$MoSi_2$ + Si on SiO_2 substrate for different interlayer thicknesses at two different photon energies (140 and 99.4 eV) while the period (d) is kept constant.

At 99.4 eV (near Si L_{III} edge), 2Å change in interlayer thickness resulted in an average change of 6.7% in reflectivity (R) while for the 140 eV (a bit off the Si edge) an average change in reflectivity of 3.8% is noted. Clearly, the Bragg peak at 99.4 eV demonstrates high sensitivity to slight changes in thickness of interlayers. Such thickness sensitivity near the EUV absorption edge is vital for ML characterization in EUV and soft X-rays as will be explained shortly. The other interesting observation in Fig 3.4 is that as long as the period is kept constants, variation of interlayer thicknesses does not cause redistribution of reflectivity peaks. In fact, Fig 3.5 below confirm that peak redistribution is inevitable when the period of the ML structure changes.

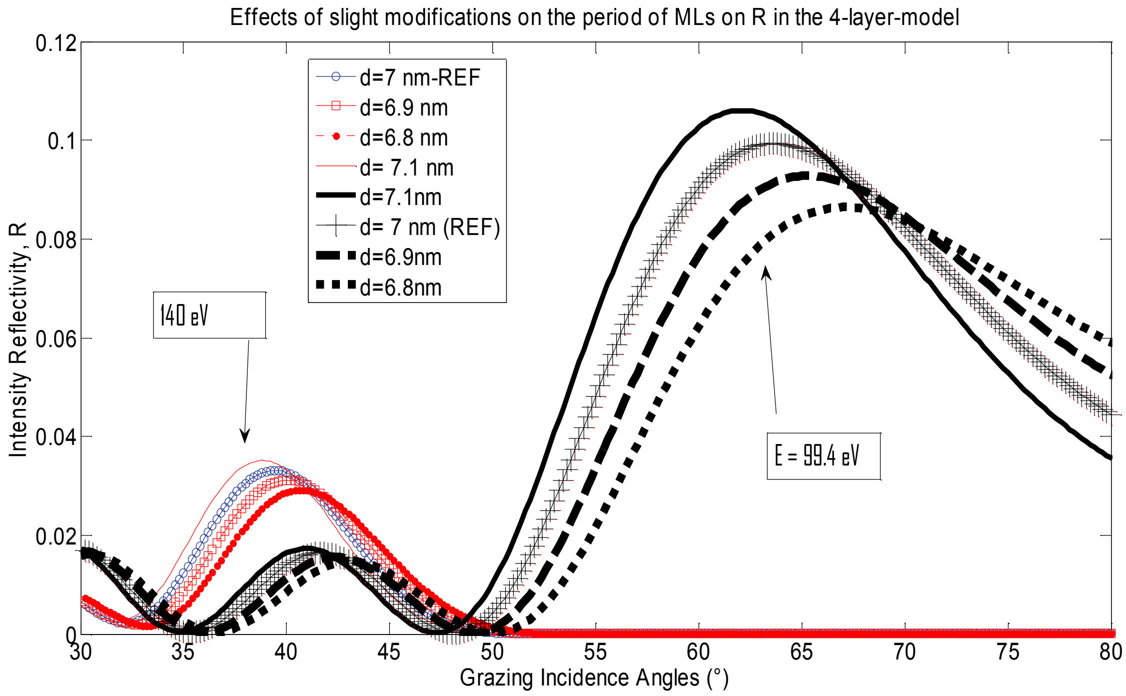

Figure 3. 5: Effects of slight changes in period thickness on the reflectivity curve at two photon energies. The sensitivity is high for both energies with more pronounced sensitivity at the near absorption edge (i.e. at 99.4 eV)

Another important property investigated in the four - layer ML structure is the impact of tailoring δ and β of the interlayers, Fig 3.6. For Mo/Si MLs there is a possibility of $MoSi_2$, Mo_2Si_3 or Mo_3Si_5 phases appearing as interlayers depending on the deposition quality and process parameters. Measured δ and β of Mo_2Si_3 or Mo_3Si_5 are not available in the literature. Therefore, a theoretical calculation of refractive index (n) of materials for X-rays Eq. (3-2) and (3-3) are adopted for EUV and soft X-rays. According to this method, δ and β are calculated by taking real and imaginary scattering factors f_1^o and f_2^o respectively and weighted average of constituent elements.

$$\Delta=\left(\frac{r_e\lambda^2}{2\pi}\right)N_0\rho\ \sum_i x_i\left(Z_i+f_1^0\right)/\sum_i x_i M_i \qquad (3\text{-}2)$$

$$B = \left(\frac{r_e \lambda^2}{2\pi}\right) N_0 \rho \ \sum_i x_i \left(Z_i + f_2^0\right) / \sum_i x_i M_i \qquad (3\text{-}3)$$

Where r_e is classical electron radius (2.82×10^{-9} nm), N_0 is Avogadro number (6.022×10^{23}), λ is the wavelength , ρ is density (gm/cm^3), Z_i refers to atomic number of the ith atom, M_i is atomic weight of the ith atom and x_i is the atomic ratio (molar ratio) of the ith atom.

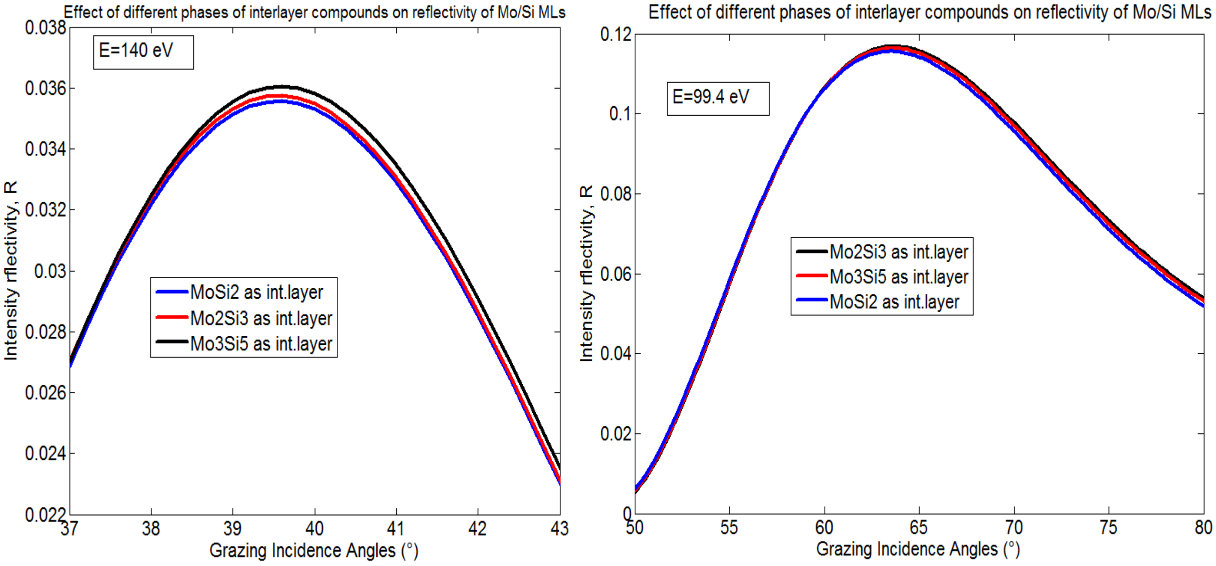

Figure 3.6: Sensitivity of the four-layer model to various compounds (alloys) of interlayers. Interlayers of stoichiometric ratio MoSi2, Mo2Si3 and Mo3Si5 are simulated for both 99.4 eV (right) and 140 eV (left).

The sensitivity of the four-layer model for these compounds is tested. What the model is trying to differentiate is the optical constants of those compounds. The optical constants of each compounds are calculated by taking the weighted average of its constituent elements[11]. The period is kept at 7 nm, Mo and Si layer thicknesses are 2.3 nm and 2.9nm respectively, interlayer thicknesses considered in this simulation are 1nm for the Mo-on-Si and 0.8nm for Si-on-Mo.

3.3 Grazing incidence EUV reflectivity for the analysis of multilayers

In EUV and soft X-rays, accurate measurements of optical properties of multilayer mirrors (MLs) and chemical compositions of inter-diffusion layers are yet particularly challenging. The theoretical analysis in section 3.2 have signaled significant potential of the EUV and soft X-ray near absorption edge optical response in characterizing MLs. In this section, experimental measurements are performed to validate the theoretical analysis.

The experiments base on EUV reflectivity measurements at photon energies near the resonance absorption edge of the low-Z element in the ML structure. The experimental setup is designed to make at-wavelength reflectivity measurements in a grazing incidence setup analogous to that of XRR. The method is called GI-EUVR (Grazing incidence EUV reflectivity). It benefits from the underlying physical phenomenon of abrupt optical responses near EUV resonance edges and wide grazing measurements that consists of several Bragg peaks. This way, optical and structural parameters of MLs can be derived with high sensitivity and reliability. Nevertheless, the major advantage of the method is a possibility to perform detailed quantitative analysis of buried interfaces of multilayer structures in a non-destructive and non-imaging setup. The method is also used to analyze the damage of ML mirrors exposed to energetic ions that are of interest to the solar coronal studies.

Following the theoretical analysis described in section 3.2, coatings of Si/Mo multilayers on Si substrate are investigated using the GI-EUVR method for demonstration of its strength. Si/Mo MLs are chosen for the demonstration because properties of these structures have been widely studied. Atomic scattering factors of elements starting from atomic number Z=1-92 have been measured by Henke and his co-authors in the energy ranges E=50 - 30,000 eV [78]. Significant work on the design and characterization of capping layers of Si/Mo mirrors for EUVL application [81, 82] by Sasa Bajt et.al, mitigation of substrate defects in reticles using ML buffer layers by B. Mirkarimii [83], Mo/Si ML components for high harmonic generation sources applicable in EUV by Eric M. Gullikson [84] are among the studies directly or indirectly contributing to the Mo/Si MLs for EUVL applications at 13.4 nm wavelength.

The Si/Mo MLs and corresponding capping structures (see Table 3.1) discussed here were designed for applications in solar missions, in particular for the development of an imaging instrument for SOLO ESA missions [85, 86] that is expected to reach as close as 0.28 AU (at the perihelion minimum) from the Sun.

Table 3.1: ML design parameters and capping layer[a]

Capping layer structures		
CL1	CL2	CL3
Si (18.72 nm)	Ir (2.0 nm)	Ir (2.0 nm)
Mo (3.5 nm)	Mo (2.2 nm)	Si (15.4nm)
		Mo (2.95nm)
Sample_01	Sample_02	Sample_03
Si substrate		

[a] Three ML samples with same interior structures but different CLs.

The GI-EUVR measurements at 99 eV photon energy were carried out at the BEAR (Bending magnet for Emission, Absorption and Reflectivity) beamline of ELETTRA Synchrotron in Trieste [87]. The BEAR beamline offers a spot size of 400 μm FWHM in horizontal and 100 μm in the vertical, angular resolution accuracy of $0.1°$, linear polarization of $\geq 90\%$ at the considered photon energies, and relative energy resolution $E/\Delta E$ =3000 in the range $40-1600$ eV. The stability and reproducibility of the beam energy coupled with the high - accuracy control of the beam-line facility operation and measurement processes allowed for increased accuracy and reliability of experimental data analysis. In addition to that, XRR measurements at hard X-ray photon energy (Cu $K\alpha$ – 8.0 keV) have been performed using X'PERT-PRO diffractometer system [88] (voltage and current sources of 40 kV and 40 mA respectively in θ - 2θ scan mode). The XRR source has a beam divergence of 0.03125 degrees in the incidence plane.

Numerical reconstruction of ML parameters from reflectivity measurements is an inverse process and ML model and algorithm dependent. Basic explanations of the software, reflectivity model and optimization algorithms used to reconstruct the ML parameters are described below. Reconstruction of ML parameters from both XRR and GI-EUVR are performed using IMD software package (http://www.esrf.eu/Instrumentation/software/data-analysis/xop2.3) that can yield both specular and non-specular (diffuse) optical functions [89]. A nonlinear curve fitting to measured reflectivity curves against a goodness of fit parameter chi-square (χ^2) similar to that of Pearson´s criterion [90] retrieves almost any parameter of a ML. A common practice of curve fitting in IMD embraces generation of independent or joint confidence intervals to assure fit parameter values are in the properly derived allowed ranges (confidence intervals) associated with the best curve fitting, based on methods given in [90, 91]. In IMD, confidence intervals are calculated in either Marquardt or Levenberg-Marquardt gradient-expansion algorithms. For MLs considered here, the nonlinear curve fitting in IMD is repeated until the probability of finding fit parameter values within the confidence intervals reach 90 - 98 %. Therefore, the discrete thickness and optical constants given in tables and figures are determined with 90 - 98% probability of finding them within the confidence intervals.

Parratt's dynamic reflectivity model of MLs and Debye-Waller like factor ($\sim e^{-\frac{q^2\sigma^2}{2}}$) to account interface irregularities, where σ is rms roughness and q refers to momentum transfer vector, are chosen for the numerical calculations of reflectivity in IMD [89]. Genetic Algorithm (GA) and a more complex form of it known by Differential evolution (DE) are alternatively used in the fitting optimization. Detailed description of the GA has been published in [92]. GA is considered as a global optimization algorithm as it is generally less sensitive to the choice of initial parameter values and less susceptible to stacking at local minima even if the function contains more than one peaks. In contrast to other methods GA combines a stochastic search of global minima in a parameter space with intelligent strategy of solution finding [93]. But also, a manual tuning of parameters to visualize in real time the resulting effect on reflectance were performed based on previous work reported in [94] to set initial parameters values relatively close to the final values. A combination of the robust GA and possibility of manual parameter tuning has made IMD versatile software that several ML parameters can be iteratively tuned during fitting. Layer and interlayer thicknesses, optical constants, interface diffusion layers and their stoichiometric compositions can be retrieved. To minimize numerical uncertainties due to the number of free parameters, period of MLs as obtained from XRR analysis is fixed in the GI-EUVR fittings. Besides, the $\Gamma -$ratio enables to choose ML structure models based on four-layer system (i.e. layer 1+ interlayer_01 +layer 2 + interlayer_02) due to the interfaces diffusion. For such ML model, a basic roughness of 3 - 5Å suffices to account interface irregularities between interlayers and layers [95].

Following the above nonlinear curve fitting strategies, XRR measured and fit curves at Cu K_α energy are provided in Fig 3.7a and Fig 3.8a for sample_01 and sample_02 (Table 3.1) respectively.

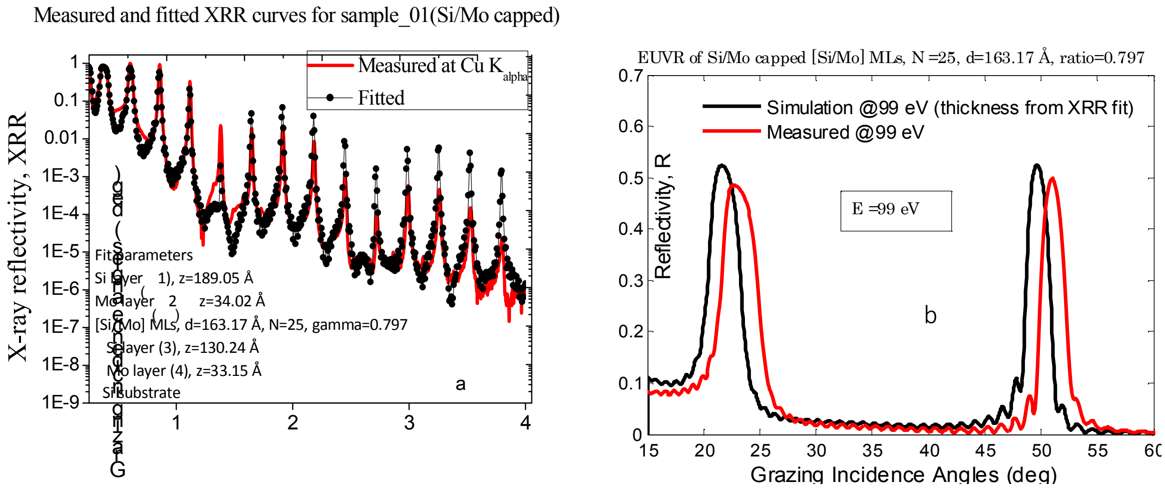

Figure 3. 7: a) Measured and fit curves of XRR for sample_01 with Si/Mo capping structure. b) Measured and simulated reflectivity at EUV (99 eV) for sample_01 with simulation thicknesses taken from XRR fit. Note that Ґ refers to ratio of Si layer to the period.

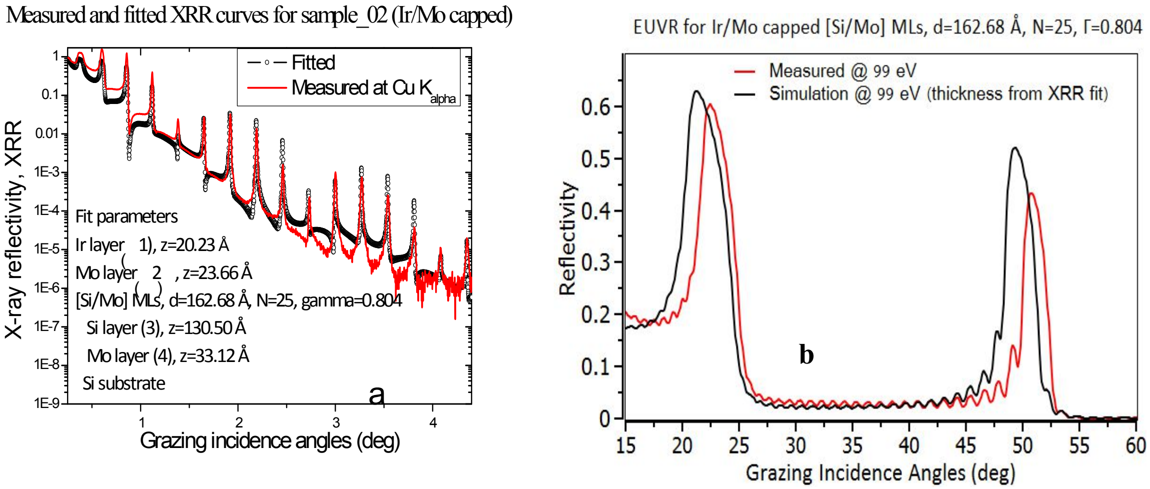

Figure 3. 8: a) Measured and fit of XRR curves in IMD for sample _02. b) Measured and simulated reflectivity at EUV (99 eV) for sample_02 with thicknesses taken from XRR fit. Note that Ґ is ratio of Si layer to the period.

The simulated and measured GI-EUVR curves of sample_01 and sample_02 are also given in Fig 3.7b and Fig 3.8b respectively. The GI-EUVR caclulations near the Si resonance edge (~ 99 eV) for all the samples are performed by adopting period and layer thicknesses as dervied from the XRR analysis.The comparison shows a clear misfit between the measured and simulated GI-EUVR curves.

XRR fit for sample_01 (CL1) gives a period of 163.17 Å, and $\Gamma - \mathrm{ratio} = 0.797$ (Fig 1a) while for sample_02 (CL2) gave a period d = 162.68 Å and $\Gamma = 0.804$ (Fig 2). Similarly for sample_03 (with CL3) the period is determined to be 162.80 Å, and $\Gamma = 0.801$. Period, layer thicknesses and interface roughness are the only input parameters during the fitting. In all cases, interface roughness of 2 - 4 Å give better fit of the measured XRR curves. For all the three ML samples, numerical fits to XRR measured data at Cu $K\alpha$ (~8.0 KeV) returned ML thickness ratios ($\acute{\Gamma}$-ratios) different from the design value $\Gamma = 0.82$. This can be considered as indication of formation of interlayers between Si and Mo layers having intermediate optical constants [96]. As an independent evidence for the formation of interlayers at the interfaces of a representative Si/Mo ML structure shown in Fig 3.9 and discussed in [85] was demonstrated from high - spatial resolution transmission electron microscopy (HR-TEM) image. That sample was deposited in the same RF sputtering facility at the RXO LLC (N.Y. USA) deposition facility under similar ultra-high vacuum, pressure and temperature conditions as the samples discussed in this section. There is only a slight difference in number of bilayers (N) compared to the current samples.

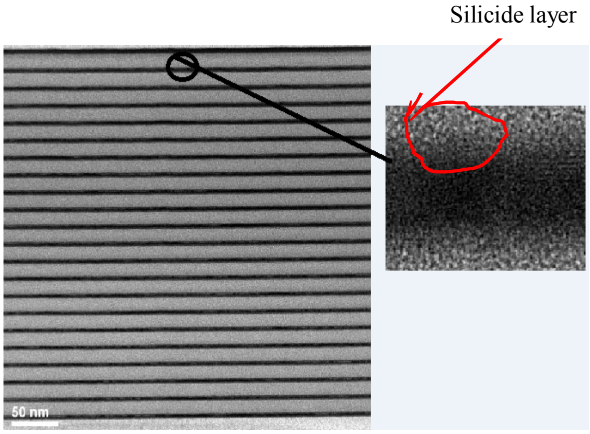

Figure 3. 9: High-spatial resolution transmission electron microscopy (HR-TEM) image of a Si/Mo ML discussed in [85]. The onset shows interface at the top of the ML structure.

To reach at reasonable fits to the measured GI-EUVR curves (i.e. to avoid the misfits in Fig 3.7b and Fig 3.8b), the four – layer ML model described in section 3.2 is introduced to account the interdiffusion (interlayers). In such four-layer modeling of MLs, 3 -5 Å surface finish and interface imperfection are accounted by the basic Debye-Waller like interface errors produce good fits to the Bragg peak intensities.

Note that periods of MLs derived from XRR data analysis are used during the GI-EUVR data-fitting algorithms. Therefore, only optical constants and thicknesses of each layer and interlayer eventually become the only input parameters during the GI-EUVR fitting. The fitting returns optical constants of the diffusion layers from which stoichiometric composition can be retraced. Optical impacts of physical and chemical interactions on any of the ML layers, especially layers on the top exposed to air, can be achieved by comparing fit results with measured values in the literature. For Si and Mo, derived optical constants are easily compared with measured values by Henke et.al in [14] and [97] respectively, here after referred as CXRO database. However, only derivations of δ values are discussed in this work due to the high sensitivity of EUV and soft X-ray reflection measurements to it. Approximate values of β's are also given but with less accuracy and thus not discussed here. First result of best fitting to GI-EUVR data curve is given in Fig 3.10 for sample_01. For this sample, optical constants for each layer and interlayer obtained from the numerical fitting are summarized in table 3.2.

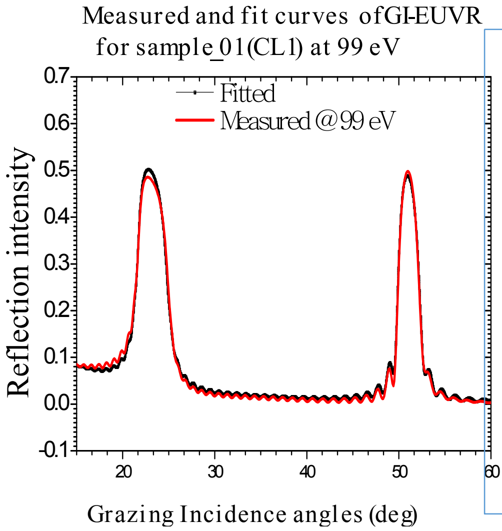

GI-EUVR thickness fit parameters (CL1):

Si layer (1), z =185 Å

int_01 (2), z =8 Å

Mo layer (3), z=27 Å

[int_02 /Si /int_03 /Mo], N =25, d=163.17Å

int_02 (4), z=10 Å

Si layer (5), z= 123 Å

int_03 (6), z =8.10 Å

Mo layer (7), z=22.05 Å

Substrate

Figure 3. 10: Measured and fit curves of GI-EUVR at 99 eV for sample_01. The table (right) contains thickness fit parameters of layers and interlayers. GI-EUVR has high tolerance to capping layer thicknesses (about 10 Å) unlike the interior layers with < 2 Å uncertainty.

Table 3.2: GI-EUVR optical fit parameters (δ and β) for sample_01 at 99 eV

Layer Medium	Optical Constant Values	Derived Interlayer
Si layer (1),	$\delta = -0.01587$ [-0.00957] $\beta = 0.00296$ [0.00181]	
Int_01 layer (2),	$\delta = 0.01374$ [0.014506] $\beta = 0.00459$	≈ $MoSi_2$
Mo layer (3)	$\delta = 0.05172$ [0.06183] $\beta = 0.004175$ [0.005087]	
[Int_02/ Si /Int_03 / Mo] × 25	d=163.17 Å	
Int_02 layer (4)	$\delta = 0.02135$ $\beta = 0.006226$	≈ Mo_3Si_5
Si layer (5),	$\delta = -0.00722$ [-0.00957] $\beta = 0.001916$ [0.00181]	
Int_03 layer (6)	$\delta = 0.02558$ $\beta = 0.002761$	≈ Mo_2Si_3
Mo layer (7)	$\delta = 0.05400$ [0.06183] $\beta = 0.004456$ [0.005087]	
	Si substrate	

[a] Data in brackets are from the CXRO database

Si layer at the capping structure (table 3.2, row 2) has shown significant change in optical constant (δ) when compared to the value contained at the CXRO database. However, Si layer in the ML structure (table 3.2, row 6) is less affected. Mo layers (high-Z element) in the capping and inside the ML structures have shown little changes in δ. The significant change in δ of Si layer at the capping structure is a manifestation of the formation of thin SiO2 layer (approximately 10 - 20 Å) due to exposure to air since a separate oxide layer was not included in the ML modeling. Thanks to the high sensitivity of Si optical properties near its EUV edge, it is possible to quantify the impact of the oxide layer on the Si optical constants that caused large deviation. The fitting algorithm to measured GI-EUVR data for sample_01 (Si-Mo capping) resulted in similar values of optical constants for the two types of interfaces. Mo-on-Si interfaces returned δ=0.02135 and Si-on-Mo interfaces yielded $\delta = 0.02558$. Phases of interlayers are approximately derived by comparing only to CXRO database and ref [98] since measured values for all possible silicide don´t exist in the literature. Accordingly, both δ values of the interlayers silicide lie somewhere between MoSi2 and Mo5Si3 [98]. Formation of different silicide compounds at the Si-on-Mo and Mo-on-Si interfaces are attributed to the difference in enthalpy and the mixing ratio of Mo and Si atoms.

Reconstructed thicknesses and optical constants of sample_02 from corresponding GI-EUVR fit are given in Fig 3.11 and table 3.3.

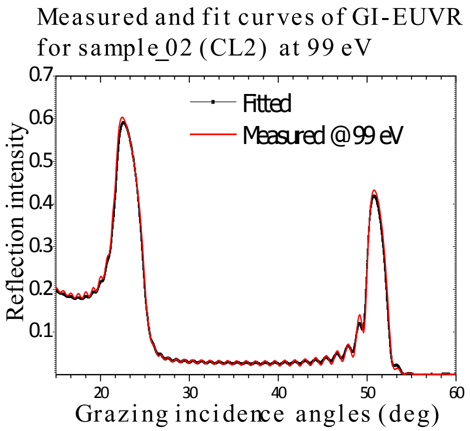

GI-EUVR thickness fit parameters (CL2):
Ir layer (1), z =21.6 Å
Mo layer (2), z =23 Å
[int_01 /Si /int_02 /Mo], N =25, d=162.68Å
int_01 (3), z=10 Å
Si layer (4), z= 123.23Å
int_02 (5), z =8.0 Å
Mo layer (6), z=23.46 Å
Substrate

Figure 3. 11: Measured and fit curves of GI-EUVR at 99 eV for sample_02. The table (right) contains thickness fit parameters of layers and interlayers. Thicknesses are determined with tolerance error of < 2Å.

Table 3.3: GI-EUVR Optical Fit Parameters (δ *and* β) for Sample_02 at 99 eV Photon Energy Optical Constants from the Numerical Fit [a]

Layer Medium	**Optical Constant Values**	**Derived Interlayer**
Ir layer (1)	$\delta = 0.08502$ [0.07931] $\beta = 0.02411$ [0.03496]	
Mo layer (2)	$\delta = 0.05245$ [0.06183] $\beta = 0.004948$ [0.005087]	
[Int_01/ Si /Int_02 / Mo] × 25,	d=162.68 Å	
Int_02 layer (3)	$\delta = 0.01482$ $\beta = 0.005704$	≈ $MoSi_2$
Si layer (4)	$\delta = -0.00577$ [-0.00957] $\beta = 0.002114$ [0.00181]	
Int_03 layer (5)	$\delta = 0.01759$	≈ $MoSi_2$

	β = 0.004044
Mo layer (6)	δ = 0.05515 [0.06183] β =0.005957 [0.005087]
Si substrate	

^{a} Data in brackets are from the CXRO database

For sample_02 (Ir-Mo capping), optical constants of both Mo-on- Si and Si- on-Mo interlayers are close to that of $MoSi_2$ [98]. Mo layers throughout the structure also show changes in the range of 10 to 15 %. The possible interface formation between Ir and Mo layers at the capping structure of sample_02 is accounted by the changes of δ's of Mo and Ir. Iridium (Ir) layer at the top of the capping structure revealed only about 7% change in optical constant (δ). This indicates superior stability and resistance of Ir to oxidation and Carbon contaminations. This fact has made Ir based coatings (e.g. Ir-Mo) to be better candidates for capping structures of MLs with better stability and performance as reported in [99]. Si layers in the ML structures of sample_02 show about 39% change in δ (table 3). This large deviation in δ of Si layers explains highest peak intensity difference between first and second order Bragg peaks in sample_02 (~0.17) while it is about i.e. ~0.10 for samples 01 and 03. This can be considered as an implicit manifestation of high sensitivity nature of Si optical properties to local atoms and interactions at its resonance edges.

In a similar fashion, results of sample_03 using same fit algorithm are summarized in Fig 3.12 and table 3.4. Interface diffusion layers with $\delta = 0.01383$ for Mo-on-Si interfaces and $\delta = 0.01037$ for the Si-on-Mo interfaces are obtained from the numerical fitting. Both δ values are closer to the optical constant of a Silicide with stoichiometric composition of $MoSi_2$.

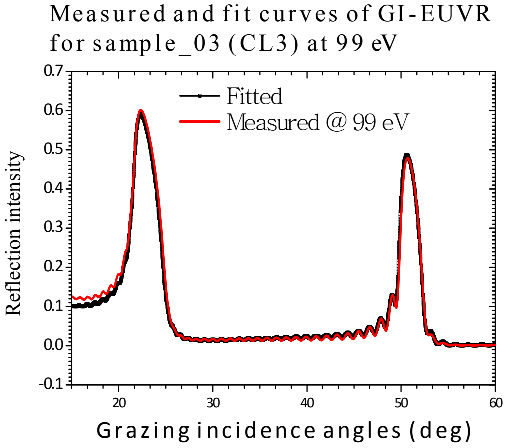

GI-EUVR thickness fit parameters (CL3):

Ir layer (1), z =21.52 Å
Int_01 (2), z =7.99Å
Si layer (3), z =134.13 Å
Int_02 (4), z =6.77 Å
Mo layer (5), z =22.40 Å
[int_03 /Si /int_04 /Mo], N =25, d=162.80Å
int_03 (6), z=6.52 Å
Si layer (7), z= 126.02 Å
int_04 (8), z =7.40 Å
Mo layer (9), z=22.81 Å
Substrate

Figure 3. 12: Measured and fit curves of GI-EUVR at 99 eV for sample_03. The table (right) contains thickness fit parameters of layers and interlayers. Thicknesses are determined with tolerance error of <2Å

Table 3.4: GI-EUVR Optical Fit Parameters (δ *and* β) for Sample_03 at 99 eV Photon Energy Optical Constants from the Numerical Fit [a]

Layer Medium	**Optical Constant Values**	**Derived Interlayer**
Ir layer (1)	$\delta = 0.08850$ [0.079315]	
Int_01 (2)	$\rho \left(\frac{\mathrm{gm}}{\mathrm{cm3}}\right) = 1.123$	
Si layer (3)	$\delta = -0.00408$ [-0.00957]	
Int_02 (4)	δ =0.009189	
Mo layer (5)	$\delta = 0.06061$ [0.06183]	
[Int_03 / Si/ Int_04 / Mo]× 25	d=162.80 Å	
Int_03 (6)	$\delta = 0.01383$	~ MoSi2
Si layer (7)	$\delta = -0.00709$ [-0.00957]	
Int_04 (8)	$\delta = 0.01037$	~ MoSi2
Mo layer (9)	$\delta = 0.05603$ [0.06183]	
	substrate	

[a] Data in brackets are from the CXRO database

For sample_03, there exist Ir-Si-Mo layers as capping structures. This increases the uncertainty in determining optical and thickness parameters of the capping structures. Thus, only results of interior ML layers are derived within reasonable accuracy. Beta (β) values are not included in Table 4 since the analysis implemented does not describe them anyway.

Based on the results presented above, GI-EUVR measurements near the resonance edge of Si atoms show great sensitivity to various parameters of the layer and interface structures. In fact, it results in different thicknesses of interlayers between Si-on-Mo and Mo-on-Si interfaces. This is consistent with the asymmetric interlayer formation reported in several publications [23, 24]. Optical constants of layers and interlayers are derived near Si EUV resonance edge. The optical constants derived slightly deviate from CXRO data base, and optical properties of interlayers demonstrate different stoichiometric compositions of silicide. The real and imaginary coefficients of the refractive indices of the interlayers correspond clearly to the Mo_xSi_y compounds formation, although the imaginary parts of the coefficient are less sensitive to the stoichiometric ratio of the elements. It is also important to note that optical constants of Si in the inner ML structures are essentially the same for all three samples, while the corresponding values for Si in the capping layer are found significantly different between samples. Ir has been used as a capping layer in samples 2 and 3. Some change in its optical constants was observed, although the difference with respect to the CXRO data is definitely less than for Si. This observation can be justified with the fact that the top-most layers exposed to the lab environment suffer from different contamination processes, involving mainly chemical reaction with carbon and oxygen. As reported elsewhere, Si when exposed to air forms an oxide layer typically of 1nm thick; Ir demonstrates a higher resistance to oxidation and better stability.

In summary, we have clearly shown that GI-EUVR at the resonance edges of low-Z elements (spacer elements) is a potent technique for diagnosing buried interfaces, layer~~s~~ analysis and characterize ML structures in combination with XRR and/or other methods. This non-imaging, non-destructive, optically sensitive and experimentally simpler technique is particularly useful for accurate interface analysis of MLs. This GI-EUVR technique may be extended to the study of interfaces helping to develop Si-based structures for micro-electronic devices.

3.4 Analysis of damage of ML optics under irradiation of low-energy ions using GI-EUVR measurements

Efforts to study the sun and the solar system have been dramatically growing over the last two decades. A number of solar missions throughout the world have been under strict preparation in order to study the sun´s atmosphere in an ever-closest distance [100]. Major ones such as the European Solar Orbiter mission aims to answer high significance scientific questions regarding the sun-heliosphere connection [101]. Solar Orbiter (SO), the first mission of the European Space Agency (ESA) Cosmic Vision 2015 - 2025 program, is expected to address how the sun creates and controls the heliosphere.

METIS, the Multi Element Telescope for Imaging and Spectroscopy, is one of the instruments selected in 2009 by ESA to be part of the payload of the SO mission. METIS adopts an innovative optical design [102] which perfectly adapts to the critical environment that will be encountered by SO, minimizing the radiation flux inside the instrument and thus the thermal problems given by the Sun proximity. Moreover, thanks to the especially suited multilayered mirrors, the instrument will perform coronal imaging in three different spectral ranges: one in the visible, and the others on two intense UV and extreme UV (EUV) coronal lines, the HI Ly-α line at 121.6 nm and the HeII Ly-α line at 30.4 nm.

However, the sun’s environment is not friendly to optical components on board. Low energy particles such as protons and α −particles from solar wind plasma, thermal loads, continuous irradiations, and natural aging processes affect the performances of optical devices in general and multilayers in particular. Thus, detail study on stability of the MLs before they make it on board indispensable.

Previous studies in [103-105] have experimentally demonstrated degradation of near normal reflectivity performances, structural damage on top layer and roughening of Si/Mo MLs after exposed to doses of protons and alpha particles. Further studies on how the radiation from the sun affects performance, optical and structural properties of the MLs is still necessary.

In this piece of work, a combination of experimental and numerical methods is implemented to perform damage analysis of MLs due to low energy ions irradiation. In addition to a physical damage observed on the top few layers, cascaded damages such as vacancies, interstitials, and atomic displacements at each layer are simulated and their impacts on EUV reflectivity are studied. Comparison of several experimental results of two MLs of same kind, one exposed to low energy ions and the other non-exposed, is expected to differentiate impact of ion irradiation on performance, optical and structural properties of MLs.

Prototype MLs were deposited at Reflective X–Ray Optics LLC (New York, USA) by DC magnetron sputtering onto polished Si (100) substrates. The MLs were design to reflect at 5° incidence angle from normal based on early requirements for METIS coronagraph [77, 85]. They are designed and optimized to simultaneously image in visible light between 450 and 650 nm, hydrogen Lyman-α line at 121.6 nm and He-II Lyman-α line at 30.4 nm [85].

Four Si/Mo ML samples with protective capping structures are studied in this paper. Two of the MLs are over coated with a pair of Si-Mo capping layers (CL1), and the other two are capped with Ir-Mo (CL2) pair. One sample from each pair is exposed to low energy helium ions (He^+) of

4 keV irradiation energy, while the other pair is kept unexposed for a reference purposes. Capping structures are summarized in Table 3.5.

The interior ML samples (excluding capping structures) consist of Si/Mo periodic structures on Si Substrate that are designed to have a period d= 16.4nm, thickness ratio Γ =0.82, $\mathrm{t_{Si}} = 13.45$nm, $\mathrm{t_{Mo}} = 2.95$nm and number of periods N=25. $\Gamma -$ ratio in this work refers to thickness-ratio of spacer layer (Si) to period of the ML.

Table 3.5: ML capping layers (CL). CL1 refers to Si/Mo and CL2 is Ir/Mo capping structures.

Capping structures	
CL1	CL2
Si (187.2 Å)	Ir (20 Å)
Mo (35 Å)	Mo (22 Å)

Two of the ML coatings (one with CL1 and another with CL2) were exposed to a flux of low energy He^{+} particles (4 keV) based on a dose fluency expected in SOLO mission environment. Alpha-particle doses are derived from data of solar irradiation at 1AU [106] with appropriate scaling to the varying distance at each point of the orbit from the sun, and finally integrated over a time of 4 years ($\approx 1.1 \times 10^{16}$ ions/cm^2) which is expected time length the SOLO satellite will stay around the sun atmosphere. Sample irradiation to He+ ions were performed at the low energy implanter facility, Institute of Ion-beam Physics and Materials Research, HZDR, Dresden (Fig 3.13).

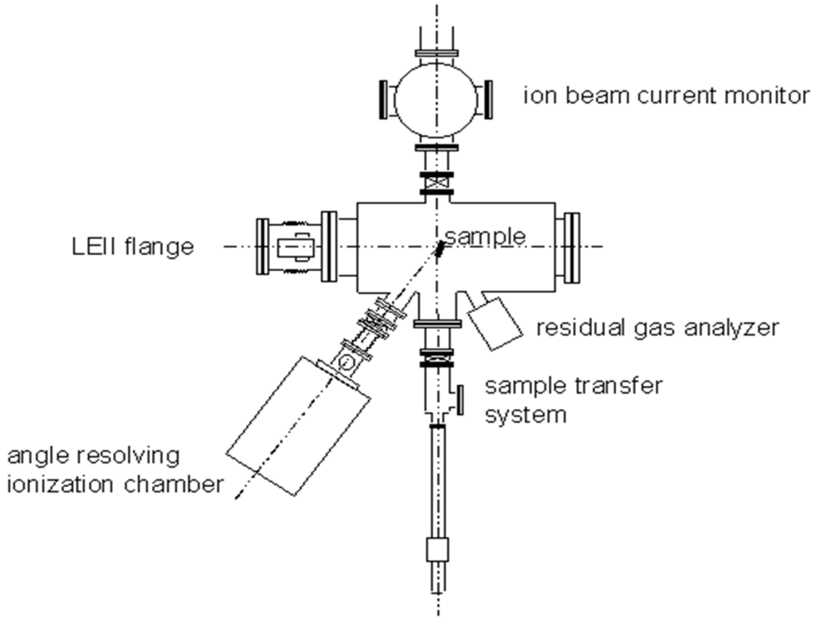

Figure 3. 13: Sketch of the Low energy ion (LEI) facility at Forschungszentrum Dresden - Rossendorf. Samples were bombarded with 1.5×10^{11} sec^{-1}cm^{-2} flux of alpha particles for about 5 hours <http://www.hzdr.de/>

Several measurements were performed to derive damage information of the exposed MLs. At-wavelength grazing incidence EUV reflectivity (GI-EUVR) measurements near the Si L- edge resonance at 99 eV were carried out at the BEAR beam line, ELETTRA Synchrotron in Trieste. On the other hand, X-ray reflectivity (XRR) measurements were done at Cu K_α line (8047 eV) with accelerated voltage and current of 40 kV and 40 mA respectively in $2\theta - \omega$ scan of the X'PERT-PRO diffractometer system [88] at the Physics department of Padova University. All the four ML samples were measured in both XRR and GI-EUVR experiments with same experimental set up and incidence beam properties.

At last, damage analysis of MLs due to irradiation of low energy He+ ions in TRIM (Transport of Ions in Medium) software were numerically performed. TRIM is a comprehensive program which calculates the stopping range of ions (up to 2 GeV/atomic mass unit) into matter using quantum mechanical treatment of ion-atom collisions (assuming a moving atom as an "ion", and all target atoms as "atoms") [107-109].

Measured data of XRR and GI-EUVR for both exposed (irr) and non-exposed (REF) MLs both with Si/Mo capping (i.e. CL1) are given in Fig 3.14. The fact that exposed and non-exposed sample pairs were deposited at same time and passed through same deposition and measurement conditions enable to systematically bypass the issue of aging and measurement errors.

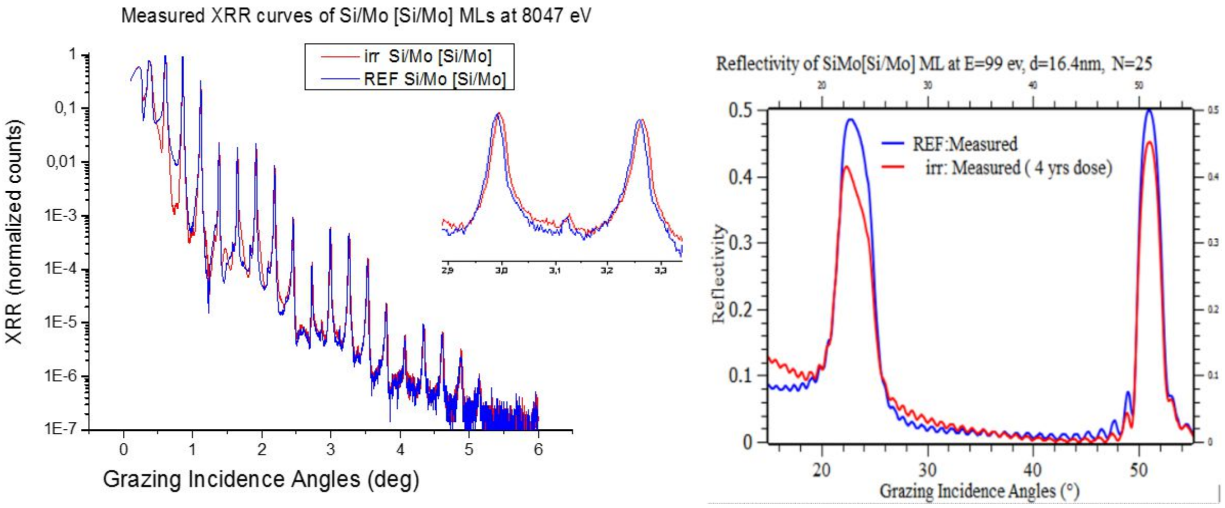

Figure 3. 14: left) Measured XRR plots of REF and irr samples both with capping structure CL1, and on the right) is GI-EUV reflectivity at 99 eV for the same samples. The onset on the left shows a slight shift of Bragg peaks of irr sample with CL1. Note that irr refers to irradiated sample and REF is the non-irradiated sample.

In a similar manner, measured XRR and GI-EUVR curves for MLs with capping structure CL2 are given in Fig 3.15.

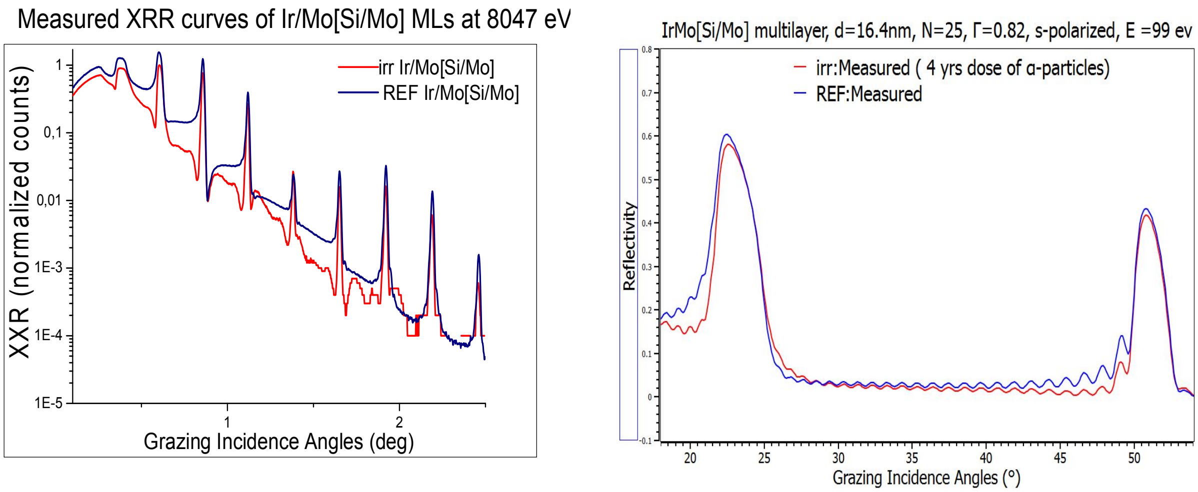

Figure 3. 15: left) Measured XRR plots of REF and irr samples both with capping structures CL2, and on the right) is GI-EUV reflectivity at 99 eV for the same ML samples also with CL2.

Fig 3.14 and Fig 3.15 confirm a slight shift of the Bragg peaks towards higher angles in both XRR and GI-EUVR measured curves. We processed the XRR data using a nonlinear least square curve fitting procedure by using the IMD [110] software using genetic algorithm (GA). Fitting Results of the XRR measured curves of the irradiated and reference samples at Cu K_α line (1.54 Å) clearly show for both samples a shrinkage of average period due to ion exposure, of about 0.3 Å and 0.1Å respectively for sample with CL1 and sample with CL2 (Table 3.6).

Table 3.6: Nonlinear curve fit results to the measured XRR curves of irr and REF samples.

	ML with CL1 (REF)	**ML with CL1 (irr)**	**ML with CL2 (REF)**	**ML with CL2 (irr)**
Period (Å)	163.370	163.073	162.617	162.497
$\Gamma -$ ratio	0.794	0.801	0.802	0.783

Inspection of Fig 3.14 and Fig 3.15 also shows a decreasing GI-EUVR performances after the irradiation of MLs with the low energy He^+ (4 keV) particles. The second order Bragg peak decreases from 0.48 to 0.40 for the sample with CL1, and from 0.6 to 0.58 for the sample with CL2. This is consistent with near normal reflectivity measurements performed at 30.4 nm and reported in [79] for the same MLs. The relative changes in reflectivity due to irradiation are different for the two samples: CL1 lose more intensity than CL2. This is attributed to the difference in protection capacity (i.e. stability) of the capping layers CL1 and CL2 [105].

We stress the fact that Bragg peaks in the GI-EUVR curves are affected differently. For example: reflectivity of second and first order Bragg peaks of the irradiated sample with CL1 (Fig 3.14 right) decreased by 12.68% and 6% from the corresponding peaks of the non-irradiated reference sample. Similar effects are observed in CL2 (Fig 3.15 right) but with less loss of reflectivity. Such discrepancies in reflectivity between the irradiated and non-irradiated samples can be attributed to the damage history of target layers (MLs) due to irradiation of 4keV He^+ ions at a dose flux of 1.5×10^{11} $sec^{-1}cm^{-2}$ for about 5 hours. A numerical damage analysis in TRIM (Fig 3.16) justifies the claim.

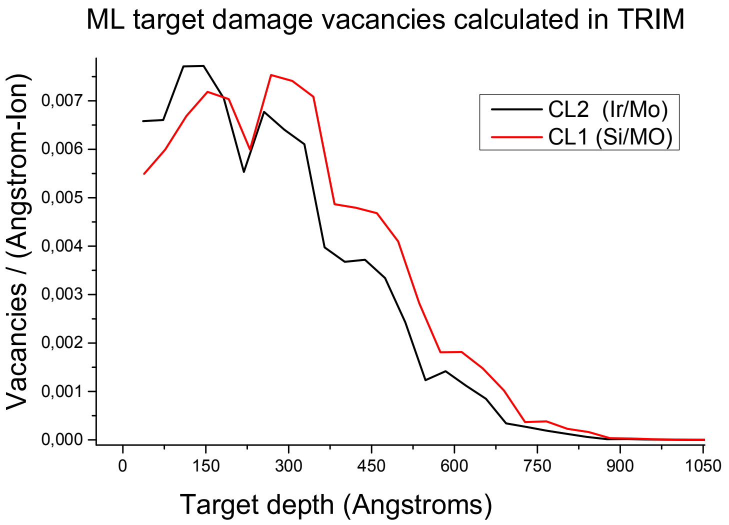

Figure 3. 16: TRIM simulations of low energy He^+ ions (4 keV) damage vacancies on both CL1 (Si/Mo capping) and CL2 (Ir/Mo capping) MLs. Simulation is performed for a total statistics of 99999 He^+ ions.

TRIM calculates ion damage events such as number of vacancies, Interstitials, and target atom displacements in the ML structure due to irradiation of energetic ions. However, thermal effects are ignored in TRIM that final damage quantities are likely changed. However, basic damage types occur and useful information can be regained.

In Fig 3.16, target vacancies refer to empty atomic sites in the ML structures due to displacements by the He^+ ions as numerically calculated in TRIM. Distribution of damage vacancies throughout the ML structures in both samples might describe the GI-EUV reflectivity pattern in Figs 3.14 and 3.15 [111]. Throughout the target depth within the reach of the 4 keV He^+ ions, ML with CL1 bears more damage vacancies than CL2 (Fig 3.16). This higher damage level of the sample with CL1 (compared to CL2 sample), mainly due to different capping structures, caused relatively greater change of reflectivity (i.e. the GI-EUVR curves) between the REF and irr samples as shown in Fig 3.14 (CL1) than that of irr and REF curves in Fig 3.15.

TRIM simulation also clearly shows the concentration of damage levels (i.e. vacancies/angstrom -ion) at the top few layers of the ML structures due to the irradiation of the low energy He^+ ions. In addition, damage levels of Si and Mo layers are different. It is then clear that at the top most structures of irradiated MLs, optical contrast ($\Delta\delta$) between Mo and Si layers is affected that in turn decreases the GI-EUVR performances. Apparently, loss of optical contrast at the upper most layers results in a higher loss of grazing incidence EUV reflectivity than near normal reflectivity.

In table 3.6, XRR nonlinear curve fitting resulted in Γ-ratios different from design value (Γ design is 0.82) for both exposed and non-exposed MLs. Note also the slight difference in Γ of the ion exposed MLs as compared to the reference samples. Such changes can be associated to the influence formation of inter-diffusion layers on the reflectivity particularly in EUV wavelengths [98, 112] due to the [113].

In summary, four Si/Mo ML samples with CL1 (Si/Mo) and CL2 (Ir/Mo) were originally prepared for a METIS coronagraph of SO mission. Analysis of impact of low energy He^+ ion irradiations of the MLs are performed. A novel GI-EUVR measurement near Si edge (99 eV) makes the analysis more innovative and sensitive. With this new method combined with the theoretical damage calculations in TRIM, we are able to confirm the degradation of reflectivity performances of MLs due to irradiations of low energy ions. It is also possible to derive, through a nonlinear curve fit of GI-EUVR measured data, the minor optical changes induced. The optical damage induced are however limited only at the top few layers that causes the 2nd order Bragg peak in Figs 3.14 and 3.15 to depreciate more than the Bragg peaks at higher angles. The stability of Ir containing capping structure is found to resist damage events better. Further work on validation with other ML samples will be paramount important.

4. COATINGS OF B4C/CEO2 MULTILAYERS FOR THE 6.X EUV LITHOGRAPHY

4.1. Introduction

Multilayer (ML) coatings are essential for technological advances and fundamental studies of EUV and X-rays. Chromium-Scandium (Cr/Sc) and alloy - ceramic oxide multilayers of $\mathrm{Ni_{80}Nb_{20}-MgO}$ are among popular candidates for soft X-ray microscopy in the "water-window" [114, 115]. Si/Mo, Si/Ir and Si/Mg multilayers have been incorporated as EUV imaging components for space mission telescopes particularly in the 17 - 30.5 nm wavelength regime [116]. Applications as polarizers, beam splitters, narrow and broadband filters in the EUV and soft X-ray are also popular in optical engineering [117]. Another eminent application of MLs in the EUV lithography as high throughput reflectors and beam shapers has gained a reputation of sustaining "Moore's Law" in the semiconductor industry, that empirically stated the doubling of transistors in a microprocessor-chip every 18 months [118]. The EUV lithography utilizes a Laser Produce Plasma (LPP) source at 13.5 nm, which enables semiconductor manufacturers to print circuit lines at or below 22 nm node. As current microlithography based on 193 nm ArF laser source is already challenged by physical and economical limits, EUVL has gained momentum as a major contender for next generation lithography by the semiconductor industry. A leading company in the EUVL development is ASML followed by many other contenders such as IBM, INTEL and others. ASML's NXE-series EUV scanners have printed 1000 wafers/day [SPIE 2015, San Jose].This approaches the industry high volume manufacturing demand, which lies about 1600 wafers/day. The output power of LPP sources, contamination and lifetime issues of collector mirrors, spatial and temporal stability of plasma pulses need to be improved to meet requirements of high volume manufacturing.

In the meantime, there is a growing interest to shorter wavelength EUV lithography platform, which is commonly known as "Beyond EUV" lithography (BEUV). The motivation behind BEUV lithography (BEUVL) at 6.x nm is to sustain “Moore’s law” and paving the way towards printing below 10 nm feature sizes on IC. For lithographic systems, wavelength (λ), numerical aperture (NA) and process constant parameter (k) determine the smallest printable feature size according to eq. (1-1). Decreasing k_1, increasing NA, and lower wavelength λ are necessary for printing fine features on Si wafer. Both k_1 and NA are, however, challenged by theoretical and engineering limits. Therefore, utilization of LPP sources at shorter wavelengths such as 6.x nm may sustain “Moore’s law’’.

Reports show the possibility of extending EUV lithography to 6.x nm from the standard 13.5 nm EUVL [119, 120] platform. Gadolinium (Gd) and Terbium (Tb) solid fuels for LPP sources producing ($\sim 1\ kW$) at the intermediate focus (IF), optical system with 40% collection efficiency, $\sim 5\%$ conversion efficiency at 2% bandwidth, multilayer reflectivity of 64% at 45° incidence angle [121] have been reported thus far [122]. However, reflectivity of $\geq 70\%$ at near normal incidence is necessary to enable the technology. The ML performance clearly shows more work needs to be done to reach minimum reflectivity requirement of >70% for the new below EUV lithography (BEUVL) platform.

In response to this demand, combination of Lanthanum (La) and Boron (B) were among the pioneer MLs deposited and tested for high performance reflectance around 6.x nm wavelengths. The first La/B ML was found to have higher diffusion and thus lower reflectivity performance that was 4.4 × less that what was expected from theoretical calculations [23]. Currently, chemical and process techniques to suppress interface diffusions are implemented and better performance is achieved with combinations of LaN/B4C and La/B4C MLs [24, 25]. However, searching for new materials that can offer better reflectivity performance at near normal incidence and beam quality or any comparable advantage in terms of process development are paramount important.

In this chapter, new ML combinations are deposited and characterized for reflectance performance at 6.x nm wavelength. This new Cerium oxide (CeO2) and Boron carbide (B4C) combination was deposited in Direct Current (DC) magnetron facility, and a number of tabletop and synchrotron based measurements were carried out to characterize it. Theoretical reflectivity calculations B4C/CeO2 MLs by taking tabulated optical constants from Henke et.al that are available at the CXRO database show comparable performance (see Fig 4.1) with the leading candidates.

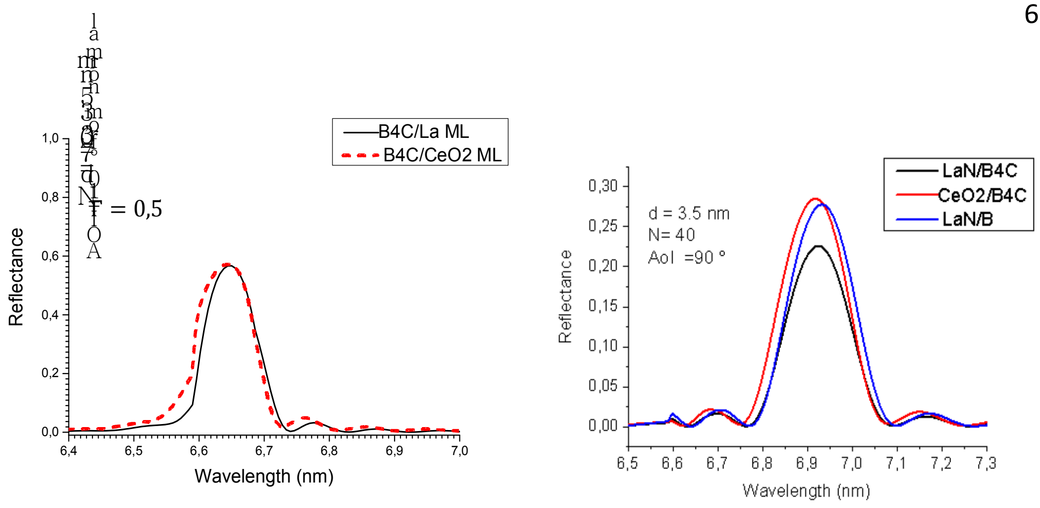

Figure 4. 1: Theoretical reflectivity performances of top candidate MLs at the 6.x nm wavelength.

A preliminary analysis of CeO2/B4C MLs for the first time deposited by DC magnetron sputtering is performed. Here, we present ML reflectivity performance at 6.x (near the boron edge) wavelength, period and layer thicknesses, optical properties of layers and interlayers.

4.2. Sample description, experiments and data analysis

Two B4C/ CeO2 ML samples (Table 4.1) were deposited in DC magnetron sputtering facility at the Institute of Precision Optical Engineering (IPOE), Tonji University from solid CeO2 and B4C precursors on Si substrate. Amorphous layers of B4C and CeO2 were grown in the low temperature deposition facility. The first sample (Sample_A) is designed for reflection performance test around 6.x nm wavelength and incidence angle of 10° from surface normal. The second sample (Sample_B) was manufactured to enable grazing incidence EUV reflectivity measurements near the Boron-edge in EUV ($\sim 186\, eV$), that is a sensitive at-wavelength metrology for the characterization of optical and structural properties of MLs with high sensitivity [123].

Table 4. 4: Design parameters of the two multilayers with the following notations: d is the period, N is number of bilayers and Γ represents the thickness ratio of the absorber layer (i.e. CeO_2 layer) to the period.

ML types	Design parameters
Sample_A: B4C/CeO2	d = 35 Å, $t_{CeO2} = 16$ Å, $t_{B4C} = 19$ Å, N = 40, $\Gamma = 0.457$
Sample_B: B4C/CeO2	d = 200 Å, $t_{CeO2} = 80$ Å , $t_{B4C} = 120$ Å, N = 10, $\Gamma = 0.400$
Substrate	Si

Measurements of at-wavelength Grazing Incidence EUV Reflectivity (GI-EUVR) were carried out at the BEAR (Bending magnet for Emission, Absorption and Reflectivity) beam line, ELETTRA Synchrotron in Trieste [124]. The stability and reproducibility of the beam energy coupled with high-accuracy control of the beam-line facility operation and measurement process allowed for noise reduction and in turn an increased reliability of data analysis. The X-ray reflectivity (XRR) measurements were performed at Cu K_α line ($\sim 8\ KeV$) in a $2\theta - \omega$ scan of the X'PERT-PRO diffractometer configuration to determine periods of the MLs with high depth resolution due to the short X-ray wavelength.

The reconstruction of ML parameters from both XRR and GI-EUVR data are performed in IMD (Modeling and Analysis of Multilayer Films) software [89]. Independent imaging evidences for the ML structures and interface profiles are provided by bright field scanning electron transmission microscopy (BF-STEM) for sample_B and High Angle Annular Dark Field (HAADF) STEM for sample_A. Both imaging experiments were performed at the Helmholtz Nano electronic Facility and Ernst Ruska-Center of the Forschungszentrum Jülich. A combination of all of the above measurements enables to characterize the MLs with high accuracy and reliability.

4.3. Results and discussion

4.3.1 Sample_A

Measured and calculated EUV reflectivity at 10° from normal for Sample_A is given in Fig-4.2.

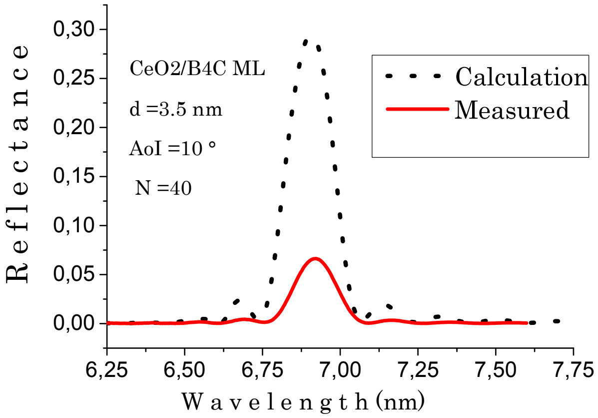

Figure 4. 2: Calculated and measured reflectivity curves for Sample_A. Tabulated values δ and β available at the Center for X-ray Optics (CXRO) database (http://henke.lbl.gov/optical_constants/) are used for the theoretical calculations. Original vales are determined by Henke and his co-authors as reported in [78].

The measured reflectivity performance at 10° from normal is 6.65 %. This is 4.4 times lower than theoretical value. High-angle annular dark field (HAADF) image of this ML sample (i.e. sample_A) confirms the presence of interface diffusion as a major cause for the low reflectivity performance as shown in Fig 4.3.

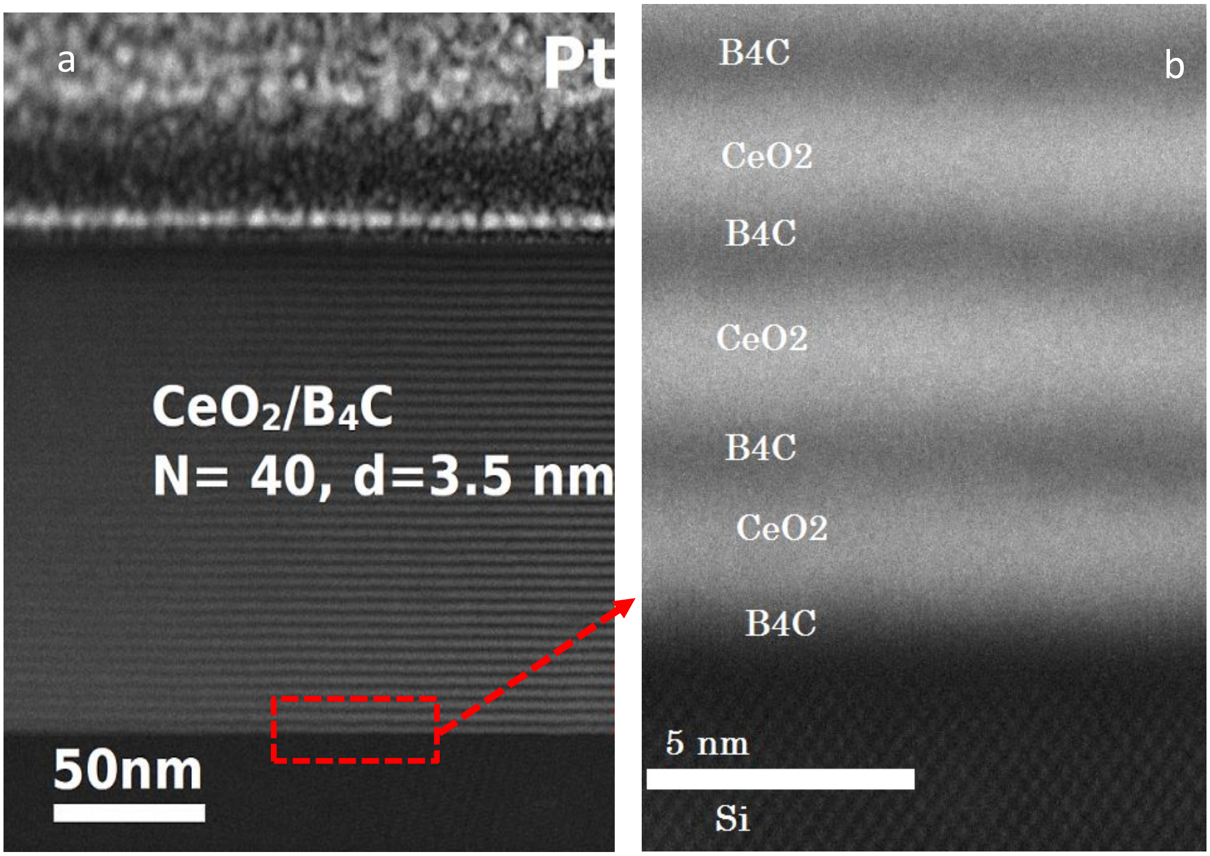

Figure 4. 3: HAADF image of sample _A, a) an overview of the ML, and b) atomic resolution of few bilayers near the Si substrate.

It is shown that Si atomic columns in the substrate are clearly resolved in the HAADF image (Fig 4.3b). A more detail view of the atomic resolution image in the [001] and [-110] axes of the Si substrate is given in Fig 4.4. The bottom onset image here shows the inter-diffusions at the interfaces.

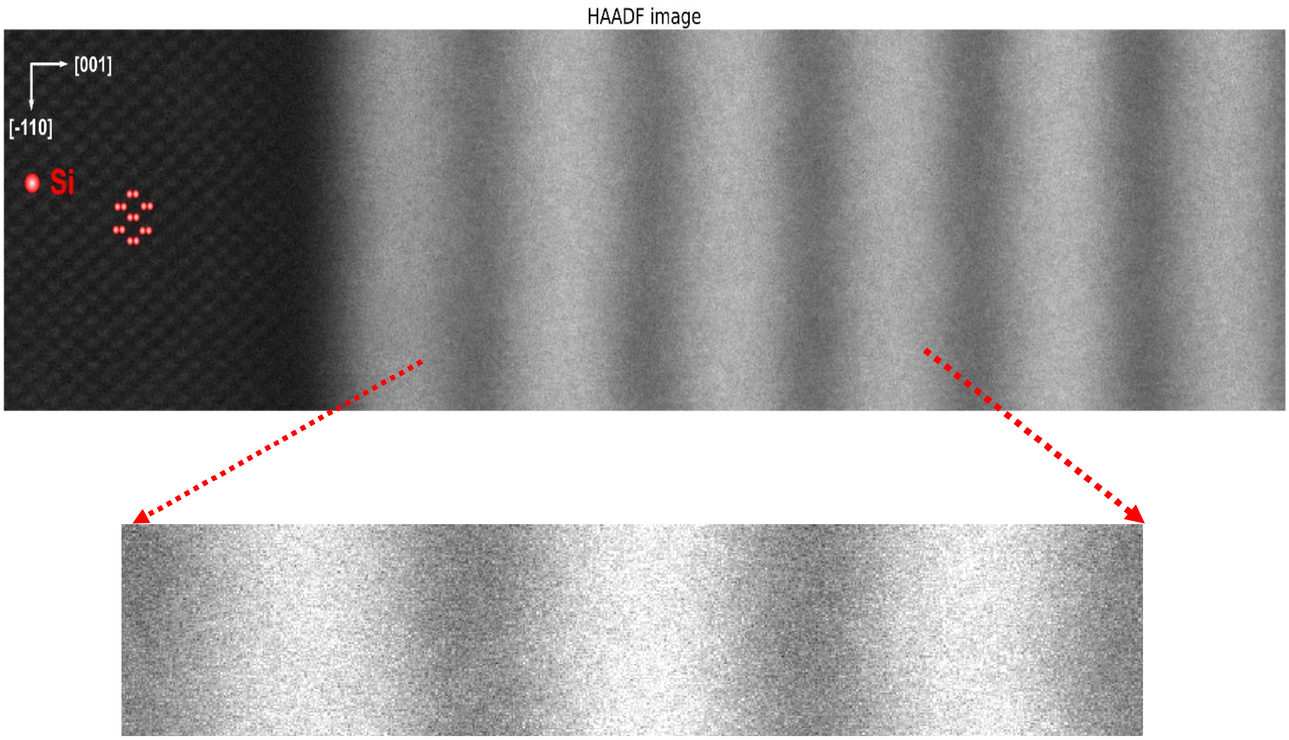

Figure 4. 4: Atomic resolution HAADF image showing Si atomic columns in the substrate. The bottom onset image (after little enhancement in contrast) clearly shows the magnitude of inter-diffusion at the interfaces.

Therefore, the HAADF image of sample_A confirms formation of inter-diffusion layers at the interfaces. Such inter-diffusion regions urged a continuous (contrary to sharp) transition of intensity profile (see Fig 4.5) in the [-110] axis of the atomic resolution HAADF image given in Fig 4.4. It is then obvious that the low reflectivity performance of the ML reported above in Fig 2 is mainly due to the interface diffusions.

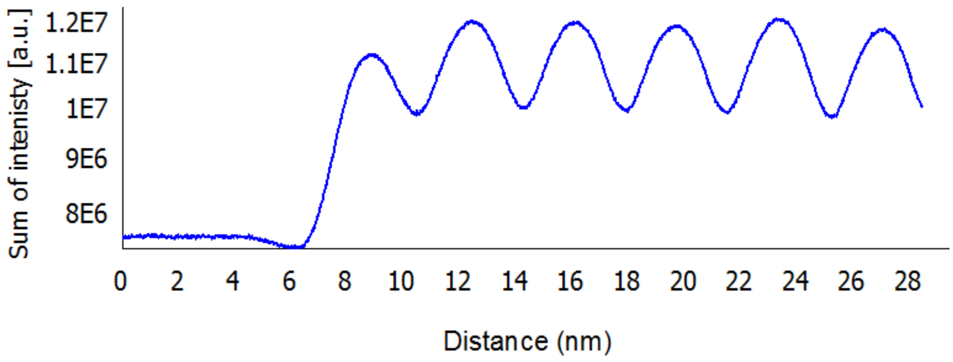

Figure 4. 5: Sum of intensity profile of the HAADF image given in Fig 4 in the [-110] axis of the Si substrate.

To investigate further density and thickness parameters of the ML, nonlinear curve fitting to the measured reflectance curve near the boron-edge (Fig 4.6) after the introduction of interlayers to account interface diffusions is performed. At the Boron edge, elemental and chemical sensitivities are higher that can reconstruct accurate values. Table 4.2 contains thicknesses and density of the ML obtained from the fitting at 10° of incidence from normal.

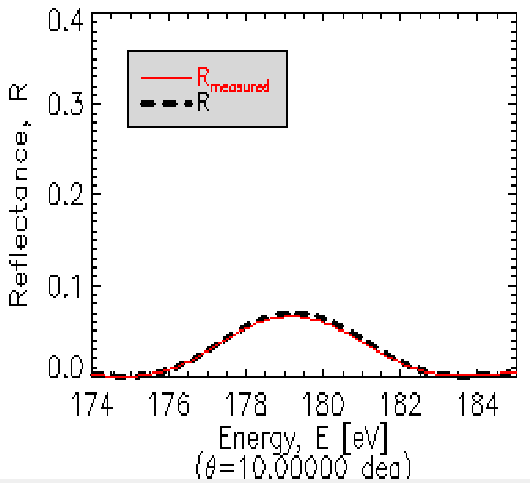

Table 4.2: ML parameters from EUVR fit for Sample_A

t_{B4C} (Å) = 10.068, $\rho\,(\frac{gm}{cm3}) = 2.537$
Interlayer_01 (Å) =7.707, $\rho\,(\frac{gm}{cm3}) = 3.875$
t_{CeO2} (Å) = 10.69, $\rho\left(\frac{gm}{cm3}\right) = 5.103$
Interlayer_02 (Å) = 7.095, $\rho\left(\frac{gm}{cm3}\right) = 4.566$
Period of ML d (Å)= 35.56

Figure 4. 6: Measured and fitted EUV reflectance for Sample_A at 10° from normal incidence. Table 4.2 at the right side shows thickness and density parameters of the ML derived from numerical fit to measured EUV reflectance.

The fact that the period of the ML obtained from the fitting (d =3.56 nm) and from the HAADF image (d=3.57 nm) in Fig 4.7 are very similar shows the accuracy of the fitting procedure.

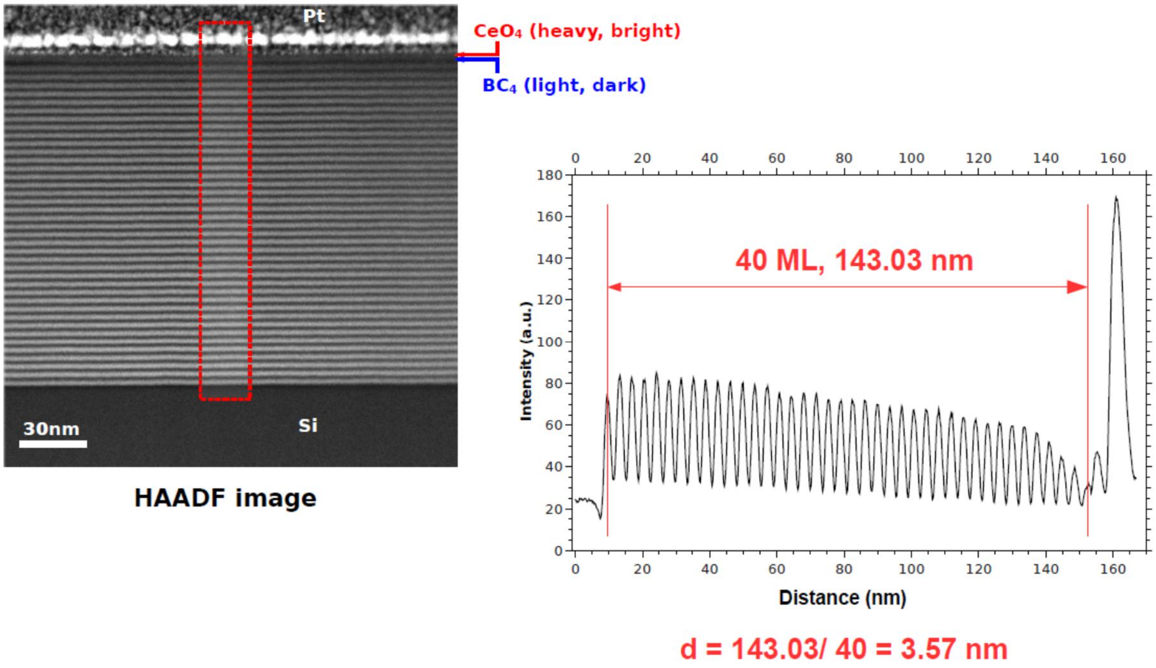

Figure 4. 7: Calculation of ML period of sample_A from the HAADF image

4.3.2 Sample_B

The above analysis for sample_A give useful insight on buried interfaces, density and thicknesses of layers and interlayers. However, further analysis is necessary to explain the physical and chemical properties of the inter-diffusion layers, CeO2 and B4C layers for EUV and soft X-ray applications. A method equally sensitive to optical properties as is to thickness is required. In fact, approximate thicknesses of layers and interlayer might be derived from the STEM images or from the intensity profiles, but that does not account the influence of optical parameters near the absorption edges of EUV wavelengths in determining the measured reflectivity curves. Due to high sensitivity of atoms to local interactions, actual measurement of optical properties is needed in EUV and soft X-rays in general and near the transition edge energies in particular.

Thus, a systematic combination of X-ray reflectivity and grazing incidence EUV reflectivity (GI-EUVR) measurements near absorption edge are performed to derive optical, structural and morphological properties of the inter-diffusion regions, CeO2 and B4C layers. The XRR analysis allows determination of ML period with reasonable accuracy because of its high in-depth resolution at Cu-K_α wavelength (~1.5 Å) and high sensitivity to Bragg peaks. The at-wavelength GI-EUVR enables derivation of optical constants with high sensitivity, and accounts possible tradeoff between thickness and optical parameters in the wide grazing angle measurement setup as explained in ref [123].

Here, a grazing incidence at-wavelength reflectivity analysis near EUV absorption edge of the low-Z element (i.e. Boron) is performed for sample_B. The sample was fabricated from same materials and in similar deposition conditions (gas pressure, substrate temperature and ultra-high vacuum properties) as that of sample_A. Thus, interface profiles, optical constants of layers and interlayers derived from sample_B are representative of sample_A. As mentioned above, a four-layer ML structure (B4C layer + interlayer 01 + CeO2 layer + interlayer 02) model that accounts the interface diffusions evidenced from the BF-STEM image of sample_B (Fig 4.8) is implemented during the GI-EUVR data analysis. Interlayer 01 (int_01 in short) and interlayer 02 (int_02) represent the diffusion layers of B4C - on - CeO2 and CeO2 - on - B4C respectively.

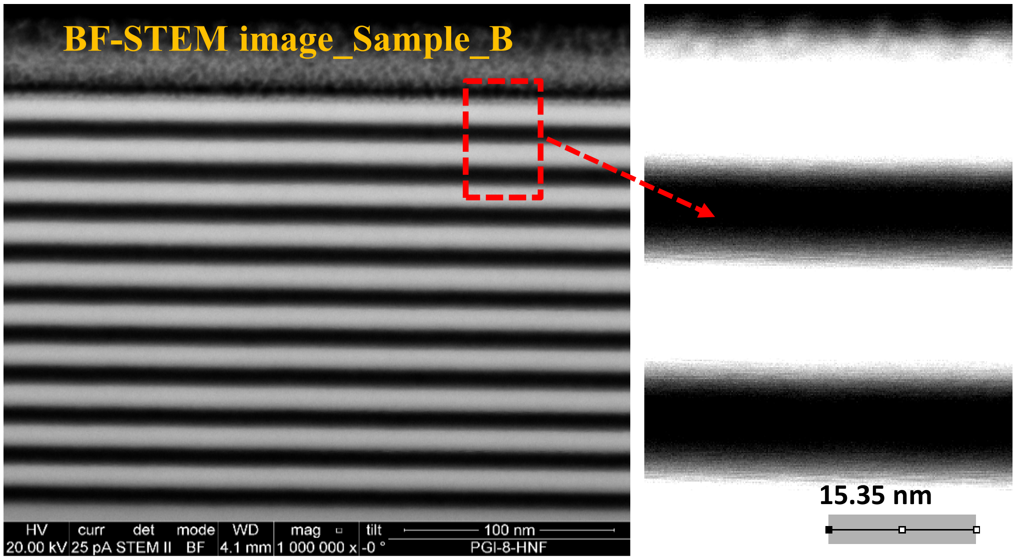

Figure 4. 8: Bright field - scanning transmission electron Microscopy (BF-STEM) image of Sample_B. Interface diffusion is clearly visible on the onset image. Int_01 refers to B4C – on - CeO2 interfacial diffusion and Int_02 is vice versa.

Analysis of the XRR data at the Cu K_α line for sample_B (Fig 4.9a) returns period $d = 199.4 \pm 0.11$ Å. GI-EUVR data fit of this sample at 182.92 eV by taking the ML period as obtained from the XRR analysis is shown in Fig 4.9b. Such GI-EUVR analysis of sample_B is performed for EUV photon energies from 177.53 eV – 183.82 eV (slightly below the B-edge). The short range of photon energies is chosen to test the reliability of the analysis method implemented here and then measurements over larger ranges of EUV energies (both above and below the B-edge) will be included in our next work plan.

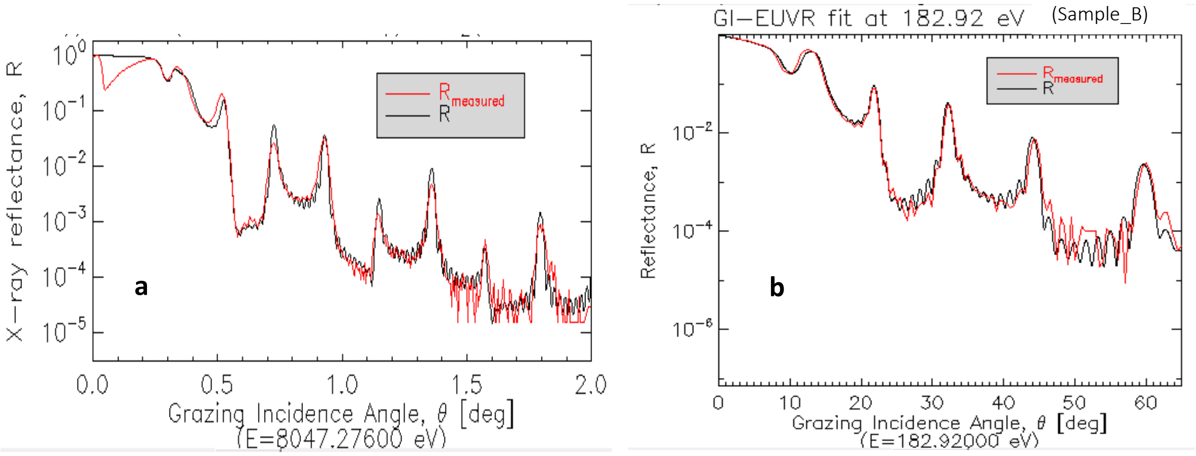

Figure 4. 9: a) Nonlinear curve fit to the X-ray data at the Cu K_α line for sample_B, b) Nonlinear curve fit to the GI-EUVR data at 182.92 eV of sample_B.

Optical constants (δ and β), layer and interlayer thicknesses derived from the fittings of GI-EUVR data, within the confidence intervals in IMD, of sample_B for different photon energies are summarized in Table II. Note that ML period derived from the XRR analysis is fixed during the GI-EUVR analysis.

Table 4.3: Sample data within the confidence intervals of sample_B calculated from combined analysis of XRR and GI-EUVR measured data. In brackets are derived thicknesses from the GI-EUVR analysis, keeping period of the ML fixed as obtained from XRR.

Photon energy (eV)	B4C_layer (98.1Å)		Int- 01_layer (18.5Å)		CeO2_layer (56.9Å)		Int 02_layer (25.98Å)	
	δ	β	*δ*	β	*δ*	β	*δ*	β
177.53	0.005711	0.00111	0.012503	0.002097	0.023407	0.003163	0.022739	0.005449
178.42	0.005294	0.001096	0.012242	0.002560	0.023487	0.003177	0.022682	0.004731
179.32	0.004594	0.001075	0.01320	0.0029633	0.023478	0.003090	0.02190	0.005645
180.22	0.004465	0.00103	0.011591	0.002784	0.023255	0.003387	0.022741	0.0049137
181.12	0.004614	0.00109	0.011854	0.002030	0.022300	0.003008	0.021484	0.005330
182.02	0.003631	0.00103	0.012025	0.002210	0.021832	0.002780	0.021526	0.005850
182.92	0.004078	0.0012182	0.013590	0.001650	0.021211	0.00182	0.019411	0.006110
183.82	0.002703	0.0009512	0.013572	0.005313	0.024804	0.00312	0.022615	0.004774

For clarity, comparisons with values of *δ* and β determined by Henke and available at the CXRO database are given in Fig 4.10a and Fig 4.10b for B4C and CeO2 layers respectively. Measured optical constants clearly demonstrate a strong nonlinear pattern near the absorption edge of Boron, unlike the linear behavior of the tabulated values from CXRO database. The optical constants of B4C layers obtained are also fully consistent with the magnetron sputtered B4C thin films measured by R. Soufli et.al [125] and G. Monaco et.al [126].

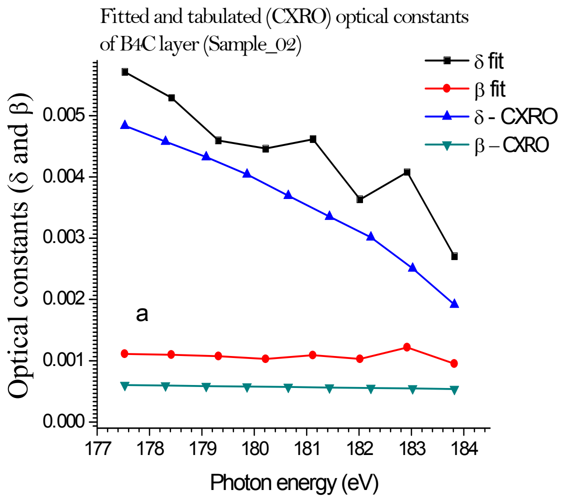

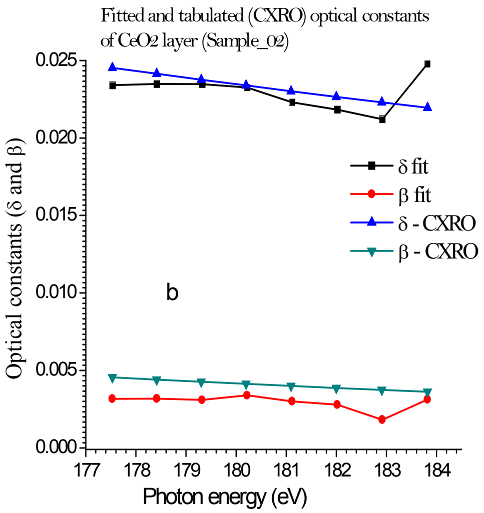

Figure 4. 10: Optical constants (δ and β) retrieved from the GI-EUVR data fittings and tabulated values from CXRO database. a) B4C layer and b) CeO2 layer. Note that optical constants of B4C and CeO2 are also representative of sample_A.

The change of optical constants of layers in sample_B as a function of photon energy, as derived from GI-EUVR data analysis, is plotted in Fig 4.11. As expected, the optical constants (δ) of int_01 and int_02 shown Fig 9a are bound by that of B4C from below and CeO2 from above. The fact that δ values of int_02 (CeO2 – on – B4C inter-diffusion region) lies far from top and bottom boundaries shows dominance of B4C atoms, while int_01 (B4C – on – CeO2 region) seems to be dominated by CeO2 atoms. EUV and soft X-ray reflection curves, particularly near the resonance edges, are more critical on δ contrast ($\Delta\delta$) of layers, which makes the accuracy of β values in Fig 4.11b less accurate and difficult to withdraw any conclusion from it.

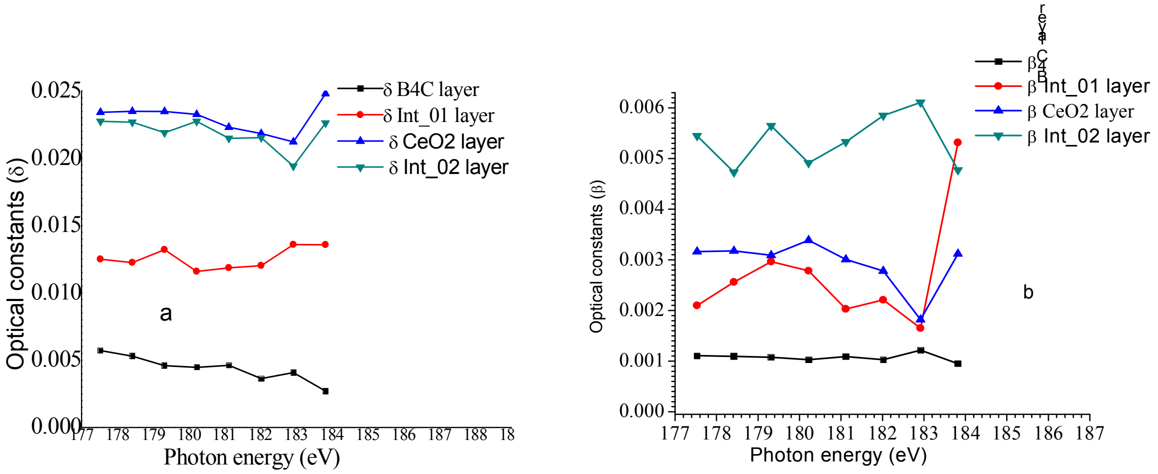

Figure 4. 11: Graphical summary of calculated optical constants from the XRR and GI-EUVR measured data for sample_B. Note that optical constants of B4C and CeO2 are also representative of sample_A.

Finally, ideal reflectivity performance of sample_A at incident photon energy E = 183.82 eV is calculated as given in Fig 4.12 by using the new optical constants of B4C and CeO2 from table II. Period and thickness ratio of sample_A are slightly modified to $d = 34.80\ \text{Å}, \Gamma = 0.43$ in optimizing the reflectivity because of new optical constants used for calculation.

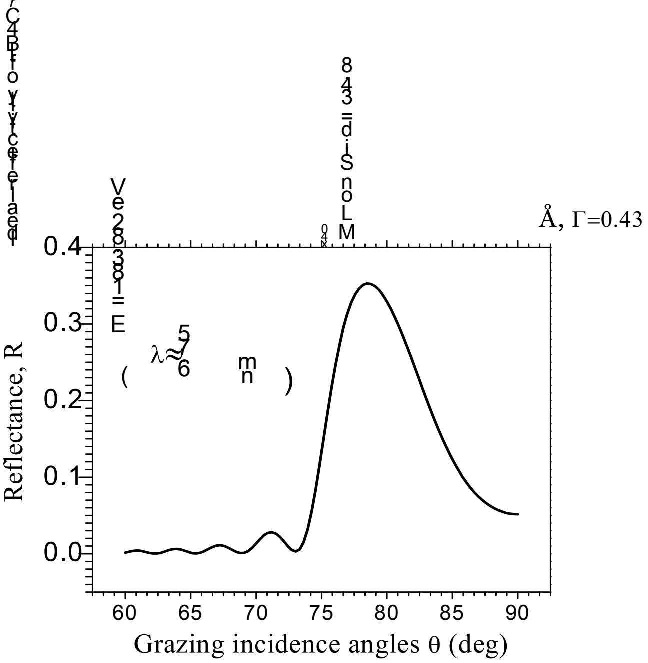

Figure 4. 12: Ideal reflectivity performance of B4C/CeO2 ML on Si substrate with N =40, d= 34.8 Å, Γ=0.43

Reflectivity of 35.3% is achieved for an incidence angle of 10° from surface normal. This performance level is significantly higher than the theoretical reflectivity calculated from tabulated optical constants by Henke, et.al as shown in Fig 4.2. This demonstrates that values provided in the available databases may be quite inaccurate for designing new optical coatings. The method of measurements described above can provide a way for improving the much-needed knowledge of the optical properties of materials used for advancing the nano-technology.

4.4 Summary

Multilayers of B4C/CeO2 for below 10 nm EUV applications were fabricated for the first time in DC magnetron sputtering facility. Reflectivity performance of the ML (sample_A) at 6.9 nm wavelength and 10° incidence angle from surface normal is 4.4 times less than the theoretical simulation. Even if this performance is comparable to the leading candidate ML (i.e. La/B) for 6.x nm EUVL with same design parameter [23], the performance is still low when compared to the optical and physical properties of B4C and CeO2 materials individually. Therefore, we performed several experimental measurements to understand the ML structure and gaining feedback for future deposition optimization. GI-EUV reflectivity, X-ray reflection at Cu-K_α, HAADF, BF- STEM imaging and other relevant measurements were performed to carry out accurate analysis of the MLs.

Accordingly, major cause for the low reflectivity performance of the B4C/CeO2 ML is found to be high inter-diffusion between layers as shown in Fig 3 and Fig 4. For convenience of the GI-EUVR analysis, sample_B (with thicker period and thus several EUV Bragg peaks) was selected for the derivation of optical constants of inter-diffusion layers. Asymmetric inter-diffusion layers are found to be formed in a magnetron deposited B4C/CeO2 MLs with CeO2 - on - B4C thicker than B4C - on - CeO2 (25.98Å vs 18.5Å).

Optical constants of layers and interlayers for short range of photon energies (177.53 - 183.82 eV) near the Boron edge are derived. The δ and β of B4C are consistent with previously reported measurements by R. Soufli et.al [125] and G. Monaco et.al.[126]. It is also worth mentioning that optical constants of CeO2 layers in the EUV energy range of 177.53 eV – 183.82 eV are for the first time measured here. Comparison of optical constants of B4C and CeO2 layers with corresponding tabulated values in CXRO database (originally determined by Henke. et al) show abrupt variation of the currently measured optical constants unlike the linear behavior in the tabulated ones. This is likely due to the higher sensitivity of near edge EUV optical constants to influences of fine structure.

Lastly, ideal reflectivity performance of the B4C/CeO2 combination based on optical constants derived using the current analysis is found to be significantly higher than what was calculated theoretically from the tabulated values. This demonstrates that values provided in the available databases may be quite inaccurate for designing new optical coatings. The future work on this particular multilayer coatings focus on the incorporation of thin film barrier layers and/or performing the deposition in a reactive magnetron facility to control the mass flow of Oxygen in the case of CeO2. Besides, adopting better deposition practices of B4C from the literature might help to optimize the interface profile.

5. TABLE TOP GRAZING INCIDENCE EUV SCATTERING EXPERIMENT (ONGOING)

5.1 Design and characteristics of the experiment

Grazing incidence light scattering experiment at 13.5 nm EUV wavelength is being developed at the Physics Department of RWTH Aachen University for Inspection of periodic, quasiperiodic, nanostructured and interface profiles of layered structures. It is designed to meet the increasing demands of at-wavelength characterization of EUV optical components. The short wavelength at around 13.5 enables propagation of more diffraction orders compared to longer wavelength radiation. It increases sensitivity of the method to small structure features [38]. The set-up is similar to the powerful GISAX (Grazing Incidence Small-Angle X-ray reflection) experiment in X-rays. As further optimizations are undergoing, final performance of the experiment is not given here. However, description of the experimental set-up, preliminary results of diffuse optical scattering from multilayer mirrors and techniques to calibrate the angular distributions of the scattered signals are provided here in this chapter.

Grazing incidence EUV scattering (GI-EUVS) can be a powerful technique for surface and buried interfaces by tailoring the incidence angle to reach out buried interfaces. It also increases the observable sample area proportional to $\sim {}^{1}/_{\sin\theta_i}$ related to the footprint at low grazing incidence. Certainly being at short wavelength in EUV enables high spatial frequency resolution of surface roughness and nano-patterns. A schematic of the GI-EUVS experiment capable of measuring angle resolved scattering in a plane is shown in Fig 5.1.

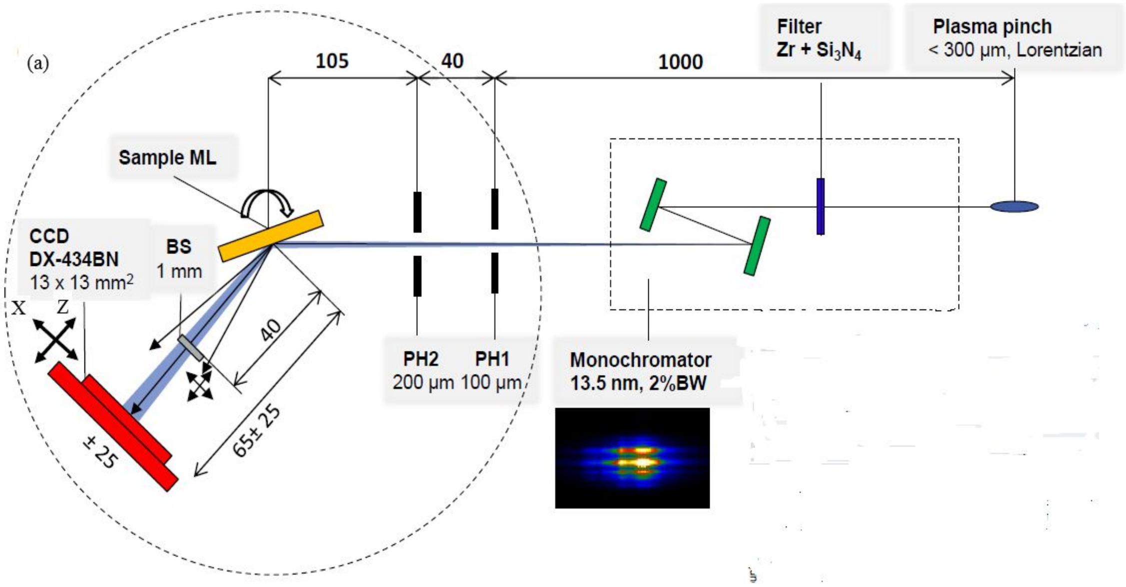

Figure 5.1: Schematic of the grazing incidence EUV scatterometer at the physics department of RWTH Aachen University (Model taken from Aleksey Maryasov). CCD is limited to 2D motion in X and Z directions, sample holder can move in the X-direction and in-plane rotation to change the incidence angle. Note that the CCD Is placed 10° inclined towards the Z-axis for alignment reasons. Every calculation considers the CCD inclination.

5.1.1 Samples

Grating, quasi-periodic structures, thin film coatings and multilayers are planned to be measured in this experimental demo. Nevertheless, two ML mirrors that were characterized in detail in chapter four are measured for the preliminary analysis of EUV scattering. Design parameters of the ML samples are given in table 5-1.

Table 5.1: Design parameters of the two ML mirrors measured for EUV diffuse reflection (scattering)

ML types	Design parameters	
Sample_A: B4C/CeO2	d = 35 Å, $t_{CeO2} = 16$ Å, $t_{B4C} = 19$ Å, N = 40, $\Gamma = 0.457$	
Sample_B: B4C/CeO2	d = 200 Å, $t_{CeO2} = 80$ Å , $t_{B4C} = 120$ Å, N = 10, $\Gamma = 0.40$	
Substrate	Si	

The tabletop EUV scattering, as any other similar purpose experiment, contains three main parts. The source, beam preparation (conditioning section) and experimental chamber. A picture of the set-up is given in Fig 5.2.

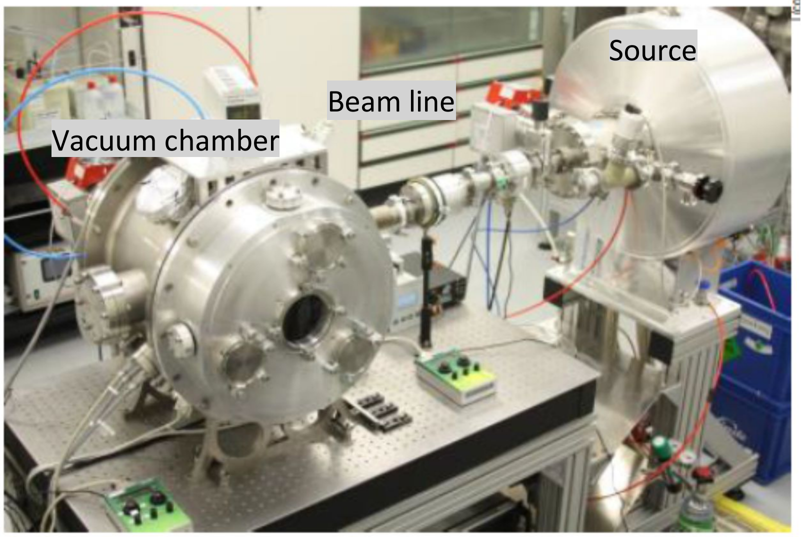

Figure 5.2: A picture of the EUV scattering set-up

5.1.2 The light source

The EUV spectra needed in this experiment are produced through a discharge produced plasma (DPP) of Xenon (Xe) gas due to its strong emission around 13.5 nm [127]. The EUV emission spectra of Xe is given in Fig 5.3. DPP produce the Xe plasma through a pulsed discharge of electrically stored energy; the hot and dense plasma is generated here by means of pinching magnetic compression of the discharge plasma. The source emits high brightness and high frequency (up to 1 kHz) EUV spectra with in-band radiation energy ~4 mJ per pulse/sr/2% bw.

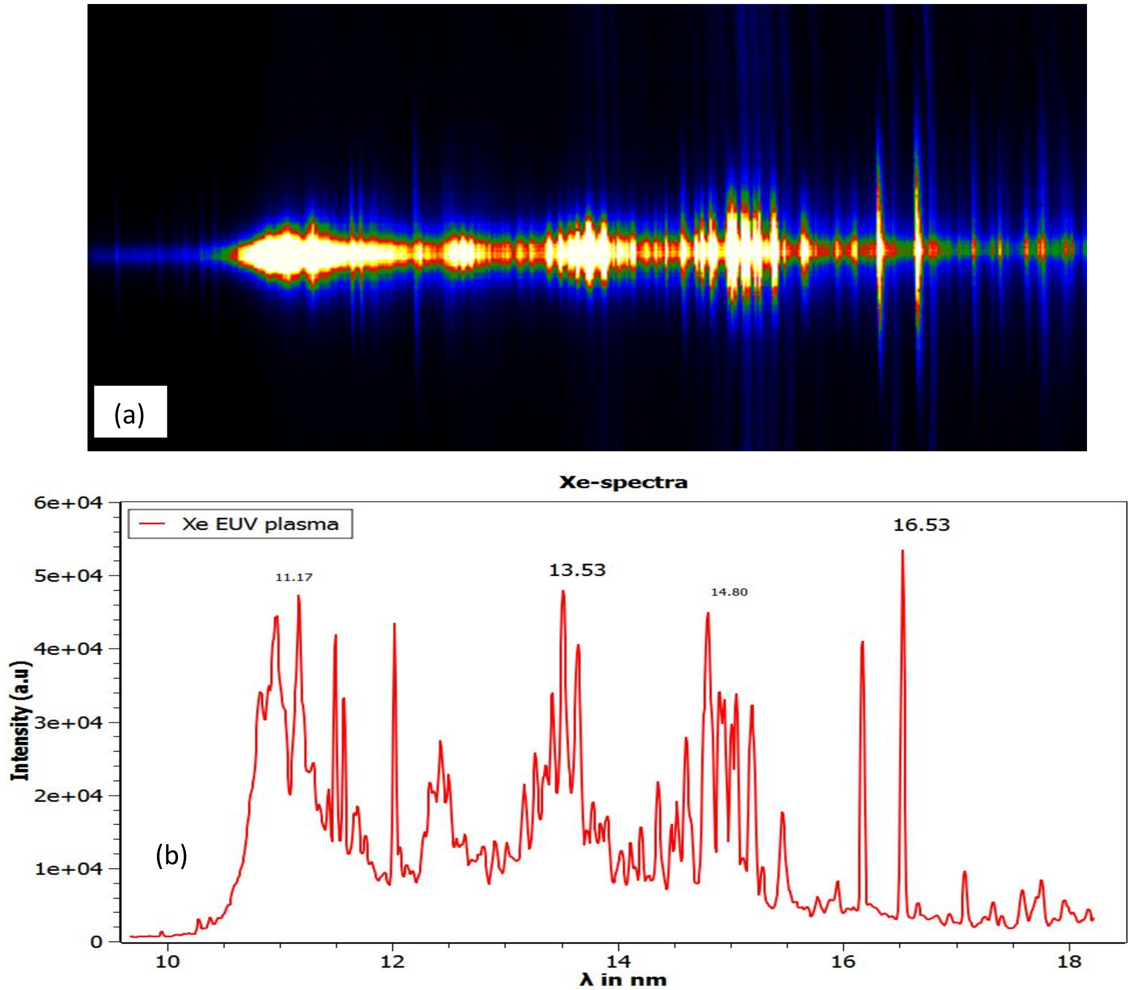

Figure 5.3: Xenon gas (Xe) EUV emission spectra (a) spectrograph including a flat-field grating and a charge-coupled device detector; (b) Wavelength calibrated emission spectra

5.1.3 The beam line

This part is also known by the name beam conditioning. It contains combinations of Zr and Si_3N_4 filters of 0.2 µm thicknesses, which suppress radiation at $\lambda > 20$ nm. Multilayer mirror (Si/Mo) based monochromatic to narrow the bandwidth to 2% around the center wavelength of 13.5 nm is inserted. It also contains a pinhole of size 50 -200 µm to further limit the spot size (beam divergence) entering the experimental chamber.

5.1.4 The experimental chamber

The experimental chamber is where vacuum compatible high-energy detection CCD camera, piezo stages, sample holders, pinholes and the sample holder are found (see Fig 5.4).

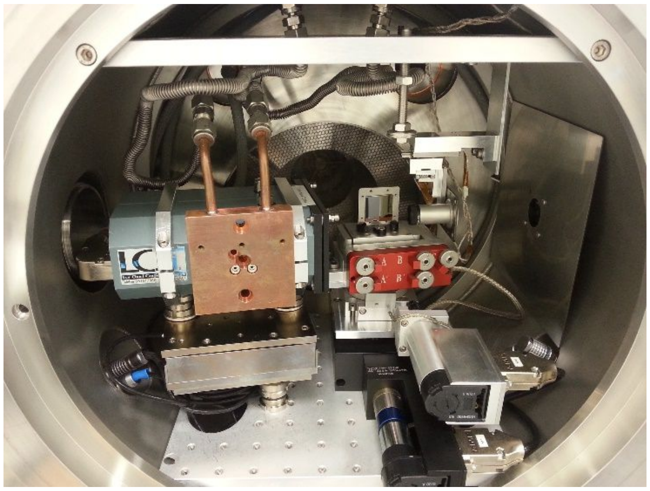

Fig 5.4: Inside view of the experimental chamber

This set-up can handle only for grazing incidences of $2-10°$ due to limitation of vacuum chamber size and limited motion of the camera piezo stage in X-direction (due to small chamber size as well). However, this range of grazing incidence angles satisfies well to the need of small angle EUV scattering measurements. The detection camera can only make $\pm$ 40 mm linear motion in the X-direction (Fig 5.1). This linear motion equates to detection angles in the range of 2-50°. However, in practice scattering detection while moving the camera causes several overlaps and complicates the results. Therefore, scattering measurements are taken while the camera is fixed. It is more or less a rocking scan measurement where the CCD is fixed and sample is rotated. A 13 mm by 13 mm CCD camera (DX-434 BN) of each pixel size 13 μm translates to maximum detection angle of about $\theta_s \sim 11°$. The angular resolution of detection is limited by the CCD pixel number (1024×1024) and size. The set-up can only measure scattering signals with a fixed angular resolution of 0.2 $mrad.$ A summary of the experimental parameters and corresponding values are given in Table 5-2.

Table 5-2: Characteristic values for main parameters in the EUV scattering set-up

Parameter	**Value**
Wavelength (nm)	13.5 , 2% b.w.
Grazing illumination angle (deg)	2 -10
Detection angular range (deg)	2 -11
CCD angular resolution (mrad)	0.2
Horizontal and vertical beam divergence (mrad)	~1.6
Maximum in-band radiation energy (per pulse/sr/2% bw	4 mJ
Beam divergence (mrad)	~4.0

5.2 Direct spot and diffuse reflection measurements

First measurements are dedicated to direct and diffuse reflection spots in order to differentiate scattering effects of the beamline (e.g. from the inside structures of pinhole) and the ML sample. As shown in Fig 5.5a and Fig 5.5c, the scattering effect of the beamline increases visibility with increasing exposure time. Diffuse scattering (diffuse reflection) from the ML sample in different exposure times are shown in Fig 5.5b and 5.5d. Slight scatterings from the beam line are visible while the ML sample shows enhanced scattering. For a scattering at about 13.5 nm wavelength, many of the surfaces in the beamline can cause significant scattering. Such inherent problems can be measured in the direct spots and are considered as signature of the instrument.

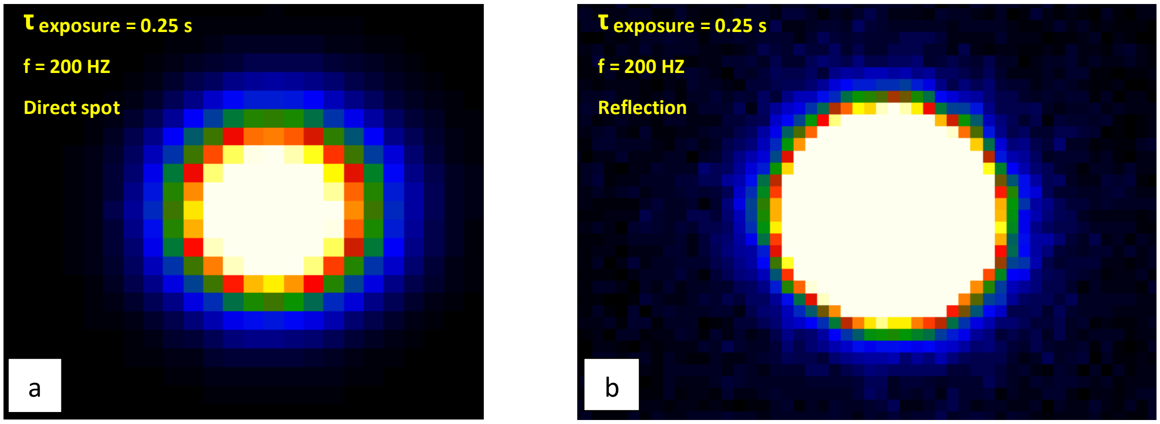

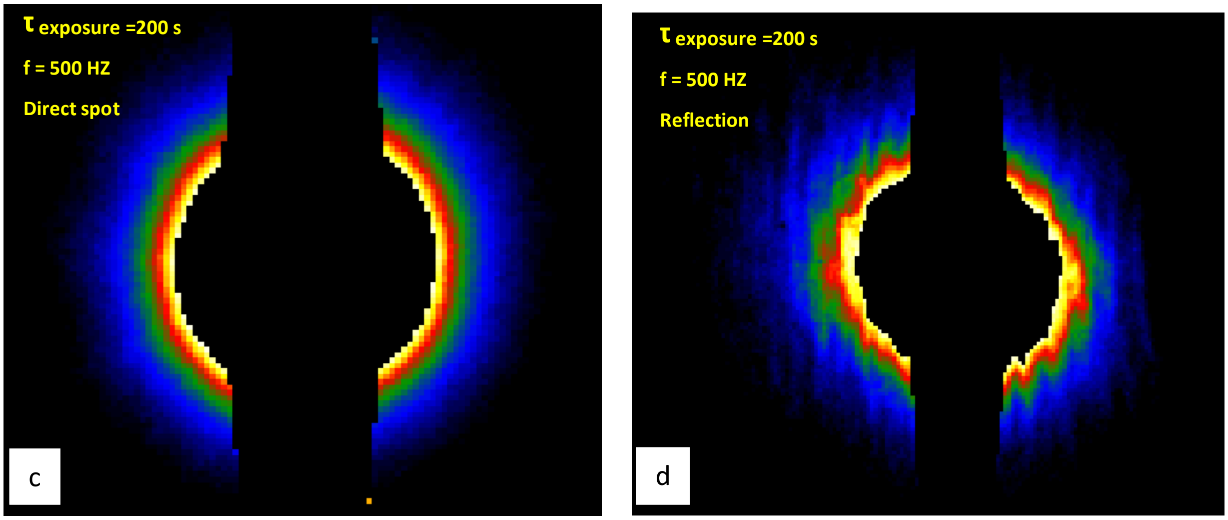

Figure 5.5: Direct spot and ML mirror diffuse scattering (sample_B) at 13.5 nm EUV wavelength and grazing incidence angle of 9° captured in CCD camera. The center halos in c) and d) are saturated region due to long exposure time (i.e. 200 s).

For exposure times beyond 1.0 sec, saturation is evident which limits the sensitivity of the measurement to the scattered signals especially from fine features. Therefore, a 1.0 mm beam-stop is introduced between the sample and CCD to block the specular beam and then increase sensitivity of scattered signals by increasing the integration time of the measurement since the powerful specular beam can be blocked before saturation is reached. Fig 5.6 shows the direct spots and ML mirror diffuse scattering in the presence of 1.0 mm beam-stop. However, the roughness at the rims of the beam-stop can introduce additional scattering that need to be differentiated from the sample scatter.

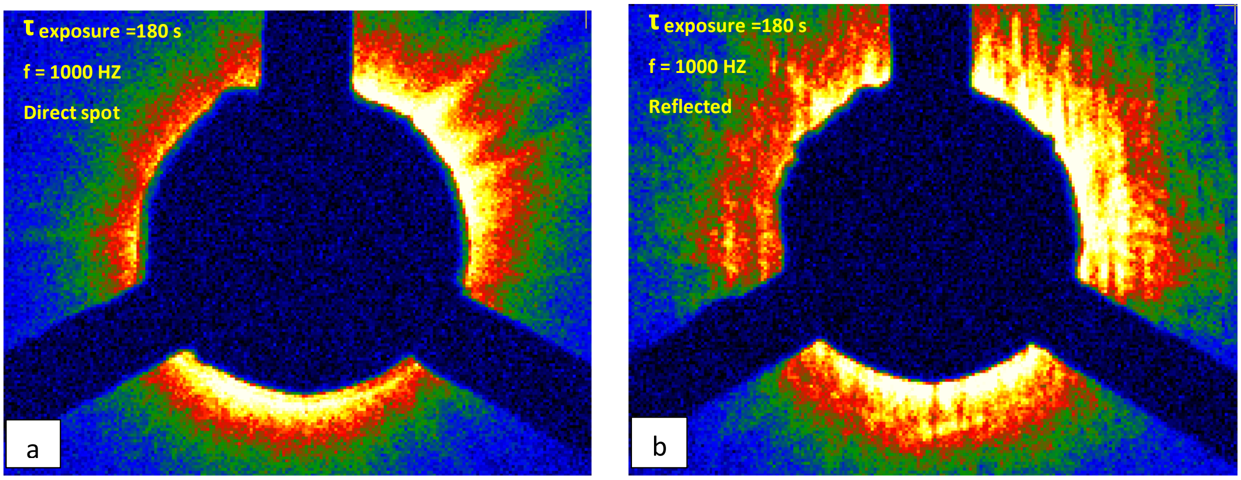

Figure 5.6: Direct spot and diffuse reflection from ML sample_A in the presence of 1mm beam-stop, integration time =180 sec and source frequency = 1000 HZ. The reflection measurement is performed at grazing incidence angle of 9°.

Clearly, the beam-stop introduced greater scattering from its edges than the rest of the beamline as can be seen from the difference in scatter pattern in Fig 5.5c and Fig 5.6a. The enhanced and quasi-periodic scattering patterns shown in Fig 5.5d and Fig 5.6b are, however, from the ML mirrors under investigation. A similar diffuse reflection measurement from the ML sample_A with higher source frequency and exposure time is given in Fig 5-7. The quasi-periodic structures have approximately 258.0 μm, which translates to a spatial roughness frequency $f =$ 0.00387 μm^{-1} (MSFR). For a relatively high beam divergence (~4.0 mrad) due to its simplicity in design, resolving the MSFR is a success.

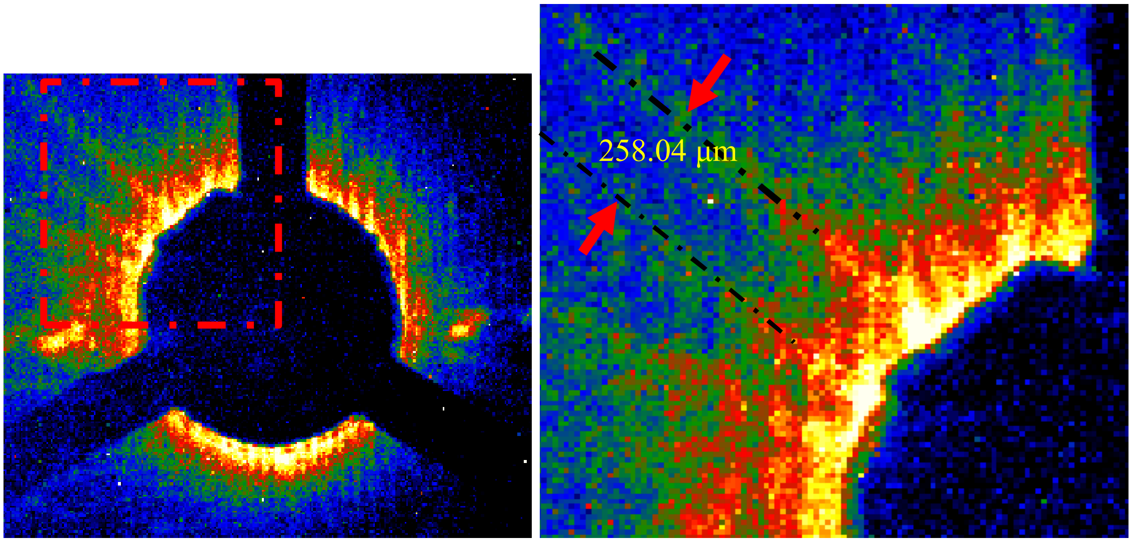

Figure 5.7: Diffuse reflection from the ML sample_A with $t_{\text{exposure}} =$ 10 min, $\theta_i = 8.9°$ and EUV source repetition rate of 1000 HZ. A beamstop of 1.0 mm is used to block majority of the specular beam. The three dark sheets extending in three directions are connectors of the beamstop.

To support ARS analysis of ML mirrors in the current experiment, calibration of the direct spot and diffuse reflection is required. Among others solid angle ($\Delta\Omega_s$), CCD pixel-sample distance and CCD angular distribution of the scattering need to be calculated. The subsequent section then describes the calibration process of ARS measurements for the current experimental set-up.

5.3 Angle resolved scattering (ARS): Calibration and analysis

Calibration of ARS measurements here refer to the quantification of angular distribution of direct spots and/or diffuse reflections captured on the plane CCD image area. Calibration of ARS of a new sample is performed either by measuring the incident power and the detector solid angle directly, or by comparison to scattering signals from a standard sample of known (certified) diffuse scattering properties [128, 129]. Unfortunately, availability of such standards for 13.5 nm EUV wavelengths is very limited. Thus, the former technique is favored and discussed here. The relative simplification of the GI-EUVS set-up (Fig 5.1), compared to goniometric-systems , allows calibration of angle resolved scattering based on geometric ray tracing as described in Fig 5.8a.

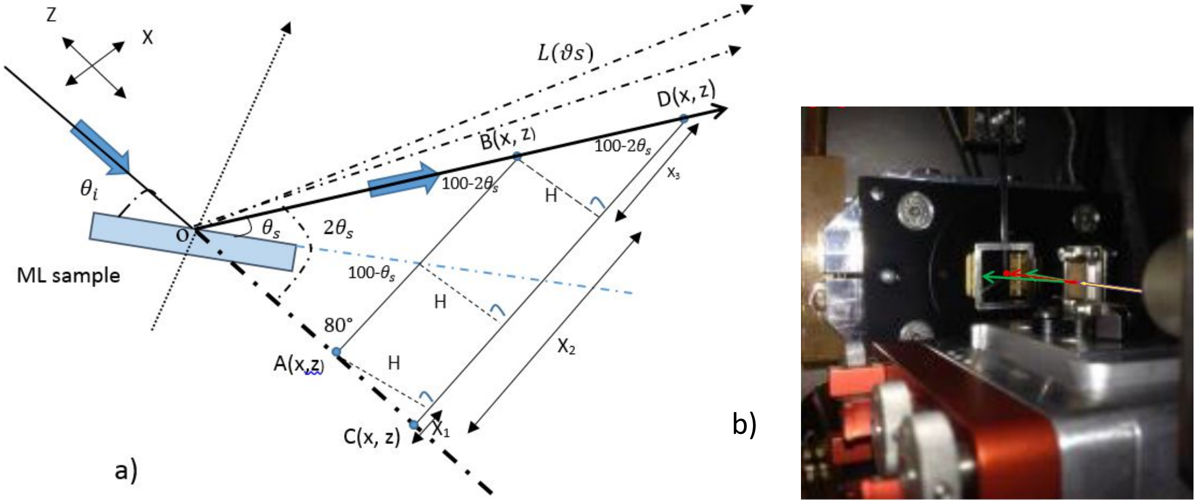

Figure 5.8: a) Geometrical sketch of GI-EUVS experiment. Points A, B, C and D are pixel coordinate points. The x-values of each coordinate points represent displacements in the X-direction and z-values in the Z-direction. b) A picture showing the incident and reflected directions inside the experimental chamber (photo by Aleksey Maryasov).

Points A, B, C and D are four coordinate points where the CCD is situated when performing measurements. A and C are coordinate points for the highest peak intensity of the direct spot, while B and D are pixel positions for the specular peak of the diffuse reflection. Firstly, image of direct spot at positions A and C and images of diffuse reflection at B and D are measured to calibrate the incidence angle according to Eq. 5-1. This method of incidence angle calibration reveals an error of $\Delta\theta_i \approx \pm 1.1°$ from the manually set values.

$$\theta_\mathrm{i} = 50 - \frac{1}{2}\tan^{-1}\left[\frac{5.671\times \mathrm{H}}{5.671\times(x_1+\mathrm{x}_3)-\mathrm{H}}\right] \tag{5-1}$$

Where x_1 and x_3 are determined from pixel coordinates of the specular peaks in direct and reflected spots, x_2 is the CCD movement in the X-direction, H is CCD displacement in the Z-direction (Fig 5-9a) and the experimenter sets the values manually.

The high-energy CCD camera (ANDOR-BN-DX434) used in the current set-up has pixel size (W × H: 13 x 13 μm) and the angular separation between consecutive pixels is about 0.2 mrad. These CCD parameters together with sample – CCD distance $\mathrm{L}(\theta_\mathrm{s})$ enable to calculate the solid angle of each pixel (Ω_s) according to Eq.5-2.

$$\Omega_\mathrm{s}(\theta_s) = \frac{169\times 10^{-6}\,\mathrm{mm}^2}{0.985\ \mathrm{L}(\theta_\mathrm{s})^2} \tag{5-2}$$

$$\mathrm{L}(\theta_\mathrm{s}) = \mathrm{L_o}(\,\mathrm{mm}) \pm \mathrm{n}(0.0008) \tag{5-3}$$

$$\mathrm{L_o} = [\mathrm{OC}^2 + \mathrm{CD}^2 - 2(\mathrm{OC})(\mathrm{CD})\sin(10°)]^{1/2} \tag{5-4}$$

Where L_o refers to $\overrightarrow{OD}$ in Fig 5.9a (i.e. distance of the CCD pixel containing the specular peak from the sample at point "O"), n=$0, \pm 1, \pm 2, \pm 3, \dots 1024$, with n=0 indicating the specular beam. Therefore, the ARS distribution of the diffuse reflection (scattering) can be calculated according to the previously given formula:

$$ARS(\theta_s) = \frac{P_s(\theta_s)}{P_i\,\Omega_\mathrm{s}(\theta_s)} \tag{5-5}$$

Where $\mathrm{P_s}$ and $\mathrm{P_i}$ refer to the scattered and incident powers respectively. Thus, ARS of each measurement per sterdian (Sr) can be independently calculated by using Eq.5-2 for solid angle $\Delta\Omega_s$. However, absolute calibration of ARS is challenging in the current set-up since calibration of $\mathrm{P_s}$ and $\mathrm{P_i}$ demand incorporation of additional optics.

Here after, angular distribution of direct spot and diffuse reflection from two of the ML samples are analyzed based on the procedures mentioned up to now. Fig 5.9 shows the angular distributions of direct spot and diffuse reflection from sample_B in a very brief integration time (0.25 s) in both cases. This result is obtained from the spots given in Fig 5.5a (direct) and Fig 5.5b (reflection).

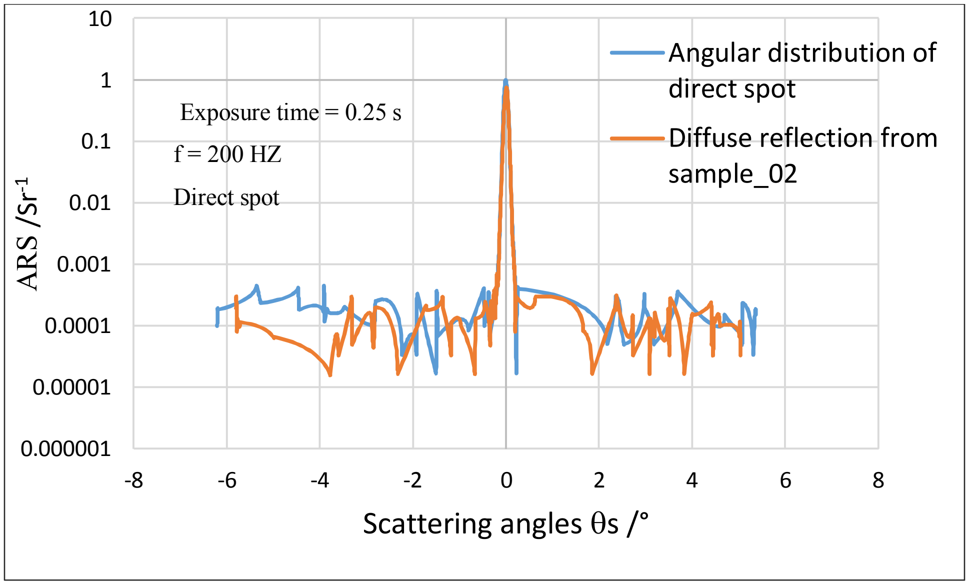

Figure 5.9: Angular distributions of the direct spot and diffused reflection from the ML sample_B.

The specular peak of the diffuse reflection (orange color) is lower than the peak of the direct spot, which is due to scattering into non-specular directions. However, the non-specular directions might be at larger angles that the CCD image area is unable to reach out. Alternatively, since the divergence of the beam is high (~4 mrad) in the current set-up, fine features of the samples, which contribute to the lower non-specular directions, are not resolved. A similar angular distribution analysis shown in Fig 5.10 is performed for the direct and reflected spots given in Fig 5.6a and b.

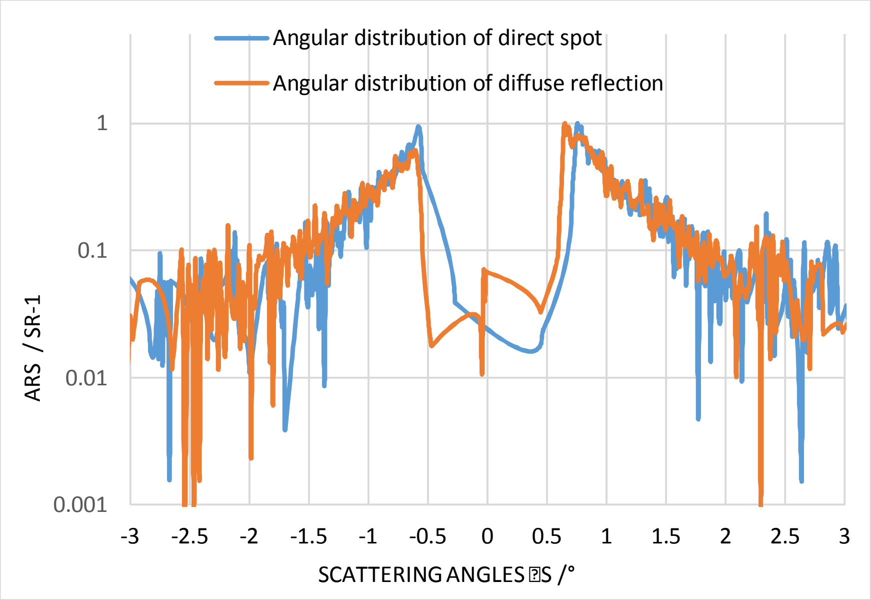

Figure 5.10: Angular distributions of the direct spot and diffused reflection from ML sample_A. The central halo is due to the beammstop introduced to block the specular beam.

6. CONCLUSION AND RECOMMENDATION

6.1 Summary and conclusion

In summary, this thesis presents innovative metrology techniques for EUV and soft X-ray MLs. A considerable effort is also exerted on coatings of short period MLs for high reflection performances for wavelengths of below 10 nm. GI-EUVR near the absorption edges of the low-Z elements in ML structures enable characterization of optical and structural properties with high sensitivity and reliability. In combination with X-ray reflectivity measurements that determine period of MLs with high depth-spatial resolution, the GI-EUVR give detailed quantitative analysis of buried interfaces of multilayer structures in a non-destructive and non-imaging setup. This method is also sensitive enough to perform damage analysis of ML mirrors exposed to energetic ions and photons.

Test measurements and analysis were performed on Si/Mo MLs. Si/Mo MLs were chosen because sufficient data exist in the literature that makes the comparison of our analysis more reliable. The MLs were deposited in RF magnetron sputtering facility and were designed for the development of an instrument for solar coronal imaging. The GI-EUVR measurements near the Si L_{III} edge (at 99 eV) yield optical constants and thicknesses of layers and interlayers of the MLs. Asymmetric nature of the inter-diffusion layers (interlayers) at Mo-on-Si and Si-on-Mo interfaces is confirmed. The stoichiometric composition of the interlayers, retrieved from the calculated optical constants, give different types of moly – silicide alloys. $MoSi_2$ seems thermodynamically favorable alloy for both types of interfaces. However, Mo_3Si_5 and Mo_2Si_3 are also found to be formed because of the diffusion during layers growth.

Multilayer damage analysis due to irradiation of low energy ions of alpha particles (4 keV He^{++}) was performed by using the GI-EUVR method. The slight thickness fluctuations due to the ion bombardments, decay of reflectivity performance and shift of optical constants ($\Delta\delta$ and $\Delta\beta$) are derived with high sensitivity.

After a series of tests on Si/MO MLs, the method was implemented to characterize the newly deposited B4C/CeO2 MLs near the boron K edge. Optical constants and thicknesses of CeO2 layers, B4C layers and inter-diffusion layers are derived. This was an opportunity to test the GI-

EUVR at different wavelength than the Si edge. The robustness of the method is again confirmed by the level of consistency B4C optical constants (δ and β) in the range of photon energies (177.53 - 183.82 eV) near the boron edge have shown with previously reported measurements by R. Soufli et.al [125] and G. Monaco et.al.[126].

The B4C/CeO2 MLs were manufactured to represent reflective-optics candidates for future lithography at 6.x nm. Deposition was performed using direct current (DC) magnetron sputtering facility. In addition to the GI-EUVR near the boron edge measurements, imaging techniques such as STEM and HAADF-STEM were used to fully characterize them. The near normal incidence reflectivity of the mirror at 6.9 nm wavelength is ~4.4 lower than what was theoretically expected. The low performance is attributed to the enhanced interface - diffusions confirmed through several state of the art imaging and non-imaging techniques. The detail optical and structural analysis of the MLs give paramount feedback for the optimizations of future depositions runs.

Lastly, grazing incidence tabletop scattering experiment at incidence wavelength of 13.5 nm and 2% bandwidth from a gas discharge produced plasma is being developed at the physics department of RWTH Aachen University. Since this experiment is still ongoing, only preliminary results are discussed in the thesis. It is possible to resolve mid-spatial frequency roughness (MSFR) roughness the current set-up. The MSFR is a major cause for flare in imaging.

In overall, the thesis discusses on a robust EUV and soft X-ray metrology technique of multilayers with major emphasis in characterization of buried interfaces, which are yet particularly challenging. On the other hand, the necessity of high reflection throughput at increasingly shorter wavelengths of EUV and X-rays is apparent in the semiconductor industry, astrophysical instrumentations, and large light source facilities such as the synchrotrons and FELs. Thus, the metrology technique presented in the thesis can be applied in the above-mentioned companies and facilities to a lesser extent. In reality, the application is far reaching.

The development B4C/CeO2 MLs aimed for high reflection at wavelengths below 10 nm can be interest for the emerging demand of laboratory-based reflectometry for fundamental study in ultra- thin films, enhancement of resolution imaging, spectroscopic application to explore extreme states of matter, etc. With further interface engineering, the B4C/CeO2 MLs can be promising candidates for N7 EUV lithography.

6.2 Recommended future works

As a continuation of the work in this thesis, the following are some future outlook and suggestions.

1. Performance, structural and optical stability of the optical devices (ML coatings in particular) in many areas of application are issues that need research. In EUV and X-rays, minor damage due to the irradiation of energetic photons and/or particles could cause significant loss in performance and stability. For its high sensitivity to optical properties and thicknesses, further experiments of damage analysis of MLs using the GI-EUVR method are highly recommended. Impact of low energy alpha particles on the capped Si/Mo MLs performed in this thesis can assist as a starting point.
2. Further optimization in the deposition processes of B4C/CeO2 MLs to reduce interface-diffusion at the interfaces, which caused degradation of reflectivity performance, is an immediate task to be performed. Controlling the amount of Oxygen (O_2) flow in a reactive RF magnetron sputtering could solve the diffusion problem significantly. Impacts of vacuum pressure, substrate temperature, and gas flow rates need further optimizations.
3. With regard to the EUV scatterometer, analytical model for the inverse scattering problems of multilayers is required. Either solving the Rigorous coupled-wave analysis (RCWA) of the incident electromagnetic radiation or characterizing the optical properties (polarization, power, incidence and scattered angles) of the incident radiation in order to calculate the ARS from the PSD parameters according Eq. (1-15) need to be formulated. In addition, the stray-light analysis, the scattering signatures of the beamline and of the pinholes are possible future tasks.

Bibliography

1. DuMond, J.W.M., and Youtz, J.P. ‘Selective X-Ray Diffraction from Artificially Stratified Metal Films Deposited by Evaporation’, Physical Review, 1935, 48, (8), pp. 703-703

2. Spiller, E. ‘Low-Loss Reflection Coatings Using Absorbing Materials’, Applied Physics Letters, 1972, 20, (9), pp. 365-367

3. Daniele SPIGA ‘development of multilayer-coated mirrors for future x-ray telescopes’, PhD thesis, Universit`a degli studi di Milano-Bicocca, 2004-2005

4. Fineschi, S., Antonucci, E., Naletto, G., Romoli, M., Spadaro, D., Nicolini, G., Abbo, L., Andretta, V., Bemporad, A., and Berlicki, A. ‘METIS: a novel coronagraph design for the Solar Orbiter Mission’, (International Society for Optics and Photonics, 2012, edn.), pp. 84433H-84433H-84413

5. Rousseau, A.D., Windt, D.L., Winter, B., Harra, L., Lamoureux, H., and Eriksson, F. ‘Stability of EUV multilayers to long-term heating, and to energetic protons and neutrons, for extreme solar missions’, in Citterio, O., and Odell, S.L. (Eds.): ‘Optics for Euv, X-Ray, and Gamma-Ray Astronomy Ii’ (2005)

6. Windt, D., and Waskiewicz ‘Multilayer facilities required for extreme-ultraviolet lithography’, Journal of Vacuum Science & Technology B, 1994, 12, (6), pp. 3826-3832

7. Bajt, S., Alameda, J.B., Barbee Jr, T.W., Clift, W.M., Folta, J.A., Kaufmann, B.B., and Spiller, E.A. ‘Improved reflectance and stability of Mo/Si multilayers’, in Editor (Ed.)^(Eds.): ‘Book Improved reflectance and stability of Mo/Si multilayers’ (International Society for Optics and Photonics, 2001, edn.), pp. 65-75

8. Montcalm, C., Bajt, S., Mirkarimi, P.B., Spiller, E.A., Weber, F.J., and Folta, J.A. ‘Multilayer reflective coatings for extreme-ultraviolet lithography’, (International Society for Optics and Photonics, 1998, edn.), pp. 42-51

9. Singh, M., and Braat, J.J. ‘Design of multilayer extreme-ultraviolet mirrors for enhanced reflectivity’, Applied optics, 2000, 39, (13), pp. 2189-2197

10. Endo A. ‘Extendibility Evaluation of Industrial EUV Source Technologies for kW Average Power and 6. x nm Wavelength Operation’, Journal of Modern Physics, 2014, 2014

11. David, A.'Soft x-rays and extreme ultraviolet radiation: Principles and Applications' (Cambridge University Press 1999. 1999)

12. Henke, B.L., Gullikson, E.M., and Davis, J.C. 'X-ray interactions: photoabsorption, scattering, transmission, and reflection at E= 50-30,000 eV, Z= 1-92', Atomic data and nuclear data tables, 1993, 54, (2), pp. 181-342

13. Windt, D.L., Cash, W.C., Scott, M., Arendt, P., Newman, B., Fisher, R.F., and Swartzlander, A.B. 'Optical-constants for thin-films of ti, zr, nb, mo, ru, rh, pd, ag, hf, ta, w, re, ir, os, pt, and au from 24-a to 1216-a', applied optics, 1988, 27, (2), pp. 246-278

14. Soufli, R., and Gullikson, E.M. 'Reflectance measurements on clean surfaces for the determination of optical constants of silicon in the extreme ultraviolet-soft-x-ray region', Applied Optics, 1997, 36, (22), pp. 5499-5507

15. Fernandez-Perea, M., Larruquert, J.I., Aznarez, J.A., Mendez, J.A., Vidal-Dasilva, M., Gullikson, E., Aquila, A., Soufli, R., and Fierro, J.L.G.: 'Optical constants of electron-beam evaporated boron films in the 6.8-900 eV photon energy range', Journal of the Optical Society of America a-Optics Image Science and Vision, 2007, 24, (12), pp. 3800-3807

16. Spiller, E. 'Soft X-ray optics' (SPIE Optical Engineering Press Bellingham, WA, 1994. 1994)

17. Nayak, M., and Lodha, G.S. 'Optical Response Near the Soft X-Ray Absorption Edges and Structural Studies of Low Optical Contrast System Using Soft X-Ray Resonant Reflectivity', Journal of Atomic, Molecular, and Optical Physics, 2011, 2011

18. Sertsu, M., Nardello, M., Giglia, A., Corso, A., Maurizio, C., Juschkin, L., and Nicolosi, P. 'Analysis of buried interfaces in multilayer mirrors using grazing incidence extreme ultraviolet reflectometry near resonance edges', Applied Optics, 2015, 54, (35), pp. 10351-10358

19. Moore, G.E. 'Cramming more components onto integrated circuits (Reprinted from Electronics, pg 114-117, April 19, 1965)', Proceedings of the Ieee, 1998, 86, (1), pp. 82-85

20. Wagner, C., and Harned, N. 'EUV LITHOGRAPHY Lithography gets extreme', Nature Photonics, 2010, 4, (1), pp. 24-26

21. Ronse, K. 'Optical lithography - a historical perspective', Comptes Rendus Physique, 2006, 7, (8), pp. 844-857

22. Hecht, B.J. 'PHOTONIC FRONTIERS: EUV LITHOGRAPHY: EUV lithography has yet to find its way into the fab', http://www.laserfocusworld.com/index.html, 2013

23. Makhotkin, I.A., Zoethout, E., van de Kruijs, R., Yakunin, S.N., Louis, E., Yakunin, A.M., Banine, V., Muellender, S., and Bijkerk, F. ‘Short period La/B and LaN/B multilayer mirrors for similar to 6.8 nm wavelength’, Optics Express, 2013, 21, (24), pp. 29894-29904

24. Yakunin, S.N., Makhotkin, I.A., Nikolaev, K.V., van de Kruijs, R.W.E., Chuev, M.A., and Bijkerk, F.: ‘Combined EUV reflectance and X-ray reflectivity data analysis of periodic multilayer structures’, Optics Express, 2014, 22, (17), pp. 20076-20086

25. Makhotkin, I.A., Zoethout, E., Louis, E., Yakunin, A.M., Muellender, S., and Bijkerk, F. ‘Spectral properties of La/B - based multilayer mirrors near the boron K absorption edge’, Optics Express, 2012, 20, (11), pp. 11778-11786

26. Kuznetsov, D., Yakshin, A., Sturm, J., van de Kruijs, R., Louis, E., and Bijkerk, F.: ‘High-reflectance La/B-based multilayer mirror for 6. x nm wavelength’, Optics letters, 2015, 40, (16), pp. 3778-3781

27. Awaki, H., Tawara, Y., Ogasaka, Y., Kunieda, H., Ohmori, H., Honda, H., and Shioya, S.: ‘Development of a thin substrate for X-ray telescope’, in Freund, A.K., Ishikawa, T., and Khounsary, A.M. (Eds.): ‘X-Ray Mirrors, Crystals and Multilayers’ (2001), pp. 68-75

28. Mao, P.H., Bellan, L., Harrison, F.A., Windt, D.L., and Christensen, F.E. ‘Evaluation and optimization of multilayer designs for astronomical x-ray telescopes using a field-of-view- and energy-dependent figure of merit’, in Hoover, R.B., and Walker, A.B.C. (Eds.): ‘X-Ray Optics, Instruments, and Missions Iv’ (2000), pp. 126-133

29. ‘ASTRONOMY In-space UV calibration of the METIS solar coronagraph’, Laser Focus World, 2015, 51, (1), pp. 20

30. Andretta, V., Bemporad, A., Focardi, M., Grimani, C., Landini, F., Pancrazzi, M., Sasso, C., Spadaro, D., Straus, T., Uslenghi, M.C., Antonucci, E., Fineschi, S., Naletto, G., Nicolini, G., Nicolosi, P., and Romoli, M. ‘On-board detection and removal of cosmic ray and solar energetic particle signatures for the Solar Orbiter-METIS coronagraph’, in Chiozzi, G., and Radziwill, N.M. (Eds.): ‘Software and Cyberinfrastructure for Astronomy Iii’ (2014)

31. Focardi, M., Capobianco, G., Andretta, V., Sasso, C., Romoli, M., Landini, F., Fineschi, S., Pancrazzi, M., Bemporad, A., Nicolini, G., Pucci, S., Uslenghi, M., Naletto, G., Nicolosi, P., Spadaro, D., Teriaca, L., Schuehle, U.H., and Antonucci, E. ‘In-flight UV and polarized-VL radiometric calibrations of the Solar Orbiter/METIS imaging coronagraph’, in Takahashi, T.,

DenHerder, J.W.A., and Bautz, M. (Eds.): ‘Space Telescopes and Instrumentation 2014: Ultraviolet to Gamma Ray’ (2014)

32. Windt, D.L. ‘EUV multilayer coatings for solar imaging and spectroscopy’, in Editor (Ed.) ‘Book EUV multilayer coatings for solar imaging and spectroscopy’ (International Society for Optics and Photonics, 2015, edn.), pp. 96040P-96040P-96012

33. Feldman, U., Schuhle, U., Widing, K.G., and Laming, J.M. ‘Coronal composition above the solar equator and the north pole as determined from spectra acquired by the SUMER instrument on Soho’, Astrophysical Journal, 1998, 505, (2), pp. 999-1006

34. Windt, D.L. ‘IMD—Software for modeling the optical properties of multilayer films’, Computers in physics, 1998, 12, (4), pp. 360-370

35. Gullikson, E.M., Stearns, D.G., Gaines, D.P., and Underwood, J.H. ‘Nonspecular scattering from multilayer mirrors at normal incidence’, in Editor (Ed.) ‘Book Nonspecular scattering from multilayer mirrors at normal incidence’ (International Society for Optics and Photonics, 1997, edn.), pp. 412-419

36. Giday, S.M., Zuppella, P., Pelizzo, M., and Nicolosi, P. ‘Exploring EUV near absorption edge optical constants for enhanced and sensitive grazing incidence reflectivity’,(International Society for Optics and Photonics, 2013, edn.), pp. 886111-886111-886115

37. Bass, M., Van Stryland, E., Williams, D., and Wolfe, W.: ‘Handbook of optics’ (McGraw-Hill, 1996. 1996)

38. Scholze, F., Kato, A., and Laubis, C. ‘Characterization of nano-structured surfaces by EUV scatterometry’, in Editor (Ed.), ‘Book Characterization of nano-structured surfaces by EUV scatterometry’ (IOP Publishing, 2011, edn.), pp. 012006

39. Rice, S.O. ‘Reflection of electromagnetic waves from slightly rough surfaces’, Communications on pure and applied mathematics, 1951, 4, (2-3), pp. 351-378

40. Harvey, J.E., Krywonos, A., and Vernold, C.L. ‘Modified Beckmann-Kirchhoff scattering model for rough surfaces with large incident and scattering angles’, optical engineering, 2007, 46, (7), pp. 078002-078002-078010

41. Harvey, J.E., Choi, N., Krywonos, A., and Marcen, J.G. ‘Calculating BRDFs from surface PSDs for moderately rough optical surfaces’, (International Society for Optics and Photonics, 2009, edn.), pp. 74260I-74260I-74269

42. Schiff, T.F. ‘Comparison of the Kirchhoff and Rayleigh-Rice diffractions for sinusoidal surfaces’, Montana State University-Bozeman, 1990
43. Stover, J.C., and Harvey, J.E. ‘Limitations of Rayleigh Rice Perturbation Theory for describing surface scatter’, (International Society for Optics and Photonics, 2007, edn.), pp. 66720B-66720B-66729
44. James, E.H., Krywonos, A., and Vernold, C.L. ‘Modified Beckmann-Kirchhoff scattering theory for rough surfaces with large scattering and incident angles’, Optical Engineering, Papers, 2006, 46, (7), pp. 078002-078001
45. Vernold, C.L., and Harvey, J.E.:‘Modified Beckmann-Kirchoff scattering theory for nonparaxial angles’, (International Society for Optics and Photonics, 1998, edn.), pp. 51-56
46. Ragheb, H., and Hancock, E.R. ‘The modified Beckmann–Kirchhoff scattering theory for rough surface analysis’, Pattern Recognition, 2007, 40, (7), pp. 2004-2020
47. Harvey, J.E. ‘Surface scatter phenomena: a linear, shift-invariant process’, (International Society for Optics and Photonics, 1990, edn.), pp. 87-99
48. Krywonos, A. ‘Predicting surface scatter using a linear systems formulation of non-paraxial scalar diffraction’, University of Central Florida Orlando, Florida, 2006
49. Harvey, J.E., Choi, N., and Krywonos, A. ‘Scattering from moderately rough interfaces between two arbitrary media’, (International Society for Optics and Photonics, 2010, edn.), pp. 77940V-77940V-77911
50. Wynn, C. ‘An introduction to BRDF-based lighting’, Nvidia Corporation, 2000
51. Schröder, S., Herffurth, T., Blaschke, H., and Duparré, A. ‘Angle-resolved scattering: an effective method for characterizing thin-film coatings’, Applied optics, 2011, 50, (9), pp. C164-C171
52. Bass, M., Stryland, E.W.V., Williams, D.R., and Wolfe, W.L. ‘Handbook of Optics Volume II Devices, Measurements’, Handbook of Optics Volume II Devices, Measurements, and Properties 2nd edition by Michael Bass, Eric W. Van Stryland, David R. Williams, William L. Wolfe New York, NY: McGraw-Hill, INC, 1995, 1995, 1
53. Church, E., Jenkinson, H., and Zavada, J. ‘Relationship between surface scattering and microtopographic features’, Optical Engineering, 1979, 18, (2), pp. 182125-182125-
54. Stover, J.C. ‘Optical scattering: measurement and analysis’ (SPIE optical engineering press Bellingham, WA, 1995. 1995)

55. Church, E.L.: ‘Fractal surface finish’, in Editor (Ed.)^(Eds.): ‘Book Fractal surface finish’ (International Society for Optics and Photonics, 1988, edn.), pp. 75-85
56. Trost, M., Schröder, S., Lin, C., Duparré, A., and Tünnermann, A.: ‘Roughness characterization of EUV multilayer coatings and ultra-smooth surfaces by light scattering’, in Editor (Ed.)^(Eds.): ‘Book Roughness characterization of EUV multilayer coatings and ultra-smooth surfaces by light scattering’ (International Society for Optics and Photonics, 2012, edn.), pp. 85010F-85010F-85017
57. Herffurth, T. ‘Light scattering and roughness analysis of optical surfaces and thin films’, Jena, Friedrich-Schiller-Universität Jena, Diss., 2015, 2015
58. Suman, M.: ‘Studio dell'interazione della radiazione elettromagnetica con strutture nanometriche per lo sviluppo di ottiche’, 2009
59. Ohring, M. ‘Materials science of thin films’ (Academic press, 2001. 2001)
60. Wang, Y., Chen, W., Wang, B., and Zheng, Y. ‘Ultrathin Ferroelectric Films: Growth, Characterization, Physics and Applications’, Materials, 2014, 7, (9), pp. 6377-6485
61. Pimpinelli, A., and Villain, J.‘Physics of crystal growth’ (Cambridge university press Cambridge, 1998. 1998)
62. Ayers, J.E. ‘Heteroepitaxy of semiconductors: theory, growth, and characterization’ (CRC press, 2007. 2007)
63. Louis, E. ‘Physics and technology development of multilayer EUV reflective optics’ (Universiteit Twente, 2012. 2012)
64. Venables, J. ‘Introduction to surface and thin film processes’ (Cambridge University Press, 2000. 2000)
65. Baskaran, A., and Smereka, P. ‘Mechanisms of stranski-krastanov growth’, Journal of Applied Physics, 2012, 111, (4), pp. 044321
66. Kern, W. ‘Thin film processes II’ (Academic press, 2012. 2012)
67. Sigmund, P. ‘Theory of sputtering. I. Sputtering yield of amorphous and polycrystalline targets’, Physical review, 1969, 184, (2), pp. 383
68. Fu, C., Yang, C., Han, L., and Chen, H. ‘The thickness uniformity of films deposited by magnetron sputtering with rotation and revolution’, Surface and Coatings Technology, 2006, 200, (12), pp. 3687-3689

69. Soloviev, A., Sochugov, N., Oskomov, K., and Kovsharov, N. ‘Film thickness distribution in magnetron sputtering system with the round cathode’, Изв. вузов. Физика, 2006, (8), pp. 491-493

70. Nedelcu, I. ‘Interface structure and interdiffusion in Mo/Si multilayers’ (University of Twente, 2007. 2007)

71. Luken, E., Ziegler, E., and Lingham, M. ‘In-situ growth control of X-ray multilayers using visible light kinetic ellipsometry and grazing incidence X-ray reflectometry’, (International Society for Optics and Photonics, 1996, edn.), pp. 113-118

72. Morton, D.E., Johs, B., and Hale, J. ‘Optical monitoring of thin films using spectroscopic ellipsometry’, in Editor (Ed.)(Eds.): ‘Book Optical monitoring of thin films using spectroscopic ellipsometry’ (2002, edn.), pp. 299-305

73. Toyoshima, Y., Arai, K., Matsuda, A., and Tanaka, K. ‘Real time insitu observation of the film growth of hydrogenated amorphous silicon by infrared reflection absorption spectroscopy’, Applied physics letters, 1990, 56, (16), pp. 1540-1542

74. Nicolosi, P. ‘EUV Multilayer Optics: Design, Development and Metrology’, Short Wavelength Laboratory Sources, 2014, pp. 283

75. Fullerton, E.E., Schuller, I.K., Vanderstraeten, H., and Bruynseraede, Y. ‘Structural refinement of superlattices from x-ray diffraction’, Physical Review B, 1992, 45, (16), pp. 9292

76. Salamon, K., Milat, O., Radić, N., Dubček, P., Jerčinović, M., and Bernstorff, S. ‘Structure and morphology of magnetron sputtered W films studied by x-ray methods’, Journal of Physics D: Applied Physics, 2013, 46, (9), pp. 095304

77. Zuppella, P., Corso, A.J., Nicolosi, P., Windt, D.L., and Pelizzo, M.G. ‘Innovative multilayer coatings for space solar physics: performances and stability over time’, Euv and X-Ray Optics: Synergy between Laboratory and Space Ii, 2011, 8076

78. Henke, B.L., Gullikson, E.M., and Davis, J.C. ‘X-RAY INTERACTIONS - PHOTOABSORPTION, SCATTERING, TRANSMISSION, AND REFLECTION AT E=50-30,000 EV, Z=1-92’, Atomic Data and Nuclear Data Tables, 1993, 54, (2), pp. 181-342

79. Nardello, M., Zuppella, P., Polito, V., Corso, A.J., Zuccon, S., and Pelizzo, M.G. ‘Stability of EUV multilayer coatings to low energy alpha particles bombardment’, Optics Express, 2013, 21, (23), pp. 28334-28343

80. Puik, E.J., Vanderwiel, M.J., Zeijlemaker, H., and Verhoeven, J. 'ION-BOMBARDMENT OF THIN-LAYERS - the effect on the interface roughness and its x-ray reflectivity', Review of Scientific Instruments, 1992, 63, (1), pp. 1415-1419

81. Bajt, S., Chapman, H.N., Nguyen, N., Alameda, J., Robinson, J.C., Malinowski, M., Gullikson, E., Aquila, A., Tarrio, C., and Grantham, S.: 'Design and performance of capping layers for EUV multilayer mirrors', in Engelstad, R.L. (Ed.): 'Emerging Lithographic Technologies Vii, Pts 1 and 2' (2003), pp. 236-248

82. Bajt, S.A., Chapman, H.N., Nguyen, N., Alameda, J., Robinson, J.C., Malinowski, M., Gullikson, E., Aquila, A., Tarrio, C., and Grantham, S.: 'Design and performance of capping layers for extreme-ultraviolet multilayer mirrors', Applied Optics, 2003, 42, (28), pp. 5750-5758

83. Mirkarimii, P.B., Bajt, S., and Stearns, D.G.: 'Mitigation of substrate defects in reticles using multilayer buffer layers', in Editor (Ed.)^(Eds.): 'Book Mitigation of substrate defects in reticles using multilayer buffer layers' (Google Patents, 2001, edn.), pp.

84. Gullikson, E.M., Anderson, C.N., Kim, S.-S., Lee, D., Miyakawa, R., Salmassi, F., and Naulleau, P.P.: 'Molybdenum/silicon multilayer components for high harmonic generation sources', Applied Optics, 2015, 54, (13), pp. 4280-4284

85. Corso, A.J., Zuppella, P., Nicolosi, P., Windt, D.L., Gullikson, E., and Pelizzo, M.G.: 'Capped Mo/Si multilayers with improved performance at 30.4 nm for future solar missions', Optics Express, 2011, 19, (15), pp. 13963-13973

86. Fineschi, S., Antonucci, E., Romoli, M., Bemporad, A., Capobianco, G., Crescenzio, G., Nicolini, G., Massone, G., Telloni, D., Focardi, M., Landini, F., Pancrazzi, M., Poletto, L., Pelizzo, M.-G., Da Deppo, V., Moses, J.D., Andretta, V., Naletto, G., Nicolosi, P., Spadaro, D., Berlicki, A., Uslenghi, M., Malvezzi, M., Teriaca, L., Abbo, L., and Magli, E.: 'Novel Space Coronagraphs: METIS, a flexible optical design for multi-wavelength imaging and spectrography', in Fineschi, S., and Fennelly, J. (Eds.): 'Solar Physics and Space Weather Instrumentation V' (2013)

87. Nannarone, S., Borgatti, F., DeLuisa, A., Doyle, B.P., Gazzadi, G.C., Giglia, A., Finetti, P., Mahne, N., Pasquali, L., Pedio, M., Selvaggi, G., Naletto, G., Pelizzo, M.G., and Tondello, G.: 'The BEAR beamline at ELETTRA', AIP Conference Proceedings, 2004, (708), pp. 450-453

88. Oetzel, M., and Heger, G.: ‘Laboratory X-ray powder diffraction: a comparison of different geometries with special attention to the usage of the CuK alpha doublet’, Journal of Applied Crystallography, 1999, 32, pp. 799-807

89. Windt, D.L.: ‘IMD - Software for modeling the optical properties of multilayer films’, Computers in Physics, 1998, 12, (4), pp. 360-370

90. Lampton, M., Margon, B., and Bowyer, S. ‘parameter-estimation in x-ray astronomy’, Astrophysical Journal, 1976, 208, (1), pp. 177-190

91. Yaqoob, T. ‘Parameter estimation in X-ray astronomy revisited’, Astrophysical Journal, 1998, 500, (2), pp. 893-898

92. Binda, P.D., and Zocchi, F.E. ‘Genetic algorithm optimization of X-ray multilayer coatings’, in DelRio, M.S. (Ed.): ‘Advances in Computational Methods for X-Ray and Neutron Optics’ (2004), pp. 97-108

93. Ulyanenkov, A., Omote, K., and Harada, J. ‘The genetic algorithm: refinement of X-ray reflectivity data from multilayers and thin films’, Physica B, 2000, 283, (1-3), pp. 237-241

94. Giday, S.M., Zuppella, P., Pelizzo, M.G., and Nicolosi, P. ‘Book Exploring EUV near absorption edge optical constants for enhanced and sensitive grazing incidence reflectivity’ (p1-15, 2013, edn.), pp. 15

95. Serafinczuk, J., Pietrucha, J., Schroeder, G., and Gotszalk, T.P. ‘Thin film thickness determination using X-ray reflectivity and Savitzky-Golay algorithm’, Optica Applicata, 2011, 41, (2), pp. 315-322

96. Fedorenko, A.I., Pershin, Y.P., Poltseva, O.V., Ponomarenko, A.G., Voronov, D.L., and Yulin, S.A.: ‘Structure of interfaces in multilayers’, in Briant, C.L., Carter, C.B., and Hall, E.L. (Eds.): ‘Interfacial Engineering for Optimized Properties’ (1997), pp. 249-254

97. Soufli, R., and Gullikson, E.M. ‘Absolute photoabsorption measurements of molybdenum in the range 60-930 eV for optical constant determination’, Applied Optics, 1998, 37, (10), pp. 1713-1719

98. Lodha, M.N.a.G.S. ‘Optical Response Near the Soft X-Ray Absorption Edges and Structural Studies of Low Optical Contrast System Using Soft X-Ray Resonant Reflectivity’, Journal of Atomic,Molecular, and Optical Physics, 2011, 2011, pp. 23

99. Pelizzo, M.G., Suman, M., Monaco, G., Nicolosi, P., and Windt, D.L.: ‘High performance EUV multilayer structures insensitive to capping layer optical parameters’, Optics Express, 2008, 16, (19), pp. 15228-15237

100. Potocki, K.A., Calabrese, M.A., Carson, D., Ayon, J., Robinson, J., Oberright, J., VanSant, J.T., Natl Aeronautics Space, A., and Ieee, I. ‘NASA's sun-earth connection program strategic planning, missions & technology (2003-2028)’: ‘2003 Ieee Aerospace Conference Proceedings, Vols 1-8’ (2003), pp. 4009-4022

101. Muller, D., Marsden, R.G., St Cyr, O.C., and Gilbert, H.R.: ‘Solar Orbiter Exploring the Sun-Heliosphere Connection’, Solar Physics, 2013, 285, (1-2), pp. 25-70

102. Fineschi, S.‘Novel Optical Designs for Space Coronagraphs: Inverted Occulters and Lyot-stops’, in Editor (Ed.): ‘Book Novel Optical Designs for Space Coronagraphs: Inverted Occulters and Lyot-stops’ (2010, edn.), pp.

103. Delaboudiniere, J.P., Stern, R.A., Maucherat, A., Portier-Fozzani, F., Neupert, W.M., Gurman, J.B., Catura, R.C., Lemen, J.R., Shing, L., Artzner, G.E., Brunaud, J., Gabriel, A.H., Michels, D.J., Moses, J.D., Au, B., Dere, K.P., Howard, R.A., Kreplin, R., Defise, J.M., Jamar, C., Rochus, P., Chauvineau, J.P., Marioge, J.P., Clette, F., Cugnon, P., and Van Dessel, E.L. ‘Imaging the solar corona in the EUV’, in Antonucci, E., and Shea, M.A. (Eds.): ‘Sun and Its Atmosphere’ (1997), pp. 2231-2237

104. Habbal, S.R. ‘Imaging the source regions of the solar wind’, in Habbal, S.R. (Ed.) ‘Robotic Exploration Close to the Sun: Scientific Basis’ (1997), pp. 105-112

105. Corso, A.J., Zuppella, P., Nicolosi, P., and Pelizzo, M.G. ‘Long term stability of optical coatings in close solar environment’, Solar Physics and Space Weather Instrumentation Iv, 2011, 8148

106. Rossi, L., Jacques, L., Halain, J.-P., Renotte, E., Thibert, T., and Grodent, D.: ‘Space radiation parameters for EUI and the Sun Sensor of Solar Orbiter, ESIO and JUDE instruments’, Modeling, Systems Engineering, and Project Management for Astronomy Vi, 2014, 9150

107. Ziegler, J.F., Ziegler, M.D., and Biersack, J.P. ‘SRIM - The stopping and range of ions in matter (2010)’, Nuclear Instruments & Methods in Physics Research Section B-Beam Interactions with Materials and Atoms, 2010, 268, (11-12), pp. 1818-1823

108. Kavetskyy, T.S., Borc, J., Kukhazh, Y.Y., and Stepanov, A.L.: ‘The Influence of Low Dose Ion-Irradiation on the Mechanical Properties of PMMA Probed by Nanoindentation’ (2015. 2015)

109. Butterworth, J.E., and Barton, C.J. ‘TRIMCAT, a TRIM interface for GARFIELD’, Journal of Instrumentation, 2009, 4

110. Windt, D.L.: ‘IMD, Version 5, Installation and User's Manual’, in Editor (Ed.)^(Eds.): ‘Book IMD, Version 5, Installation and User's Manual’ (2013, edn.), pp.

111. Kulik, M., and Zuk, J. ‘Correlation between optical-properties and nuclear-damage profiles in ion-implanted oxidized gap crystals’, Nuclear Instruments & Methods in Physics Research Section B-Beam Interactions with Materials and Atoms, 1986, 15, (1-6), pp. 744-747

112. Giday, S.M., Zuppella, P., Pelizzo, M.G., and Nicolosi, P. ‘Book Exploring EUV near absorption edge optical constants for enhanced and sensitive grazing incidence reflectivity’ (p1-15, 2013, edn.), pp. 15

113. Roy, S., and Dev, B.N. ‘X-ray standing waves in a multi-trilayer system with linearly varying period’, Applied Surface Science, 2011, 257, (17), pp. 7566-7572

114. Vitta, S., Weisheit, M., Scharf, T., and Krebs, H.U. ‘Alloy-ceramic oxide multilayer mirrors for water-window soft x rays’, Optics Letters, 2001, 26, (18), pp. 1448-1450

115. Uspenskii, Y., Burenkov, D., Hatano, T., and Yamamoto, M. ‘Optimal design of multilayer mirrors for water-window microscope optics’, Optical Review, 2007, 14, (1), pp. 64-73

116. Martinez-Galarce, D., Soufli, R., Windt, D.L., Bruner, M., Gullikson, E., Khatri, S., Spiller, E., Robinson, J.C., Baker, S., and Prast, E.: ‘Multisegmented, multilayer-coated mirrors for the Solar Ultraviolet Imager’, Optical Engineering, 2013, 52, (9)

117. Matyi, R.J. ‘High resolution x-ray reflectometery: theory, practice, accuracy and precision’, ‘Analytical and Diagnostic Techniques for Semiconductor Materials and Devices’ (2003)

118. Hirase, J. ‘Verification of Moore's Law Using Actual Semiconductor Production Data’, Ieice Transactions on Electronics, 2014, E97C, (6), pp. 599-608

119. Kozawa, T., Santillan, J.J., and Itani, T. ‘Feasibility study of sub-10-nm half-pitch fabrication by chemically amplified resist processes of extreme ultraviolet lithography: I. Latent image quality predicted by probability density model’, Japanese Journal of Applied Physics, 2014, 53, (10)

120. Wurm, S. ‘Transition to EUV lithography’ (2012. 2012)

121. Naujok, P., Yulin, S., Bianco, A., Mahne, N., Kaiser, N., and Tuennermann, A. 'La/B4C multilayer mirrors with an additional wavelength suppression', Optics Express, 2015, 23, (4), pp. 4289-4295

122. Oyama, T.G., Takahashi, T., Oshima, A., Washio, M., and Tagawa, S. 'Extendibility of EUV resists in the exposure wavelength from 13.5 down to 3.1 nm for next-generation lithography', Advances in Resist Materials and Processing Technology Xxviii, 2011, 7972

123. Sertsu, M.G., Nardello, M., Giglia, A., Corso, A.J., Maurizio, C., Juschkin, L., and Nicolosi, P.: 'Analysis of buried interfaces in multilayer mirrors using grazing incidence extreme ultraviolet reflectometry near resonance edges', Appl. Opt., 2015, 54, (35), pp. 10351-10358

124. Nannarone, S., Borgatti, F., DeLuisa, A., Doyle, B.P., Gazzadi, G.C., Giglia, A., Finetti, P., Mahne, N., Pasquali, L., Pedio, M., Selvaggi, G., Naletto, G., Pelizzo, M.G., and Tondello, G. 'The BEAR beamline at ELETTRA', in Warwick, T., Arthur, J., Padmore, H.A., and Stohr, J. (Eds.): 'Synchrotron Radiation Instrumentation' (2004), pp. 450-453

125. Soufli, R., Aquila, A.L., Salmassi, F., Fernandez-Perea, M., and Gullikson, E.M. 'Optical constants of magnetron-sputtered boron carbide thin films from photoabsorption data in the range 30 to 770 eV', Applied Optics, 2008, 47, (25), pp. 4633-4639

126. Monaco, G., Garoli, D., Frison, R., Mattarello, V., Nicolosi, P., Pelizzo, M.G., Rigato, V., Armelao, L., Giglia, A., and Nannarone, S. 'Optical constants in the EUV soft x-ray (5÷152 nm) spectral range of B4C thin films deposited by different deposition techniques', (2006, edn.), pp. 631712-631712-631712

127. Zhang, C., Katsuki, S., Horta, H., Imamura, H., Kondo, Y., Namihira, T., and Akiyama, H.: 'Xenon discharge produced plasma radiation source for EUV lithography', (IEEE, 2005, edn.), pp. 2320-2323

128. Trost, M., Schröder, S., Feigl, T., Duparré, A., and Tünnermann, A. 'Influence of the substrate finish and thin film roughness on the optical performance of Mo/Si multilayers', Applied optics, 2011, 50, (9), pp. C148-C153

129. ME, S.:'Guide for Angle Resolved Optical Scatter Measurements on Specular or Diffuse Surfaces', Semiconductor Equipment and Materials International, San José, CA, 2005